This is to certify that the
dissertation entitled

MODEL BASED ARTERIAL PRESSURE WAVEFORM ANALYSIS FOR MONITORING CARDIOVASCULAR FUNCTION

presented by

GOKUL SWAMY

has been accepted towards fulfillment
of the requirements for the

Ph.D. degree in Electrical Engineering

Major Professor's Signature

03/13/2009

Date

MODEL BASED ARTERIAL PRESSURE WAVEFORM ANALYSIS FOR MONITORING CARDIOVASCULAR FUNCTION

By

Gokul Swamy

A DISSERTATION

Submitted to
Michigan State University
in partial fulfillment of the requirements
for the degree of

DOCTOR OF PHILOSOPHY

Electrical Engineering

2009

ABSTRACT

MODEL-BASED ARTERIAL PRESSURE WAVEFORM ANALYSIS FOR MONITORING CARDIOVASCULAR FUNCTION

By

Gokul Swamy

Today, the workhorse in hemodynamic monitoring is the continuous (i.e., automated) measurement and display of blood pressure (BP) waveforms from peripheral arteries. In particular, minimally invasive (or non-invasive) catheters are broadly utilized in clinical practice to measure BP waveforms at these circulatory sites. However, it is well known that the cardiac output (CO) left ventricular ejection fraction (EF), left atrial pressure (LAP) and central aortic BP (ABP) are more useful in guiding therapy and more predictive of patient outcome. The conventional methods for measuring each of these critical central hemodynamic variables require an operator or an unacceptably high level of invasiveness. We attempt to bridge this gap by presenting three novel techniques to estimate the central ABP, CO and EF from mathematical analysis of routinely measured blood pressure waveforms.

The first technique is based on multi-channel blind system identification in which two or more measured outputs (peripheral artery pressure waveforms) of a single input, multi-output system (arterial tree) are mathematically analyzed so as to reconstruct the common unobserved input (central ABP waveform) to within an arbitrary scale factor. The technique then invokes Poiseuille's law to calibrate the reconstructed waveform to absolute pressure. Proportional estimates of beat-to-beat CO can be estimated from the reconstructed central ABP waveform by fitting it to a Windkessel model. The second

technique aims to estimate EF and proportional left ventricular elastance from a BP waveform by fitting the waveform to a lumped parameter model of the arterial tree and subsequently estimating the parameters of this model using an optimization scheme. Finally, a procedure to quantify wave reflection in the arterial tree and its subsequent application towards estimating the central ABP waveform from only a single peripheral artery pressure waveform is discussed. These techniques are validated on data collected from animal studies in which the hemodynamic parameters were varied over a wide physiologic range.

ACKNOWLEDGMENTS

First and foremost I would like to express my sincere gratitude and deepest appreciation to my committee chair, Dr. Ramakrishna Mukkamala, whose technical genius and passion for research have been instrumental in motivating me to attain greater heights in my research career. This dissertation would not have been possible without his constant professional and moral support.

I would also like to extend my sincere thanks to Dr. Satish Udpa whose invaluable guidance and motivation during my formative years led me to choose a career in research.

My heart felt gratitude is also due to Dr. Bari Olivier without whose support none of the physiologic studies could have been completed. I will forever be indebted to him for patiently explaining to me and teaching me the various surgical procedures used in physiologic experimentation.

Finally, I would like to express my heartfelt gratitude to my father Mr. V Doraiswamy Iyer and my mother Mrs. Sundari Swamy for their constant love and encouragement during every stage of my career. Words cannot express how thankful I am to my dearest wife Lakshmi for putting up with my late work hours and showering me with her constant love and encouragement. It is to my family that I dedicate this dissertation.

TABLE OF CONTENTS

LIST OF TABLES

LIST OF FIGURES

NOMENCLATURE

τ	Windkessel time constant
Ca	Arterial compliance
CO	Cardiac output
EI	Ejection interval
Elv(t)	Time varying ventricular elastance
Emin	Minimum left ventricular elastance
HR	Heart Rate
LVEF	Left ventricular ejection fraction
MAP	Mean arterial pressure
MBSI	Multi-channel blind system identification
n	Discrete time or sample index
nbs	Sample index denoting beginning of systolic ejection interval
nes	Sample index denoting end of systolic ejection interval
Pa(t)	Aortic pressure waveform
PAP	Peripheral artery pressure waveform
pbwd	Reflected arterial pressure wave
pfwd	Forward arterial pressure wave
PP	Pulse pressure
Ra	Total peripheral resistance
RMSE	Root-mean-squared error
RMSNE	Root-mean-squared normalized error
SP	Systolic pressure
t	time
T	Sampling period
Ts	Time duration to reach Emax from Emin
Γ	Wave reflection coefficient

CHAPTER 1

INTRODUCTION

1.1 General

The proportion of the elderly population is projected to grow at the beginning of the 21st century (see Figure (1.1)). This projection can be partly attributed to advances in biomedical technology, which have increased life expectancy. For example, new medical devices such as implanted defibrillators and stents have decreased the mortality rate following a heart attack (but have increased the prevalence of heart failure). Moreover, the elderly population contributes disproportionately to the overall prevalence of disease (see, e.g., the age distribution of critically ill patients in Figure (1.2)). Because of the evolving demographics as well as for other reasons, there is a simultaneous projected rise in the deficit of needed clinical staff (see, e.g., the nursing shortage projection in Figure (1.3)). One important implication of these projections is the need for effective and easy-to-use patient monitoring technologies for the new century.

This need is especially apparent in the context of hemodynamic monitoring of cardiovascular disease.

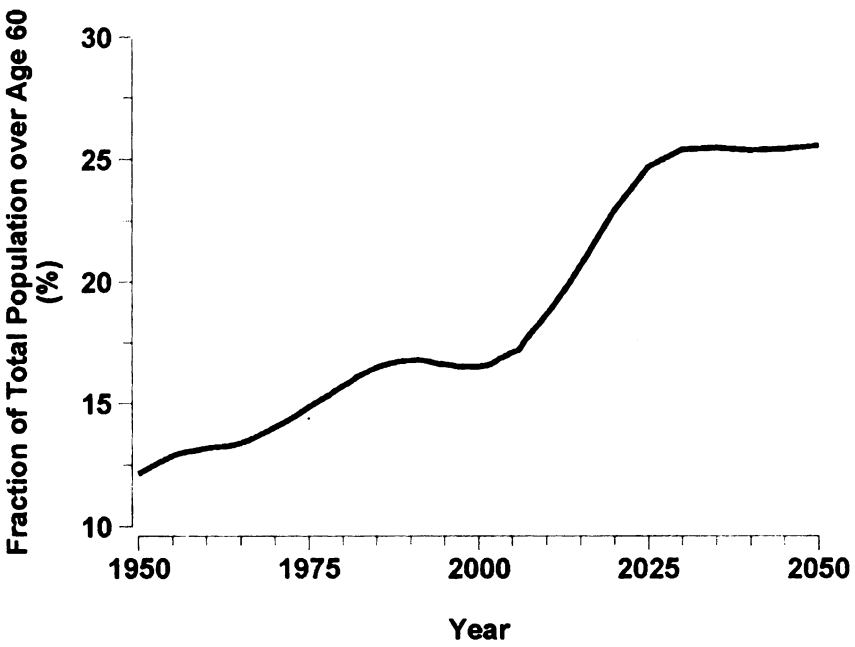

Figure 1.1 Annual percentage of the total population over the age of 60 in the Americas (Adapted from the US Census Bureau).

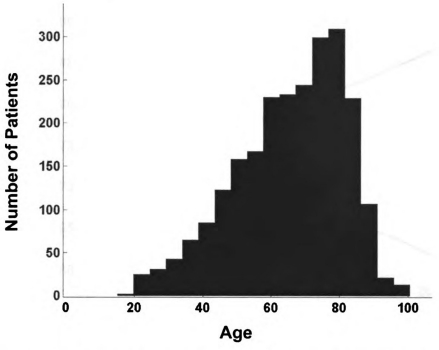

Figure 1.2 Age distribution of critically ill patients from an intensive care unit database [Saeed 2002].

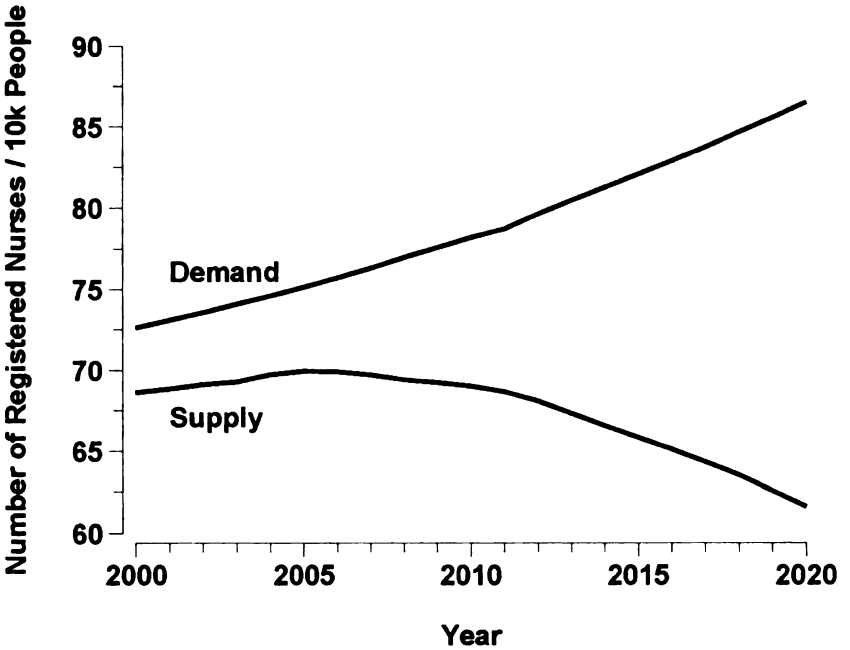

Figure 1.3 Annual national supply and demand projections for registered nurses per 10,000 people (Adapted from the US Census Bureau and Bureau of Health Professions).

1.2 Current Monitoring Techniques

Today, the workhorse in hemodynamic monitoring is the continuous measurement and display of BP waveforms. For example, invasive catheters are utilized in about 50-80% of all critically ill patients to monitor BP waveforms from peripheral arteries, especially the radial and femoral arteries. Moreover, over the past few decades, totally non-invasive methods have been developed and refined to measure peripheral ABP waveforms via finger-cuff photoplethysmography and applanation tonometry. These non-invasive methods are even available as commercial systems that are simple enough to potentially be used by patients at home (see, for example, the Finometer and Portapres, Finapres Medical Systems, The Netherlands and the T-Line Blood Pressure Monitoring System, Tensys Medical Inc., San Diego, CA). Finally, new systems are continually in development with much promise for future expansion of BP waveform monitoring. For example, it may be possible one day to chronically monitor peripheral ABP waveforms with simple wearable ring sensors. However, while these systems are continuous and offer a level of invasiveness suitable for routine clinical use, they are limited in that the measured and displayed BP levels are not very good indicators of circulatory status.

One reason is that BP levels in the peripheral arteries are not as clinically relevant as its counterpart in the central aorta. (Note that catheterization of the central aorta is too invasive and risky for routine clinical practice, as blood clot formation and embolization here could lead to, for example, a stroke.) In particular, central ABP levels would be preferred to peripheral ABP levels, as the latter are significantly distorted by highly complex wave reflections (see below). For example, both systolic pressure and pulse pressure (PP, systolic minus diastolic pressure) are amplified in peripheral ABP

waveforms, with the extent of the amplification dependent on the particular peripheral site and circulatory state. Thus, it is the systolic and diastolic pressures measured specifically in the aorta that truly reflect cardiac afterload and perfusion. Perhaps, as a result, central measurements of systolic pressure and PP have been shown to be superior in predicting patient outcome than corresponding measurements made in more peripheral arteries.

Another reason is that BP levels do not provide an early indicator of changes in circulatory status. For example, in the early stages of a bleed, the cardiovascular control system maintains ABP at the expense of other hemodynamic variables (most notably CO) in order to adequately perfuse all tissue beds of the body (see Figure (1.4)). While frank hypotension may eventually occur (see Figure (1.4)), it is often too late to intervene at this point (e.g., irreversible hemorrhagic shock). Thus, ABP levels do not provide as early an indicator of circulatory changes as CO and, as a result, may not permit sufficient time for successful therapy.

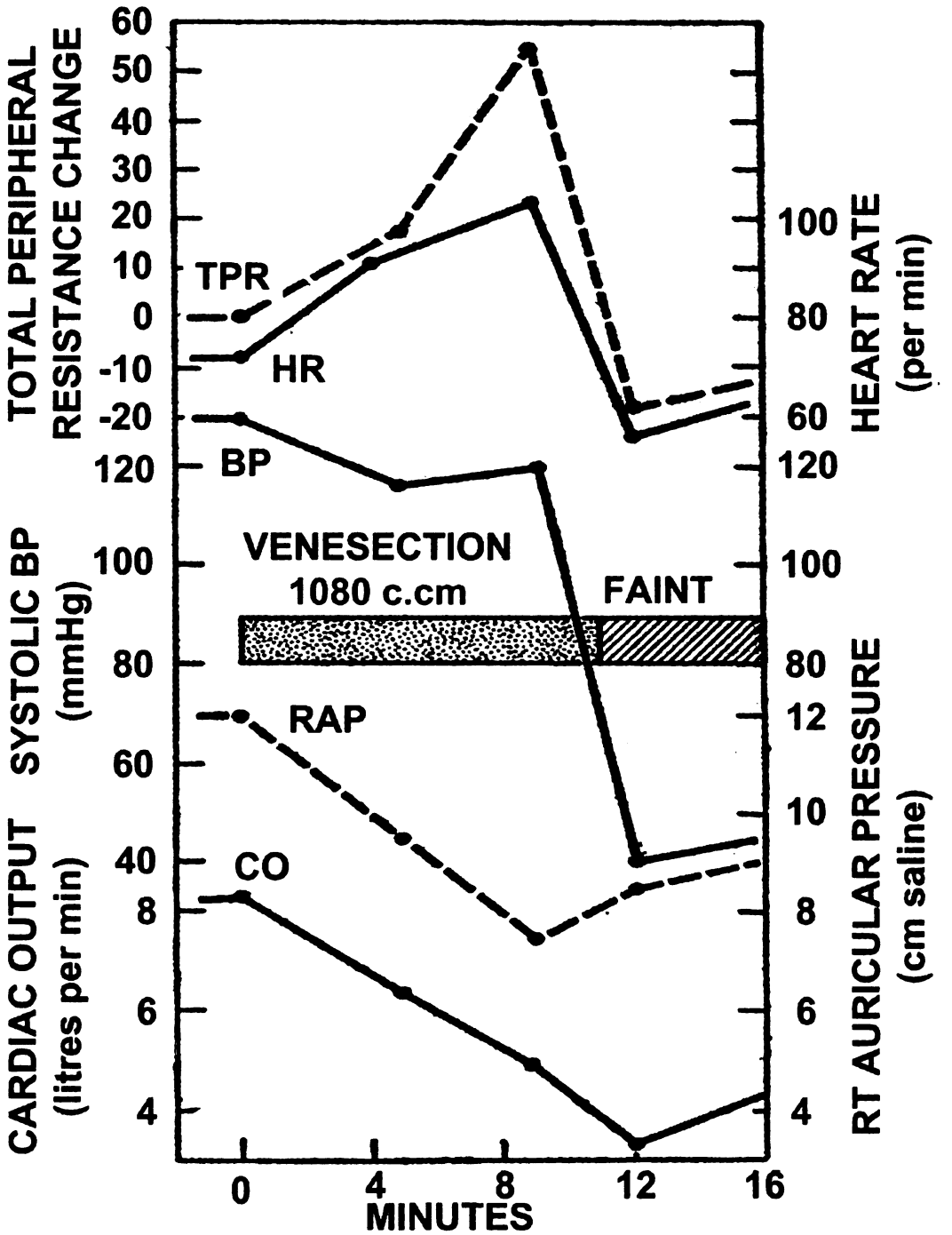

Figure 1.4 In the early stages of a bleed, arterial BP (ABP) is maintained even while cardiac output (CO) is falling due to the cardiovascular control system. Thus, ABP levels do not provide an early indicator of harmful changes in circulatory status and, as a result, may not provide enough time for successful therapy (adapted from [Barcroft 1944]).

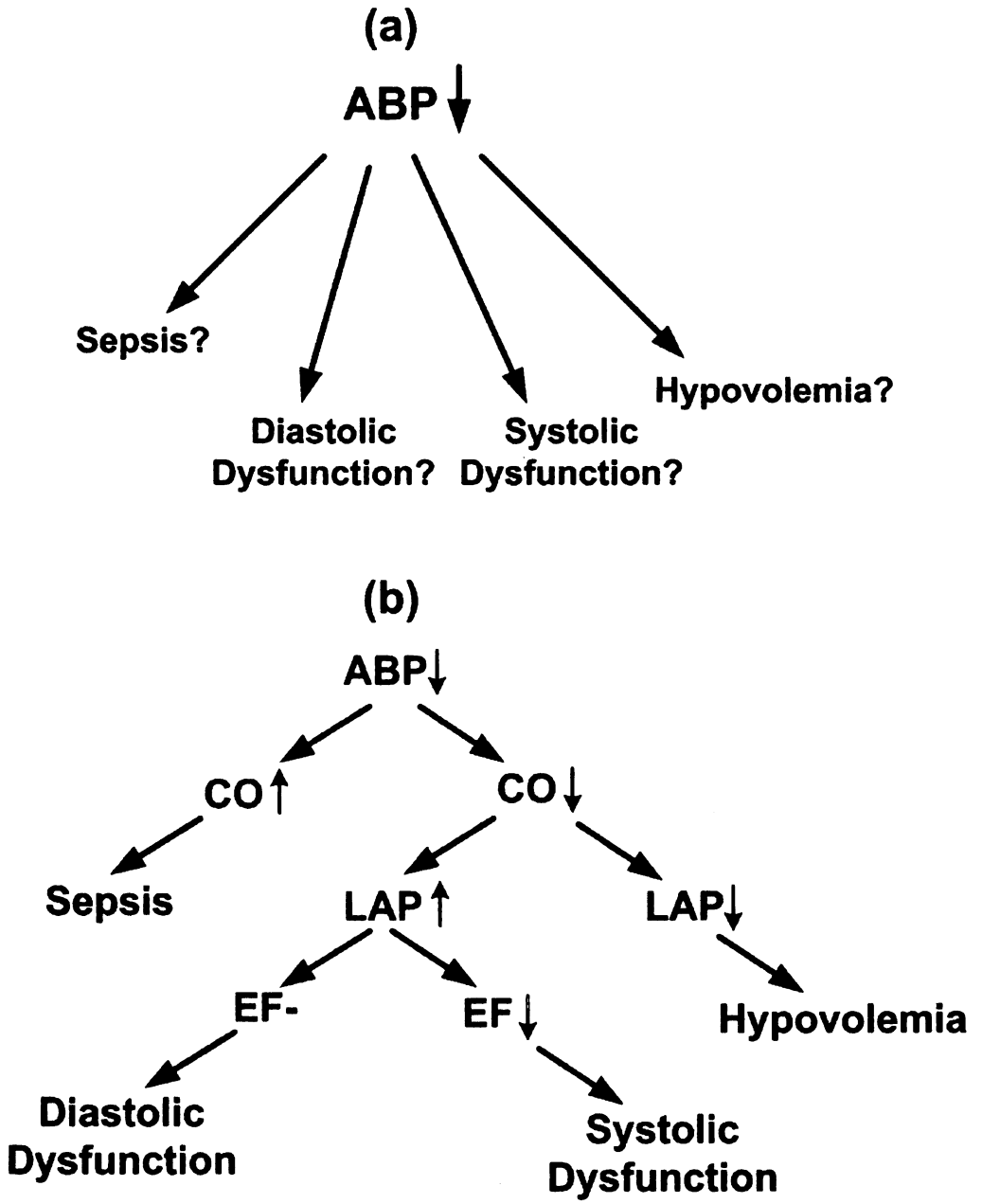

Figure 1.5 ABP levels are not sufficiently specific to permit diagnosis and guide therapy. However, a differential diagnosis may be obtained by also monitoring CO, left atrial pressure (LAP), and left ventricular ejection fraction (EF).

A third reason is that BP levels are dependent on multiple physiologic factors and are therefore not sufficiently specific to permit diagnosis and direct therapy. For example, when the cardiovascular control system eventually fails so as to result in hypotension, this could indicate sepsis (low vascular resistance due to bacterial blood poisoning), diastolic dysfunction (reduced cardiac filling due to, e.g., tamponade), systolic dysfunction (weakened cardiac contraction due to, e.g., a heart attack), or hypovolemia (due to, e.g., an internal bleed). To distinguish amongst these possibilities so as to guide therapy, it is well known that the CO, LAP, and EF must also be monitored (see Figure (1.5)). Note that EF has also proven to be a powerful predictor of outcome in heart failure patients.

The standard clinical method for monitoring CO involves the use of the balloon-tipped, flow-directed pulmonary artery catheter. CO is specifically estimated via the bolus thermodilution method. This method involves injecting a bolus of cold saline in the right atrium, measuring temperature downstream in the pulmonary artery, and computing the average CO based on conservation laws. The standard clinical method for monitoring EF (i.e., the ratio of the stroke volume (SV) to the left ventricular end-diastolic volume (EDV)) is by imaging the left ventricular volume. Commonly employed imaging methods include echocardiography, radionuclide techniques (first pass or equilibrium), contrast angiography, ultra-fast computed tomography (CT), and magnetic resonance imaging. However, these clinical methods generally share the major limitation of requiring a trained operator for their implementation. While alternative measurement methods are available, these methods suffer from substantial limitations that have generally prevented them from supplanting the operator-dependent methods in clinical

practice (see Table (1.1)). Thus, the monitoring of these three critical central hemodynamic variables is limited today and likely to be even more so in the new century.

Table 1.1 Alternative conventional methods for monitoring CO, LAP, and EF. These methods suffer from substantial disadvantages that have generally prevented them from supplanting the standard operator-dependent methods employed in clinical practice, namely bolus thermodilution, pulmonary capillary wedge pressure, and imaging. 1

Hemo-dynamic variable	Measurement Method	Advantages	Disadvantages
CO	aortic flow probe	continuous accurate	thorocotomy
	continuous thermodilution	continuous, with estimates of right ventricular ejection fraction	less accurate than bolus thermodilution
	doppler ultrasound	non-invasive	expert operator expensive
	oxygen fick	accurate inexpensive	two catheterizations operator
	thoracic bioimpedance	non-invasive continuous	inaccurate, especially in critically ill patients
EF	conductance catheter	continuous	too invasive and risky repeated calibrations
	non-imaging nuclear monitor	non-invasive continuous	too difficult to position
	sonomicrometry	continuous	thorocotomy, with crystals sutured to the ventricle

1.3 Dissertation layout

To address the above limitations we propose several techniques to mathematically estimate the central hemodynamic parameters from routinely measured blood pressure waveforms.

The rest of the dissertation is organized as follows. Chapter 2 describes a technique to estimate the central ABP from two or more peripheral artery pressure waveforms. The technique is based on multi-channel blind system identification in which two or more measured outputs (peripheral artery pressure waveforms) of a single input, multi-output system (arterial tree) are mathematically analyzed so as to reconstruct the common unobserved input (central aortic pressure waveform) to within an arbitrary scale factor. The technique then invokes Poiseuille's law to calibrate the reconstructed waveform to absolute pressure. Chapter 3 proposes a refinement to this technique wherein more efficient representations of arterial tree transfer functions are utilized to reduce the reconstruction error. This reduction in error permits beat-to-beat cardiac output to be estimated from the reconstructed central ABP waveform with high accuracy. Chapter 4 lays the foundation for wave reflection analysis in which measured aortic and peripheral artery pressure waveforms are represented in a transmission line model to estimate the forward and backward pressure and flow waves in the arterial tree. This model in conjunction with the knowledge that aortic flow is zero during diastole is utilized in chapter 5 to estimate the central ABP waveform from a single peripheral artery pressure waveform. Chapter 6 utilizes a Windkessel model for the arterial tree and a variable capacitance model for the left ventricle to derive the ejection fraction and proportional

left ventricular elastance from measurement of a central ABP waveform. Finally, some conclusions and directions for future research are outlined in chapter 7.

CHAPTER 2

BLIND IDENTIFICATION OF THE CENTRAL AORTIC PRESSURE WAVEFORM FROM MULTIPLE PERIPHERAL ARTERY PRESSURE WAVEFORMS

2.1 Introduction

As the arterial pressure wave traverses from the central aorta to the peripheral arteries, its contour becomes significantly distorted due to complex wave reflections in the distributed arterial tree [O'Rourke 1991]. For example, both systolic pressure and pulse pressure usually become amplified with the extent of the amplification dependent on the particular peripheral site and state of the arterial tree [Soderstrom 2002]. Thus, it is the systolic and diastolic pressures measured specifically in the central aorta that truly reflect cardiac afterload and perfusion [Chen 1997]. Perhaps, as a result, central measurements of systolic pressure and pulse pressure have been shown to be superior in predicting patient outcome than corresponding measurements made in more peripheral arteries [Safar 2002, Wadell 2001]. Moreover, since central aortic pressure is not significantly complicated by the wave reflections [Bourgeois 1976, Noordergraf 1978], the entire waveform clearly reveals the cardiac ejection interval through the dichrotic notch [Fetics 1999].

The measurement of the central aortic pressure waveform usually involves introducing a catheter into a peripheral artery and guiding the catheter against the flowing blood to the central aorta. However, placement of an aortic catheter is not commonly

performed in clinical practice [Chen 1997] because of the risk of blood clot formation and embolization. On the other hand, related, but distorted, peripheral artery pressure waveforms may be measured less invasively and more safely via placement of a catheter in a distal artery. Indeed, radial and femoral artery catheterizations are routinely performed in clinical practice [Marino 1998]. Moreover, over the past few decades, totally non-invasive methods have been developed and refined to continuously measure peripheral artery pressure based on finger-cuff photoplethysmography [Imholz 1998] and applanation tonometry [Kenner 1988]. These non-invasive methods are even available as commercial systems at present (see, for example, the Finometer and Portapres, Finapres Medical Systems, The Netherlands and the T-Line Blood Pressure Monitoring System, Tensys Medical Inc., San Diego, CA).

Several techniques have therefore been recently developed to mathematically derive the clinically more relevant central aortic pressure waveform from less invasively measured peripheral artery pressure waveforms. Most of these techniques have involved 1) initially obtaining simultaneous measurements of central aortic and peripheral artery pressure waveforms in a group of subjects; 2) estimating a group-averaged transfer function relating the measured peripheral artery pressure to the measured central aortic pressure; and 3) subsequently applying this transfer function to peripheral artery pressure measured from a new subject in order to predict the unobserved central aortic pressure waveform [Soderstrom 2002, Chen 1997, Fetics 1999, Karamanoglu 1993]. The principal assumption underlying these "generalized transfer function" techniques is that arterial tree properties are constant over all time and between all individuals. Because of known inter-subject and temporal variability of the arterial tree, a few techniques have

been more recently proposed towards partial individualization of the transfer function relating peripheral artery pressure to central aortic pressure through modeling [Karamanoglu 1997, Sugimachi 2001, Segers 2000].

It would be desirable to be able to estimate the central aortic pressure waveform from peripheral artery pressure in an entirely patient and time specific manner. One possible way to do so is with the multi-channel blind system identification (MBSI) approach of recent interest in signal processing [Abed-Meraim 1997, Xu G 1995]. In this approach, two or more outputs of a single input, multi-output system are analyzed so as to reconstruct the common input. To our knowledge, the very recent study by McCombie et al. represents the first application of MBSI to the field of hemodynamic monitoring [Mc Combie 2005]. However, their study specifically aimed to estimate the shape of the aortic flow waveform from peripheral artery pressure measurements (see Discussion section).

In this study, we introduce a new technique to reconstruct the central aortic pressure waveform from multiple peripheral artery pressure waveform measurements without the need for a generalized transfer function using the MBSI approach. We then demonstrate the validity of the MBSI technique with respect to four swine in which femoral and radial artery pressure waveforms and a reference central aortic pressure waveform were simultaneously measured during diverse hemodynamic interventions.

2.2 MBSI Technique

Our technique, which was initially presented in abbreviated form in [Swamy 2006], applies standard MBSI algorithms from the signal processing literature [Abed-Meraim 1997, Xu 1995] to two or more peripheral artery pressure waveforms in order to

reconstruct the central aortic pressure waveform to within an arbitrary scale factor and then calibrates the reconstructed waveform to absolute pressure based on known physiology. Below, we describe the technique at a conceptual level while stating its underlying assumptions. See the next section for the mathematical derivation and the Discussion section for a justification of its assumptions.

Figure (2.1) (dark lines and fonts) illustrates the single input, multi-output model of the pressure waveforms in the arterial tree upon which the technique is based. Here, the m (> 1) measured and sampled peripheral artery pressure waveforms ($p_{pi}(t), 1 \leq i \leq m$) are modeled as outputs of m unknown systems or channels driven by the common unobserved and likewise sampled central aortic pressure waveform ($p_{ca}(t)$) input. Each of the discrete-time channels coupling the common input to each of the distinct outputs characterizes the dynamic properties of a different arterial tree path. These channels are assumed to be linear and time-invariant (LTI) over each one-minute interval of analysis (see Methods section). The LTI channels are further assumed to be well approximated by impulse responses (i.e., time-domain version of transfer functions; ($h_i(t), 1 \leq i \leq m$) that are finite in duration and different from each other.

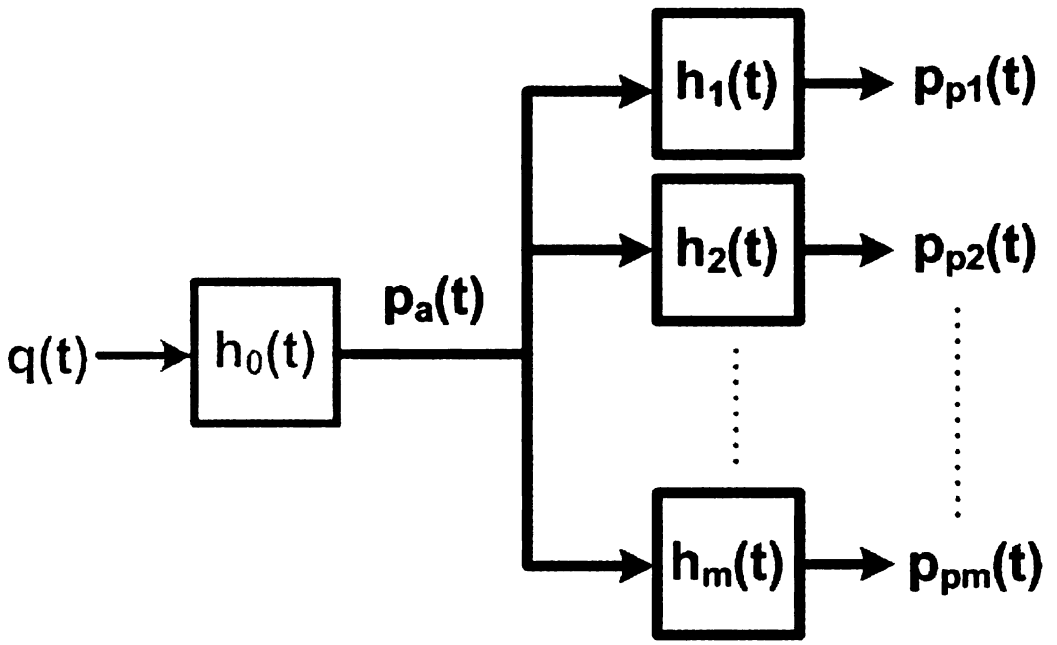

Figure 2.1 The dark lines and fonts illustrate the single input, multi-output model of the arterial tree upon which the multi-channel blind system identification (MBSI) technique introduced herein is based. The gray line and fonts represent a contemporary model [Mc Combie 2005], where the unobserved aortic flow waveform is regarded as the input.

Different here precisely means that the finite impulse responses (FIRs) are coprime with each other (i.e., the Z-transforms of the impulse responses share no common zeros or roots). In this way, all of the commonality in the measured outputs may be attributed to the input, and the differences in the measured outputs (see Discussion section) may then be deciphered so as to estimate the FIRs and ultimately reconstruct the common central aortic pressure waveform input. Note that it is generally impossible to determine the scale factor of the FIRs and therefore the common input, because any scaling of the common input may be offset with a reciprocal scaling of the FIRs. Thus, physiologic knowledge must also be employed to clarify the ambiguity.

More specifically, first, the FIRs are mathematically estimated based on the cross relations between pairs of measured outputs. These cross relations may be derived from the fundamental properties of the convolution operation governing LTI input-output behavior as follows:

$$p_{pi}(t) \otimes h_j(t) = (p_{ca}(t) \otimes h_i(t)) \otimes h_j(t) =$$
$$h_i(t) \otimes (p_{ca}(t) \otimes h_j(t)) = h_i(t) \otimes p_{pj}(t),$$

where $i \neq j$ and $\otimes$ denotes the convolution operation. The FIRs are specifically estimated to within an arbitrary scale factor by solving the homogenous system of equations resulting from the cross relations using the convenient eigenvector algorithm [Xu 1995]. The implicit assumption here is that the central aortic pressure waveform input is persistently exciting of high enough order (i.e., containing at least as many frequency components as the number of estimated FIR samples) [Xu 1995].

Then, the central aortic pressure waveform input is reconstructed to within an arbitrary scale factor by deconvolving the estimated FIRs from the measured peripheral

artery pressure waveforms. In particular, a single reconstructed waveform is obtained by employing a multi-channel least squares deconvolution algorithm [Abed-Meraim 1997].

Finally, the reconstructed waveform is calibrated to absolute pressure by scaling it to have the same mean value as the measured peripheral artery pressure. This scaling step is well justified, since the paths from the central aorta to peripheral arteries offer very little resistance to blood flow due to Poiseuille's law [Noordergraf 1978].

It should be noted that the reconstructed absolute central aortic pressure waveform will be slightly delayed with respect to the actual central aortic pressure waveform, because the time delay shared by the FIRs cannot be identified with MBSI. However, this delay, which is usually < 0.1 sec, is not important for most clinical applications.

2.3 Mathematical Derivation

We outline below the mathematical steps of the MBSI technique for the simplest case in which two peripheral artery pressure waveforms are analyzed. See [Abed-Meraim 1997, Xu 1995] for a more general mathematical treatment of the employed MBSI algorithms.

First, the FIRs in Figure (2.1) (dark lines and fonts) are mathematically estimated to within an arbitrary scale factor based on the following cross relation between the two measured outputs:

$$\sum_{k=0}^{L-1} h_1(k) * p_{p2}(t-k) - \sum_{k=0}^{L-1} h_2(k) * p_{p1}(t-k) = e(t), \quad t \in [L-1, N-1]. \tag{2.1}$$

Here, the convolution sum has been explicitly written (rather than using shorthand notation as in the initial cross relation equation of the manuscript), and the term e(t) has been included to account for any measurement noise and/or modeling error. The

variables L and N in Equation (2.1) respectively represent the number of samples of each FIR (channel order) and the number of measured peripheral artery pressure waveform samples. This equation can be expressed in matrix form by stacking each individual equation corresponding to each time t, one on top of the other, as follows:

$$\underbrace{\begin{bmatrix} \mathbf{P}_{p2} & -\mathbf{P}_{p1} \end{bmatrix}}_{\mathbf{P}} \underbrace{\begin{bmatrix} \mathbf{h}_1 \\ \mathbf{h}_2 \end{bmatrix}}_{\mathbf{h}} = \mathbf{e}, \tag{2.2}$$

where

$$\mathbf{P}_{pi} = \begin{bmatrix} p_{pi}(0) & p_{pi}(1) & \cdots & p_{pi}(L-1) \\ p_{pi}(1) & p_{pi}(2) & \cdots & p_{pi}(L) \\ \vdots & \vdots & \ddots & \vdots \\ p_{pi}(N-L) & p_{pi}(N-L+1) & \cdots & p_{pi}(N-1) \end{bmatrix}, \quad i \in [1,2],$$

are [(N-L+1)×L] Hankel matrices comprising the respective measured output samples;

$$\mathbf{h}_i = \begin{bmatrix} h_i(L-1) & h_i(L-2) & \ldots & h_i(0) \end{bmatrix}^T, \quad i \in [1,2],$$

are [L×1] vectors specifying the samples or parameters of the two respective FIRs; and

$$\mathbf{e} = \begin{bmatrix} e(0) & e(1) & \ldots & e(N-L) \end{bmatrix}^T$$

is an [(N-L+1)×1] vector of the noise samples. For a fixed channel order L, the vector **h** in Equation (2.2) is estimated to a certain non-trivial constraint by minimizing the energy in the vector **e**. This optimization problem is specifically solved in closed-form by selecting the eigenvector associated with the minimum eigenvalue of the matrix $\mathbf{P}^T\mathbf{P}$ as a unit-energy estimate of the vector **h**. The channel order L is determined by 1) forming a **P** matrix of dimension $[(N-L_{max}+1)\times 2L_{max}]$, where $L_{max}=15$ is assumed to encompass the true channel order; 2) computing the eigenvalues of the matrix $\mathbf{P}^T\mathbf{P}$; and

3) establishing the optimal value of L as half the number of eigenvalues (rounded up when odd) that are at least 5% of the maximum eigenvalue.

Second, the common central aortic pressure waveform input in Figure (2.1) (dark lines and fonts) is determined to within an arbitrary scale factor from the two determined FIRs (i.e., the estimated vector **h**) and the two measured outputs through multi-channel least squares deconvolution. That is, the two measured outputs may be expressed in terms of their common input via the convolution sum as follows:

$$p_{pi}(t) = \sum_{k=0}^{L-1} h_i(k) p_{ca}(t-k) + n_i(t), \quad i \in [1,2], \quad t \in [0, N-1], \tag{2.3}$$

where $n_i(t)$ accounts for any noise. This equation may also be expressed in matrix form by stacking each individual equation for each t and i, one on top of the other, as follows:

$$\underbrace{\begin{bmatrix} p_{p1} \\ p_{p2} \end{bmatrix}}_{\mathbf{p_p}} = \underbrace{\begin{bmatrix} H_1 \\ H_2 \end{bmatrix}}_{\mathbf{H}} \mathbf{p_{ca}} + \underbrace{\begin{bmatrix} n_1 \\ n_2 \end{bmatrix}}_{\mathbf{n}}, \tag{2.4}$$

where

$$\mathbf{p_{pi}} = [p_{pi}(0) \quad p_{pi}(2) \quad \cdots \quad p_{pi}(N-1)]^T, \quad i \in [1,2],$$

are [N×1] vectors of the respective measured output samples;

$$\mathbf{H_i} = \begin{bmatrix} h_i(L-1) & \cdots & h_i(0) & \cdots & 0 \\ \vdots & \ddots & & \ddots & \vdots \\ 0 & \cdots & h_i(L-1) & \cdots & h_i(0) \end{bmatrix}, \qquad i \in [1,2],$$

are the [N×(N+L-1)] Toeplitz matrices including the estimated samples of the respective FIRs;

$$\mathbf{p_{ca}} = [p_{ca}(-L-1) \quad p_{ca}(-L-2) \quad \cdots \quad p_{ca}(0) \quad p_{ca}(1) \quad \cdots \quad p_{ca}(N-1)]^T$$

is a [(N+L-1)×1] vector of unmeasured common input samples; and

$$\mathbf{n_i} = \left[n_i(0) \quad n_i(1) \quad \ldots \quad n_i(N-1) \right]^T, \quad i \in [1,2],$$

are [Nx1] vectors of the respective noise samples. The vector $\mathbf{p_{ca}}$ in Equation (2.4) is then estimated to within an arbitrary scale factor by minimizing the energy in the vector $\mathbf{n}$. This optimization problem is specifically solved in closed-form using the following linear least-squares solution:

$$\mathbf{p_{ca}} = (\mathbf{H^T H})^{-1} \mathbf{H^T p_p}, \tag{2.5}$$

where the inverse here is computed efficiently as described in [Jain, 1978]. Following the deconvolution, the reconstructed input is lowpass filtered with a cutoff frequency of 10 Hz.

Third, the reconstructed waveform (i.e., the determine $\mathbf{p_{ca}}$ vector) is calibrated to absolute pressure by scaling it to have the same mean value as that of the measured peripheral artery pressure as follows:

$$p^s_{ca}(t) = p_{ca}(t) \frac{\sum_{t=0}^{N-1} p_{p1}(t)}{\sum_{t=o}^{N-1} p_{ca}(t)}. \tag{2.6}$$

Here, $\mathbf{p^s_{ca}}$ is the absolute (scaled) estimated central aortic pressure waveform.

Finally, if the average systolic pressure of the reconstructed central aortic pressure waveform is greater than that of the measured peripheral artery pressure, then the solution is considered to be invalid and the above steps are repeated but with the channel order reduced by one. We note that this technique always resulted in a valid estimate of the central aortic pressure waveform for every interval of analysis in the present swine study.

2.4 Methods

We evaluated the MBSI technique with respect to previously collected hemodynamic measurements from swine, which are described in detail elsewhere [Mukkamala 2006]. Below, we briefly describe the experimental procedures employed for collecting these hemodynamic data and then present the methods for data analysis utilized herein.

Hemodynamic Data

Six Yorkshire swine (30-34 kg) were studied under a protocol approved by the MIT Committee on Animal Care. Following the induction of general anesthesia and mechanical ventilation, physiologic transducers were placed in each animal as follows. A micromanometer-tipped catheter was fed retrograde to the thoracic aorta via a femoral artery for reference central aortic pressure. Fluid-filled catheters were then inserted in the opposite femoral artery for femoral artery pressure and in an artery as distal as possible to the brachial artery for "radial" artery pressure. Finally, an ultrasonic flow probe was placed around the aortic root following a midline sternotomy for cardiac output. In each animal, a subset of the following interventions was then performed over the course of 75 to 150 minutes to vary arterial pressures as well as other hemodynamic parameters: infusions of volume, phenylephrine, dobutamine, isoproterenol, esmolol, nitroglycerine, and progressive hemorrhage. Several infusion rates were implemented followed by brief recovery periods. The hemodynamic waveforms were continuously recorded throughout the intervention period at a sampling rate of 250 Hz and 16-bit resolution.

Data Analysis

We discarded two of the six swine datasets from the study due to excessive damping of the femoral artery pressure waveform in one dataset [Mukkamala 2006] and an

improperly calibrated reference central aortic pressure waveform in the other dataset. We then applied the technique to all one-minute, non-overlapping intervals of the femoral and radial artery pressure waveforms (resampled to 50 Hz) in the remaining four swine datasets. We evaluated the resulting central aortic pressure waveform estimates with respect to the measured reference waveforms (likewise resampled to 50 Hz) in terms of the root-mean-squared-error (RMSE = $\sqrt{\mu^2 + \sigma^2}$, where μ is the bias and σ is the precision) of the following parameters: total waveform (i.e., sample-to-sample), beat-to-beat systolic pressure, beat-to-beat pulse pressure, and beat-to-beat ejection interval. For comparison, we likewise evaluated the peripheral artery pressure waveforms with respect to the measured central aortic pressure waveforms in terms of the first three parameters. (Note that we did not attempt to determine the ejection intervals from the peripheral artery pressure waveforms, because the dichrotic notch was generally obscured by wave reflections.) Prior to conducting these evaluations, we advanced the central aortic pressure waveform estimates so that they were temporally aligned with the measured central aortic pressure waveforms. To make a fair comparison, we likewise time aligned the peripheral artery pressure waveforms.

2.5 Results

Tables (2.1) and (2.2) respectively summarize the hemodynamic parameters of the four analyzed swine datasets and the evaluation results of the MBSI technique with respect to these datasets. These tables generally indicate that the technique was able to reliably estimate the central aortic pressure waveform over a wide hemodynamic range

with a level of accuracy that was far better than no mathematical analysis of the peripheral artery pressure waveforms.

More specifically, the overall total waveform RMSE of the estimated central aortic pressure was 4.7 mmHg (after a modest time alignment as described above). For comparison, the average overall total waveform RMSE between the measured peripheral artery pressures and the measured central aortic pressure was 8.6 mmHg (after a more significant time alignment). Thus, the technique was able to effectively reduce the total wave distortion in the measured peripheral artery pressure waveforms by 45%. Furthermore, the overall beat-to-beat systolic pressure RMSE and the overall beat-to-beat pulse pressure RMSE of the estimated central aortic pressure were 7.5 mmHg and 8.2 mmHg, respectively.

Table 2.1 Hemodynamic parameters of the swine evaluation datasets. The multi-channel blind system identification (MBSI) technique was experimentally evaluated with respect to four swine in which femoral artery pressure and radial artery pressure waveforms and a reference central aortic pressure waveform were simultaneously measured over a wide hemodynamic range. MAP is mean arterial pressure; SP, systolic pressure from central aortic pressure; PP, pulse pressure from central aortic pressure; EI, ejection interval from central aortic pressure; HR, heart rate; and CO, cardiac output.

Animal	MAP Range [mmHg]	SP Range [mmHg]	PP Range [mmHg]	EI Range [ms]	HR Range [beats/min]	CO Range [L/min]
1	54 – 136	70 – 168	28 – 48	237 – 267	100 – 223	2.3 – 4.1
2	58 – 117	73 – 143	19 – 49	235 – 337	92 – 190	1.7 – 6.0
3	45 – 114	60 – 140	22 – 45	204 – 296	91 – 243	2.4 – 5.7
4	48 – 119	70 – 142	22 – 51	198 – 261	102 – 207	1.3 – 6.2
Total	45 – 136	60 – 168	19 – 51	198 – 337	91 – 243	1.3 – 6.2

Table 2.2 Summary of the experimental evaluation results of the MBSI technique with respect to the four swine datasets. Overall, the MBSI technique (see dark line and fonts in Figure (1.1)) as applied to the radial and femoral artery pressure waveforms in the four swine datasets (see Table (2.1)) reliably estimated the central aortic pressure waveform along with its clinically significant parameters and thereby significantly reduced the wave distortion in the measured peripheral artery pressure waveforms. RMSE is root-mean-squared-error; TW, total waveform; SP, systolic pressure; PP, pulse pressure; and EI, ejection interval. See example results of the MBSI technique in Figure 2.2.

Dog	Estimated Central Aortic Pressure RMSE				Femoral Artery Pressure RMSE			Radial Artery Pressure RMSE		
	TW	SP	PP	EI	TW	SP	PP	TW	SP	PP
		[mmHg]		[ms]		[mmHg]			[mmHg]	
1	4.4	4.7	4.8	82	11.6	19.2	10.5	4.0	5.1	4.9
2	4.3	5.2	6.4	57	7.8	13.5	14.3	10.5	24.5	19.2
3	4.7	6.2	8.5	55	6.3	12.0	10.2	9.4	16.7	10.3
4	5.6	7.8	7.7	67	7.0	10.7	14.3	9.3	22.7	21.6
Total	4.7	7.5	8.2	59	8.1	13.7	12.6	9.1	19.7	15.9

These errors represent an average overall improvement of 57% and 41% with respect to the corresponding parameters from the measured peripheral artery pressure waveforms. In addition, the overall beat-to-beat ejection interval RMSE of the estimated central aortic pressure was 59 msec. Finally, though not shown in the tables, the errors in the four studied parameters of the estimated central aortic pressure were virtually uncorrelated with the respective reference values of these parameters.

Figures (2.2a) and (2.2b) provide two visual examples illustrating the significant differences between the measured peripheral artery pressure waveforms (dash and dot-dash) and the corresponding measured central aortic pressure waveforms (solid), while Figures (2.2c) and (2.2d) show the resulting central aortic pressure waveforms estimated from these peripheral artery pressure waveforms (dash) along with the reference central aortic pressure waveforms (solid). As is evident in these examples at two different mean pressure levels, the estimated and reference central aortic pressure waveforms agree very closely, and much of the wave distortion in the measured peripheral artery pressure waveforms has been eliminated.

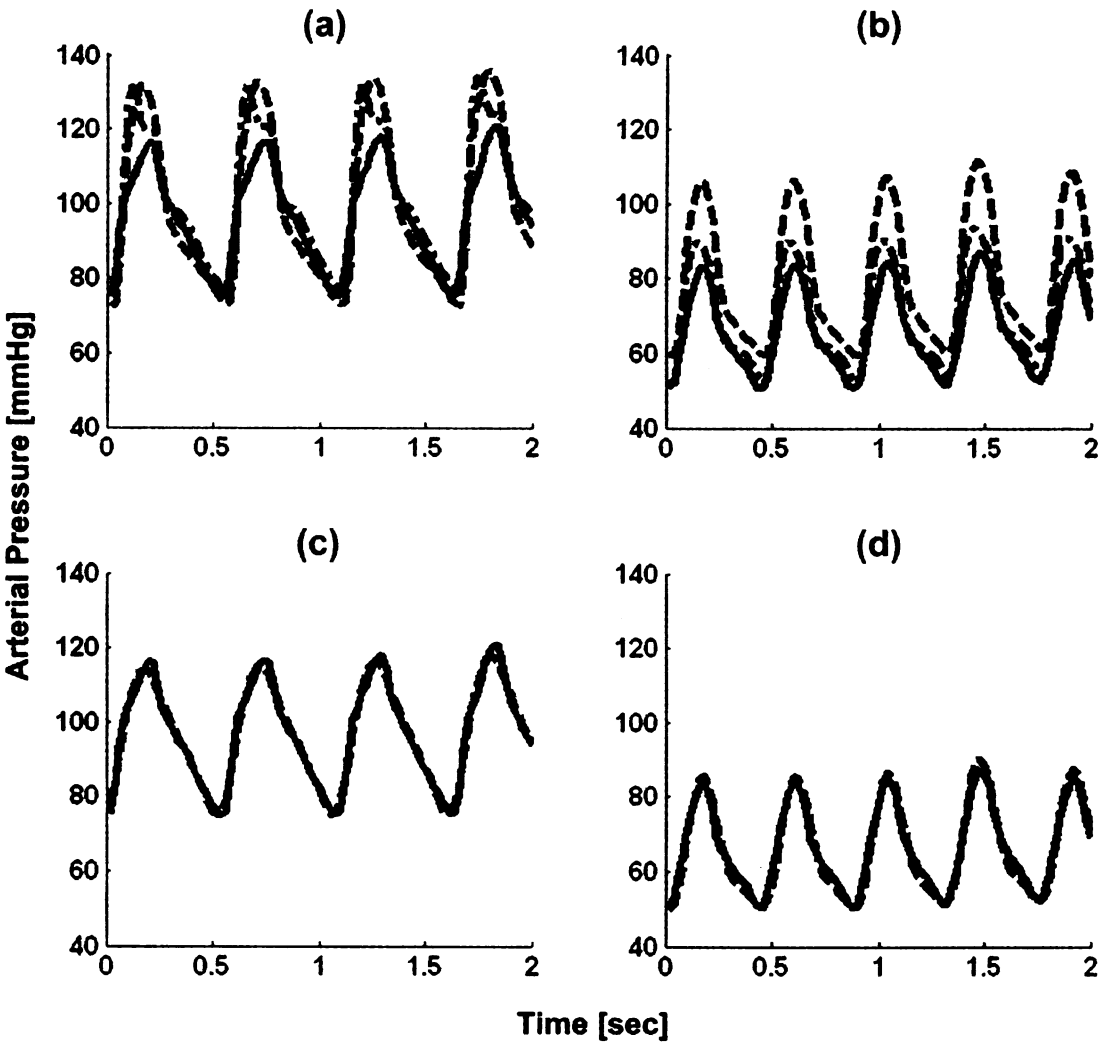

Figure 2.2 (a, b) Example segments of the measured central aortic pressure (solid), femoral artery pressure (dash), and radial artery pressure (dot-dash) waveforms from the four analyzed swine datasets (see Table (2.1)). (c, d) Example segments of the central aortic pressure waveform measured (solid) and estimated (dash) by applying the MBSI technique (see dark lines and fonts in Figure (2.1)) to the two segments of peripheral artery pressure waveforms in (a, b).

2.5 Discussions

In summary, we have introduced a new technique to mathematically reconstruct the clinically more relevant central aortic pressure waveform from multiple, less invasively measured peripheral artery pressure waveforms distorted by wave reflections. Our technique capitalizes on the powerful MBSI approach of recent interest in signal processing in which the differences in the outputs of a single input, multi-output system are assessed so as to reconstruct the common input to within an arbitrary scale factor. Then technique then calibrates the reconstructed waveform to absolute pressure using Poiseuille's law. As a result, in contrast to previous, related efforts, our technique neither employs a generalized transfer function nor requires any training data and is therefore entirely patient and time specific. We have also presented an experimental evaluation of the technique in four swine in which radial and femoral artery pressure waveforms and a reference central aortic pressure waveform were simultaneously measured over a wide hemodynamic range. Our results show that the technique was able to reliably estimate the entire central aortic pressure waveform and thereby significantly improve upon the determination of systolic pressure, pulse pressure, and the ejection interval as compared to measuring these clinically significant parameters directly from the peripheral artery pressure waveforms.

Assumptions of the MBSI Technique

As stated above, our MBSI technique is based on a set of assumptions. We make physiologic and empirical arguments to justify each of the underlying assumptions below.

Assumption 1: the channels relating the common input to each distinct output in Figure 1.1 are LTI over each one-minute interval of analysis. Over such short time

intervals, the arterial tree is usually operating in near steady-state conditions in which the statistical properties of the arterial pressure waveforms vary little over time. Such steady-state conditions clearly justify the time-invariance approximation. Moreover, these conditions also support the linearity approximation as argued in [McCombie 2005] and references therein.

Assumption 2: the LTI channels are characterized with FIRs. Although not widely appreciated, it is known that arterial pressure waveforms measured from distinct sites only differ significantly in terms of their high frequency detail while being quite similar at lower frequencies [Noordergraf 1978, Mukkamala 2006]. Thus, the dynamics of each of the channels in Figure (2.1) (dark lines and fonts) are fast (e.g., effectively vanishing within ~0.5 sec [Zhang 2002]), thereby supporting the FIR approximation.

Assumption 3: the FIRs are coprime with each other. If the FIRs were not coprime with each other, then the non-coprime or common FIR dynamics would be erroneously attributed to the common input. As discussed above, peripheral artery pressure waveforms from distinct sites in the arterial tree appear different. Thus, the dynamics of each channel cannot be the same, and the coprime channel approximation is at least somewhat tenable.

Assumption 4: the central aortic pressure waveform is persistently exciting of high enough order. This assumption means that the central aortic pressure waveform contains at least as many frequency components as the number of estimated FIR samples. As described above, the channel dynamics are short duration. Thus, the number of FIR samples to be estimated is small, thereby buttressing the persistence of excitation approximation.

Any violation to the four above assumptions in the present swine study may indeed represent a source of error of our MBSI technique. However, we note that each of the assumptions must have been at least largely valid here given that the discrepancy between the estimated and reference central aortic pressure waveforms was relatively small (see Table (2.2)).

MBSI Technique in the Context of Previous Efforts

The MBSI technique that we have introduced herein was inspired by the seminal contributions of several previous investigations described in the hemodynamic monitoring literature. In particular, the idea of mathematical deriving central aortic pressure from measured peripheral artery pressure stems from the body of generalized transfer function literature [Soderstrom 2002, Chen 1997, Fetics 1999, Karamanoglu 1993, Karamanoglu 1997, Sugimachi 2001, Segers 2000], whereas the idea of employing MBSI to do so in an entirely patient and time specific manner is based on the very recent study by McCombie et al. [McCombie 2005].

McCombie et al. specifically proposed a technique using MBSI to reconstruct the shape of the common aortic flow waveform input from multiple peripheral artery pressure waveform outputs and demonstrated its feasibility in a pilot swine experiment. Figure (2.1) (all lines and fonts) illustrates the single input, multi-output model upon which their technique was based. As can be seen from this model, the channels coupling the aortic flow waveform to each peripheral artery pressure waveform include common dynamics, namely the channel relating the aortic flow waveform to the central aortic pressure waveform ($h_0(t)$), and are therefore not coprime. As a result, these investigators had to develop additional signal processing to estimate the common channel

dynamics, which resulted in a considerably more complicated algorithm than standard MBSI. Moreover, their framework did not provide an obvious means to determine the uncontrolled scale factor of the reconstructed input. Thus, the technique cannot be utilized to monitor relative changes in cardiac output. In contrast, our MBSI technique aimed to estimate the central aortic pressure waveform input in which the coprime channel assumption is more tenable (thereby rendering a relatively straightforward algorithm) and the arbitrary scale factor of the input is conveniently determined by invoking Poiseuille's law.

It is not strictly valid to compare the results of the MBSI technique reported here with those of previous studies employing generalized or partially individualized transfer functions due to variations in evaluation datasets (both subjects and experimental conditions) and methods for evaluation. Nevertheless, we find that the total central aortic pressure waveform error of 4.7 mmHg obtained by our technique (see Table (2.2)) is somewhat higher than the approximately 2 to 4 mmHg errors reported in four of the previous studies [Chen 1997, Fetics 1999, Karamanoglu 1993, Karamanoglu 1997]. However, we note that the transfer functions that were utilized in each of these studies were trained on the same subjects and/or the same experimental conditions that were subsequently employed for testing. The impetus for the present research is that the MBSI technique should demonstrate an improved performance when applied to the diverse population of patients and patho-physiologic conditions seen in clinical practice. On the other hand, we acknowledge that the cost of this potential improvement in accuracy is the requirement of more than one peripheral artery pressure waveform for analysis. However, several convenient methods are currently available for measuring peripheral

artery pressure waveforms (see above) and new systems are continually in development. For example, it may be possible one day to chronically monitor peripheral artery pressure waveforms with wearable ring sensors [Asada 2003].

Future Directions

The present study opens up the possibility of several different avenues of future investigation. In terms of subsequent mathematical efforts, it would be worthwhile to attempt to improve upon the accuracy of the MBSI technique by compactly representing the FIR channels with more appropriate basis functions and thereby alleviate the persistence of excitation demands. In addition, it would be extremely desirable, from a clinical point of view, to be able to extend the MBSI technique to also estimate relative changes in aortic flow through, for example, physical modeling. In terms of subsequent experimental efforts, it may prove useful to seek correlation between the estimated FIR channels and phenomena that are local to the respective peripheral artery pressure measurement sites (e.g., plaque development) so as to further extend the monitoring capabilities of the technique. Furthermore, while the application of the technique to femoral and radial artery pressure waveforms may be most suitable for clinical practice (see above), it would be interesting, from a scientific point of view, to establish the optimal sites and number of peripheral artery pressure measurements (e.g., the arterial tree sites that result in the most coprime channels and the smallest number of measurements that does not significantly compromise estimation accuracy). Finally, future evaluations of the MBSI technique in humans and with respect to non-invasive peripheral artery pressure waveforms are certainly warranted.

Potential Applications of the MBSI Technique

Our MBSI technique mathematically derives the clinically more relevant central aortic pressure waveform from multiple, less invasively measured, but distorted, peripheral artery pressure waveforms without using any training data. The technique may easily be implemented in near real time (with a one minute delay) using a standard home personal computer. With further development and successful testing, the technique may ultimately be utilized for more precise monitoring and titration of therapy [Chen 1997] in, for example, critically ill patients with invasive catheters installed and hypertension patients instrumented with non-invasive arterial pressure transducers. Advancements in arterial pressure monitoring technology hold further promise for the application of the technique in the context of chronic ambulatory and home monitoring.

CHAPTER 3

ESTIMATION OF THE AORTIC PRESSURE WAVEFORM AND BEAT-TO-BEAT CARDIAC OUTPUT FROM MULTIPLE PERIPHERAL ARTERY PRESSURE WAVEFORM

3.1 Introduction

Blood ejected by the left ventricle initiates pressure and flow waves that propagate through the arterial tree. These waves are reflected at multiple sites of impedance mismatch caused by arterial bifurcations, narrowing, and stiffening [Donald 1960], [Noordergraf 1978]. For example, wave reflections are especially pronounced at the sites of arterial terminations [Donald 1960, Westerhof 1972]. The pressure waveform measured at a given site in the arterial tree therefore represents the sum of the forward and backward traveling pressure waves at that particular site [Westerhof 1972, Berger 1993]. As a result, the arterial pressure waveform becomes progressively distorted as its site of measurement becomes more distal to the aorta [Donald 1960]. Most notably, systolic pressure (SP) and pulse pressure (PP) become increasingly amplified [Donald 1960, Soderstrom 2002] and therefore less indicative of cardiac performance [Chen 1997]. Indeed, central measurements of SP and PP have been shown to be superior predictors of patient outcome than corresponding measurements made in more peripheral arteries [Safar 2002, Wadell 2001]. In addition, aortic pressure (AP, especially from the descending thoracic aorta) is less complicated by wave reflections than peripheral artery pressure (PAP) due in part to attenuation and destructive interference of the reflected

waves that reach the aorta [Noordergraf 1978, Bourgeois 1974, Bourgeois 1976]. Thus, the entire AP waveform usually reveals the ventricular systolic ejection interval (SEI) through the dicrotic notch [Fetics 1999] and may be represented with a lumped parameter Windkessel model in order to accurately estimate beat-to-beat relative changes in cardiac output (CO), as convincingly demonstrated in [Bourgeois 1976]. On the other hand, PAP may be measured more safely than AP through catheterization and even non-invasively via finger-cuff photoplethysmography [Imholz 1998] or applanation tonometry [Kenner 1998]. It is therefore PAP waveforms that are routinely monitored in humans [Marino 1998], even though the AP waveform is known to be of greater clinical value.

As a result, over the past 15 years, there has been considerable interest in estimating the AP waveform from measured PAP waveforms using generalized transfer function techniques [Soderstrom 2002, Chen 1997, Fetics 1999, Karamanoglu 1993, Karamanoglu 1996]. These techniques essentially involve: 1) initially obtaining simultaneous measurements of AP and PAP waveforms in a group of subjects; 2) estimating a group-averaged transfer function relating the measured PAP to the measured AP; and 3) subsequently applying this transfer function to PAP measured from a new subject in order to estimate the AP waveform. However, these techniques do not account for known inter-patient and temporal variability of arterial tree properties (e.g., [Hallock 1937, Guyton 1996]) and may therefore be prone to significant estimation error when applied to the diverse patient population encountered in clinical practice.

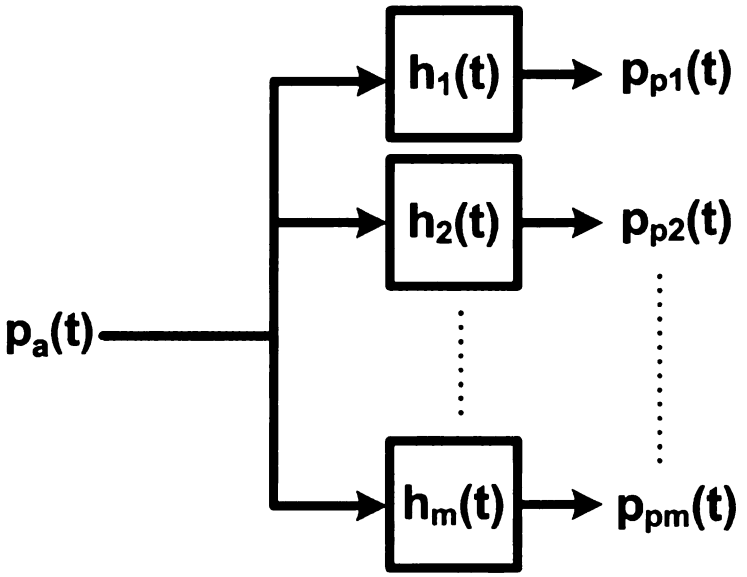

Figure 3.1 Single input, multi-output model of the arterial tree providing the basis for the technique introduced herein to estimate the clinically more relevant aortic pressure (AP) waveform from multiple, less invasively measured peripheral artery pressure (PAP) waveforms distorted by wave reflections.

We have recently developed a patient and time specific technique for estimating the AP waveform from multiple PAP waveforms by capitalizing on the powerful multi-channel blind system identification (MBSI) approach [Swamy 2007]. The technique specifically involves: 1) modeling two or more measured PAP waveforms as outputs of distinct finite impulse response (FIR) channels driven by the common AP waveform input (see Figure (3.1)); 2) estimating the FIRs to within an arbitrary scale factor by applying the standard eigenvector method to the cross relations between pairs of measured outputs (see Equations (3.1) and (3.2)); 3) reconstructing the AP waveform to within an arbitrary scale factor by deconvolving the estimated FIRs from the measured waveforms; and 4) scaling the reconstructed waveform to absolute pressure by invoking Poiseuille's law. In this way, the technique is able to estimate the AP waveform from PAP waveforms without the need for a generalized transfer function. We have tested this technique with respect to four swine datasets consisting of simultaneous measurements of two PAP waveforms from the femoral and radial arteries and a measured reference AP waveform during diverse hemodynamic interventions [Swamy 2007]. Our results showed that the technique provided more accurate AP waveform estimates than a generalized transfer function developed from a subset of the same datasets. In this paper, we introduce an improved technique for estimating the AP waveform as well as beat-to-beat relative changes in CO from multiple PAP waveforms. The technique specifically involves: 1) estimating the AP waveform based on our new MBSI method in which the FIRs are represented with more efficient basis functions than the impulse basis functions assumed by the standard eigenvector method in order to reduce the number of parameters to be estimated and therefore enhance the estimation accuracy; and 2) estimating beat-to-

beat relative changes in CO by fitting a Windkessel model to the estimated AP waveform in which wave distortion should be greatly attenuated. We show that this new technique is able to estimate the AP waveforms in the four aforementioned swine datasets with greater accuracy than our initial technique. We further show that this enhanced accuracy permits reliable estimation of beat-to-beat relative changes in CO as compared to gold standard reference aortic flow probe measurements also available in the swine datasets.

3.2 Technique

Our technique applies a new MBSI method that we have developed to two or more PAP waveforms to estimate the AP waveform and then fits a Windkessel model to the estimated waveform to estimate beat-to-beat relative changes in CO. We fully describe the technique below for the simplest case in which two PAP waveforms are available for analysis. Generalization of the technique to more than two measured waveforms readily follows analogous to [Xu 1995].

First, two measured and sampled PAP waveforms ($p_{pi}(t)$, $i \in [1, 2]$) are modeled as individual outputs of two unknown channels driven by the common unknown and likewise sampled AP waveform ($p_a(t)$) input as shown in Figure 1 with $m = 2$. The two discrete-time channels coupling the common input to the two distinct outputs represent the dynamic properties of a different path in the arterial tree. A principal assumption underlying the model is that the channels may be well characterized by coprime FIRs ($h_i(t)$, $i \in [1, 2]$) over each one-minute interval of analysis (see below). Over such short time intervals, the arterial tree is usually operating in near steady-state conditions, thereby clearly supporting the implicit time invariance assumption as well as buttressing the

implicit linearity assumption as argued in [McCombie 2005] and references therein. Moreover, since pressure waveforms measured from distinct sites in the arterial tree only differ significantly over short time scales (e.g., within a cardiac cycle) while being quite similar over longer time scales (e.g., mean values as described below) [Noordergraf 1975, Zhenwei 2006], the FIR assumption is also well justified. Finally, the coprime assumption, which is needed to subsequently estimate the FIRs [Xu 1995], may be largely valid due to the significant differences in PAP waveforms measured from distinct arterial sites.

Then, by applying the fundamental properties of convolution to the single input, multi-output model of Figure (3.1), the two FIRs may be estimated based on the resulting cross relation between the two measured outputs:

$$\sum_{\tau=0}^{L-1} h_1(\tau) * p_{p2}(t-\tau) - \sum_{\tau=0}^{L-1} h_2(\tau) * p_{p1}(t-\tau) = e(t), \quad t \in [L-1, N-1]. \tag{3.1}$$

Here, e(t) accounts for any measurement and/or modeling error, and the variables L and N respectively represent the maximum duration of the FIRs (channel order) and the number of measured PAP waveform samples in a one-minute interval of analysis [Xu 1995].

The standard method for estimating the FIRs in Equation (3.1) is to first determine the channel order through eigenvalue analysis and then to estimate the FIR samples or parameters to within an arbitrary scale factor by least squares minimization of e(t) via the eigenvector method [Xu 1995]. More specifically, Equation (3.1) may be expressed in matrix form by stacking each individual equation, corresponding to each t, one on top of the other as follows:

$$\underbrace{\begin{bmatrix} \mathbf{P}_{p2} & -\mathbf{P}_{p1} \end{bmatrix}}_{\mathbf{P}} \underbrace{\begin{bmatrix} \mathbf{h}_1 \\ \mathbf{h}_2 \end{bmatrix}}_{\mathbf{h}} = \mathbf{e}, \tag{3.2}$$

where

$$\mathbf{P}_{pi} = \begin{bmatrix} p_{pi}(0) & p_{pi}(1) & \cdots & p_{pi}(L-1) \\ p_{pi}(1) & p_{pi}(2) & \cdots & p_{pi}(L) \\ \vdots & \vdots & \ddots & \vdots \\ p_{pi}(N-L) & p_{pi}(N-L+1) & \cdots & p_{pi}(N-1) \end{bmatrix}, \quad i \in [1,2], \tag{3.3}$$

are [(N-L+1)×L] Hankel matrices comprising the respective measured output samples; $\mathbf{h_i} = \begin{bmatrix} h_i(L-1) & h_i(L-2) & \cdots & h_i(0) \end{bmatrix}^T$, $i \in [1,2]$, are [L×1] vectors specifying the parameters of the two respective FIRs; and $\mathbf{e} = \begin{bmatrix} e(0) & e(1) & \cdots & e(N-L) \end{bmatrix}^T$ is an [(N-L+1)×1] vector consisting of the error samples. The channel order L may then be determined by 1) forming a matrix $\mathbf{P}$ of dimension $[(N-L_{max}+1)\times 2L_{max}]$, where L_{max} is assumed to encompass the true channel order; 2) computing the eigenvalues of the matrix $\mathbf{P}^T\mathbf{P}$; 3) identifying the number of insignificant eigenvalues n_{ie}; and 4) selecting the optimal value of L as $L_{opt} = L_{opt} - (n_{ie} - 1)$. Then, the least squares, unit two-norm estimate of the vector $\mathbf{h}$ may be conveniently obtained by selecting the eigenvector associated with the minimum eigenvalue of the matrix $\mathbf{P}^T\mathbf{P}$, where $\mathbf{P}$ is of dimension $[(N-L_{opt}+1)\times 2L_{opt}]$. The implicit assumption of this standard eigenvector method, which was employed by our initial MBSI technique [Swamy 2007], is that the AP waveform contains at least as many frequency components as the number of estimated FIR parameters $2L_{opt}$ [Xu 1995].

To reduce the number of parameters to be estimated so as to alleviate the frequency content demands on the AP waveform and thereby improve the estimation accuracy, the FIRs are instead compactly represented with damped sinusoidal basis functions as follows:

$$h_i(t) = \sum_{k=1}^{n} \lambda^t \left(a_{ik} \cos(\omega_{ik} t) + b_{ik} \sin(\omega_{ik} t) \right), \quad i \in [1,2], \tag{3.4}$$

where $\{\lambda, a_{ik}, b_{ik}, \omega_{ik}\}$ is a set of unknown parameters and n is an unknown number of basis functions. These basis functions were chosen empirically based on our swine datasets (see section 3.5). Thus, only a small number of basis functions should be needed to represent the FIRs, thereby resulting in a significant reduction in the parameters to be estimated. Then, for a fixed number of basis functions n, the set of parameters is estimated based on least squares minimization of e(t) in the following cross relation equation resulting from substitution of Equation (3.4) into Equation (3.1):

$$\begin{aligned} &\sum_{k=1}^{n} \left(a_{1k} \sum_{\tau=0}^{L_{opt}-1} \lambda^\tau \cos(\omega_{1k}\tau) p_{p2}(t-\tau) + b_{1k} \sum_{\tau=0}^{L_{opt}-1} \lambda^\tau \sin(\omega_{1k}\tau) p_{p2}(t-\tau) \right) \\ &- \sum_{k=1}^{n} \left(a_{2k} \sum_{\tau=0}^{L_{opt}-1} \lambda^\tau \cos(\omega_{2k}\tau) p_{p1}(t-\tau) + b_{2k} \sum_{\tau=0}^{L_{opt}-1} \lambda^\tau \sin(\omega_{2k}\tau) p_{p1}(t-\tau) \right) \\ &= e(t), \quad t \in [L_{opt}-1, N-1], \end{aligned} \tag{3.5}$$

where L_{opt} is established through eigenvalue analysis as described above with L_{max} = 15. To estimate the coefficient parameter sets $\{a_{ik}, b_{ik}\}$ uniquely (rather than to within an arbitrary scale factor), one FIR is constrained to have unity gain as follows:

$$\sum_{k=1}^{n} a_{1k} \sum_{t=0}^{L_{opt}-1} \lambda^t \cos(\omega_{1k} t) + \sum_{k=1}^{n} b_{1k} \sum_{t=0}^{L_{opt}-1} \lambda^t \sin(\omega_{1k} t) = 1. \tag{3.6}$$

The constraint here is well justified, as the paths from the aorta to the peripheral arteries offer very little resistance to blood flow due to Poiseuille's law (i.e., the mean values of pressure waveforms from different sites in the arterial tree are nearly the same) [Noordergraf 1978]. To simplify this constrained optimization problem, the damping parameter λ is set to $\exp(-3/L_{opt})$ so that the FIRs approximately decay to zero, while the frequencies in the parameter set ω_{ik} are allowed to take on only discrete values according to the Fourier Series (i.e., $2\pi l/L_{opt}$ for l=0,1,..., $\text{ceil}((L_{opt}-1)/2)$), where ceil(x) is the smallest integer $\geq$ x). For each set of frequency parameters $\{\omega_{ik}\}$ considered (see below), the corresponding coefficient parameter sets are estimated through the linear least squares solution. More specifically, similar to Equation (3.1), Equations (3.5) and (3.6) may be expressed in matrix form as follows:

$$\underbrace{\begin{bmatrix} P_2^1 & P_2^2 & -P_1^1 & -P_1^2 \end{bmatrix}}_{A} \underbrace{\begin{bmatrix} a_1 \\ b_1 \\ a_2 \\ b_2 \end{bmatrix}}_{x} = \underbrace{\begin{bmatrix} 0 \\ M \\ 0 \\ 1 \end{bmatrix}}_{b} + e, \tag{3.7}$$

where

$$P_i^j = \begin{bmatrix} P_{pi} \\ \varphi \end{bmatrix} \begin{bmatrix} \lambda^{L_{opt}-1} f\left((L_{opt}-1)*\omega_{i1}\right) & \cdots & \lambda^{L_{opt}-1} f\left((L_{opt}-1)*\omega_{in}\right) \\ \vdots & \ddots & \vdots \\ \lambda^0 f(0*\omega_{i1}) & \cdots & \lambda^0 f(0*\omega_{in}) \end{bmatrix},$$

$$f(x) = \begin{cases} \cos(x) & j=1 \\ \sin(x) & j=2 \end{cases};$$

$\mathbf{P_{pi}}$ is defined in Equation (3) with L = L_{opt}; $\boldsymbol{\varphi}$ is a $[1\times L_{opt}]$ vector whose elements are all zeros for i = 1 and all ones for i = 2; and $\mathbf{a_i} = \begin{bmatrix} a_{i1} & \cdots & a_{in} \end{bmatrix}^T$ and $\mathbf{b_i} = \begin{bmatrix} b_{i1} & \cdots & b_{in} \end{bmatrix}^T$, $i \in [1,2]$, are [n×1] vectors specifying the coefficient parameters of the two respective FIRs. Then, the least squares estimate of the vector **x** in Equation (7) is obtained as $\mathbf{x} = (\mathbf{A}^T\mathbf{A})^{-1}\mathbf{A}^T\mathbf{b}$. Amongst all of the linear least squares solutions computed for each considered set of frequency parameters $\{\omega_{ik}\}$, the one that minimizes the two-norm of the vector **e** in Equation (7) is selected so as to provide the optimal estimate of the parameter set $\{\lambda, a_{ik}, b_{ik}, \omega_{ik}\}$. Finally, the number of basis functions n is determined iteratively by starting with a single basis function representation and then adding one basis function at a time until the two-norm of the vector **e** becomes < 10% of the two-norm of the vector $(\mathbf{p_{p1}} + \mathbf{p_{p2}})/2$, where $\mathbf{p_{pi}}$ is defined in Equation (3.10). For further simplicity, in the k^{th} iteration, the frequency parameters are only estimated for the newly added basis function with the frequency parameters of the previous (k-1) basis functions set to the estimates obtained from the $(k-1)^{th}$ iteration. In the k^{th} iteration, the number of sets of frequency parameters considered is specifically $(\text{ceil}((L_{opt}-1)/2)) - k + 2)^2$. Thus, the two FIRs are assumed to be represented by the same number of basis functions but of generally different frequencies.

Next, with the set of basis function parameters $\{\lambda, a_{ik}, b_{ik}, \omega_{ik}\}$ estimated and the two FIRs fully defined through Equation (4), the common AP waveform input of the model of Figure (3.1) is estimated through multi-channel least squares deconvolution [Abed-

Meriam 1997]. That is, the two measured outputs may be expressed in terms of their common input via convolution as follows:

$$p_{pi}(t) = \sum_{k=0}^{L_{opt}-1} h_i(k)p_a(t-k) + n_i(t), \quad i \in [1,2], \quad t \in [0,N-1], \tag{3.8}$$

where $n_i(t)$ accounts for any noise. The common input is then estimated by least squares minimization of $n_i(t)$, $i \in [1,2]$ [Donald 1960, Noordergraf 1978]. More specifically, Equation (3.8) may also be expressed in matrix form by stacking each individual equation corresponding to each t and i, one on top of the other as follows:

$$\underbrace{\begin{bmatrix} p_{p1} \\ p_{p2} \end{bmatrix}}_{\mathbf{p_p}} = \underbrace{\begin{bmatrix} H_1 \\ H_2 \end{bmatrix}}_{\mathbf{H}} \mathbf{p_a} + \underbrace{\begin{bmatrix} n_1 \\ n_2 \end{bmatrix}}_{\mathbf{n}}, \tag{3.9}$$

where

$$\mathbf{p_{pi}} = [p_{pi}(0) \quad p_{pi}(1) \quad \cdots \quad p_{pi}(N-1)]^T, \quad i \in [1,2], \tag{3.10}$$

are [N×1] vectors of the respective measured output samples;

$$\mathbf{H_i} = \begin{bmatrix} h_i(L_{opt}-1) & \cdots & h_i(0) & \cdots & 0 \\ \vdots & \ddots & & \ddots & \vdots \\ 0 & \cdots & h_i(L_{opt}-1) & \cdots & h_i(0) \end{bmatrix}, \quad i \in [1,2],$$

are the [N×(N+L_{opt}-1)] Toeplitz matrices including the estimated parameters of the respective FIRs;

$$\mathbf{p_a} = [p_a(-L_{opt}-1) \quad p_a(-L_{opt}-2) \quad \cdots \quad p_a(0) \quad p_a(1) \quad \ldots \quad p_a(N-1)]^T$$

is a [(N+L_{opt}-1)×1] vector of the unknown common input samples; and

$$\mathbf{n_i} = \left[n_i(0) \quad n_i(1) \quad \cdots \quad n_i(N-1) \right]^T, \quad i \in [1,2],$$

are [Nx1] vectors of the respective noise samples. The least squares estimate of the vector $\mathbf{p_a}$ in Equation (3.9) is then obtained through the following linear least squares solution with Tikhonov regularization [Hansen 1987]:

$$\mathbf{p_a} = (\mathbf{H}^T\mathbf{H} + \mu\mathbf{I})^{-1}\mathbf{H}^T\mathbf{p_p}. \tag{3.11}$$

The matrix $(\mathbf{H}^T\mathbf{H} + \mu\mathbf{I})$ here is relatively large ((> 3000)×(> 3000)) for one-minute analysis intervals and a sampling frequency of 50 Hz), and standard computation of its inverse is therefore very expensive requiring $O(N^3)$ operations. However, by exploiting the Toeplitz structure of this matrix, its inverse is instead computed efficiently in $O(N \log N)$ operations using the fast circular decomposition method described in [Jain 1978]. The estimated AP waveform is then lowpass filtered with a cutoff frequency of 15 Hz in order to further attenuate any high frequency noise generated in the deconvolution process. This cutoff frequency is well justified, as the relevant waveform features generally fall within this frequency range [Chen 1997]. It should be noted that the estimated AP waveform will be slightly delayed (< 0.1 s) with respect to the actual AP waveform, because the time delay shared by the FIRs cannot be identified with MBSI.

Finally, beat-to-beat relative changes in CO are estimated from the determined AP waveform by employing the Windkessel model of Figure (3.2a), which accounts for the lumped arterial compliance (C_a) of the large arteries and the total peripheral resistance (R_a) of the small arteries, as described in [Bourgeois 1976]. That is, since C_a may be nearly constant over a wide pressure range and on the time scale of months [Bourgeois

1974, Hallock 1937, Zhenwei 2006], proportional CO for each cardiac cycle is calculated through the following governing model equation:

$$CO \propto \frac{1}{T}\left(p_a(t_{es}) - p_a(t_{bs}) + \frac{1}{\tau}\int_{t_{bs}}^{t_{es}} p_a(t)dt \right), \tag{3.12}$$

where $p_a(t)$ is again the estimated AP waveform, and t_{bs}, t_{es}, T, and $\tau = R_a C_a$ are timing parameters that are determined from this waveform as shown in Figure (3.2b). More specifically, t_{bs}, which denotes the beginning time of the SEI, is identified as the time of the local minimum that immediately precedes the time of peak SP for the cardiac cycle; t_{es}, which indicates the ending time of the SEI, is identified as the time of the minimum of the derivative of the estimated waveform over the interval from the time of peak SP to the t_{bs} of the next cardiac cycle; T, which signifies the cardiac cycle duration, is determined as the difference between the t_{bs} of successive cardiac cycles; and τ, which is the time constant of the Windkessel model, is estimated by least squares fitting of a single exponential decay to the reconstructed waveform over an interval between t_{es} and t_{bs} of the next cardiac cycle, in accordance with the model prediction. Since the time constants governing R_a changes are significantly longer than the cardiac cycle duration [Berger 1989], the τ estimates are actually averaged over five cardiac cycles to attenuate any noise.

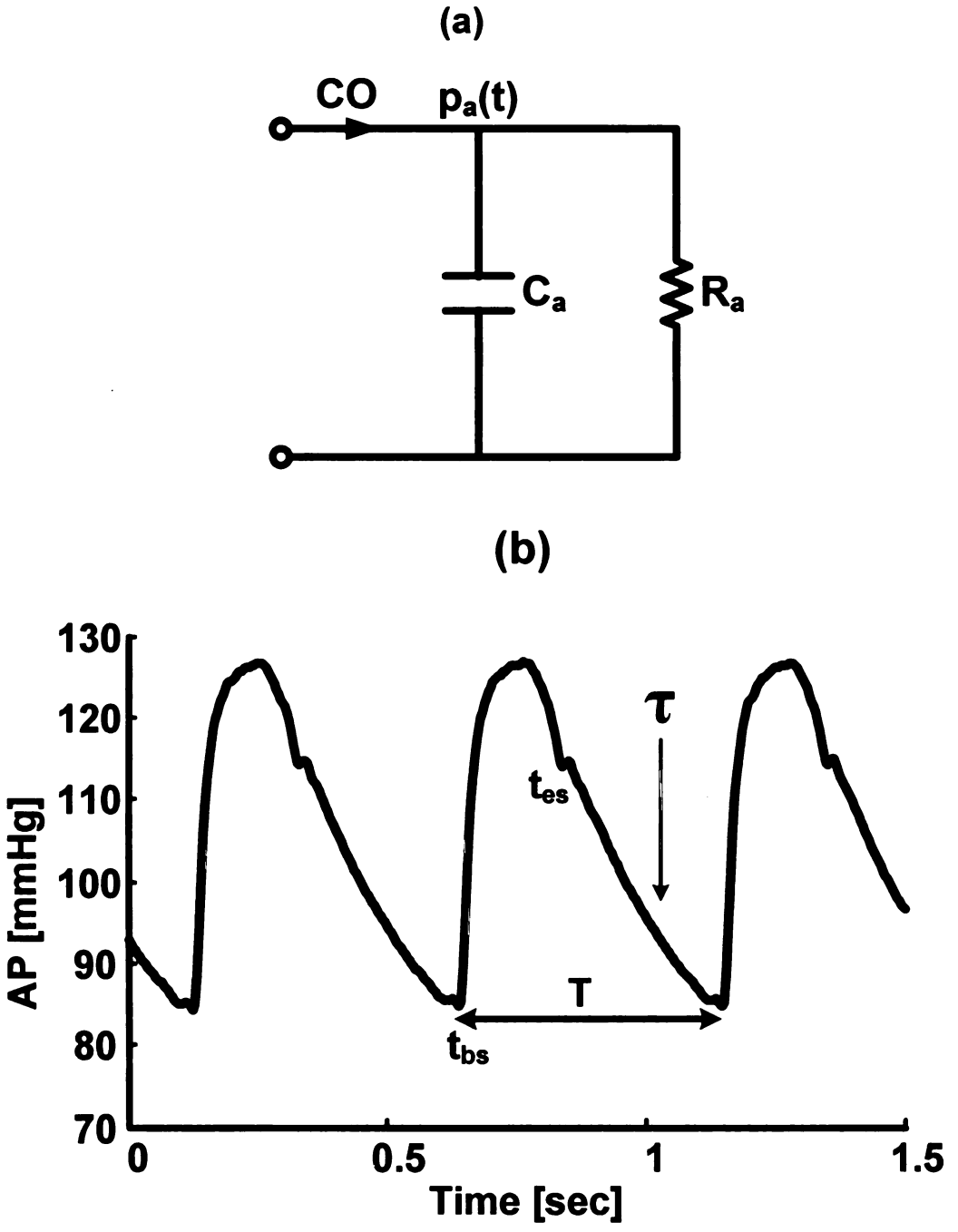

Figure 3.2 Lumped parameter Windkessel model providing the basis for the technique to estimate beat-to-beat relative changes in cardiac output (CO) from the estimated AP waveform ($p_a(t)$) in which the wave distortion should be greatly attenuated (see Figure (3.1)). (b) Illustration generally indicating how the unknown timing parameters in Equation (3.12), namely t_{bs} (beginning time of the systolic ejection interval (SEI)), t_{es} (ending time of the SEI), T (cardiac cycle duration), and $\tau = R_a C_a$ (time constant of the Windkessel model), are determined from the estimated AP waveform.

3.3 Methods

We evaluated the technique with respect to experimental datasets that were originally collected to address related but different specific aims [Mukkamala 2006] and previously utilized to investigate our initial MBSI technique for estimating the AP waveform using the standard eigenvector method [Swamy 2007]. Briefly, these datasets consist of various hemodynamic recordings obtained from four swine (30-34 kg) under general anesthesia and mechanical ventilation. The hemodynamic recordings include femoral artery pressure (FAP) and radial artery pressure (RAP) waveforms measured with fluid-filled catheters, a reference AP waveform measured from the descending thoracic aorta with a high frequency response micromanometer-tipped catheter, and gold standard reference beat-to-beat CO measured with an aortic flow probe. These hemodynamic recordings are available at a sampling frequency of 250 Hz for a total of 253 minutes during infusions of volume, phenylephrine, dobutamine, isoproterenol, esmolol, nitroglycerine, and progressive hemorrhage. Table (3.1) shows that these interventions imposed a wide hemodynamic parameter range for each of the four swine datasets.

We applied the technique to all one-minute, non-overlapping intervals of the FAP and RAP waveforms resampled to 50 Hz. We evaluated the resulting AP waveform estimates with respect to the measured reference waveforms (likewise resampled to 50 Hz) in terms of the root-mean-squared-error (RMSE) of the following parameters: total waveform (i.e., sample-to-sample), beat-to-beat SP, beat-to-beat PP, and beat-to-beat SEI. For comparison, we likewise evaluated the PAP waveforms (with respect to the measured AP waveforms) as well as the AP waveform estimates from our initial MBSI technique and an autoregressive exogenous input (ARX)-based generalized transfer function [Fetics,

1999] developed on a subset of the swine datasets as described in [Swamy 2007]. (Prior to conducting these evaluations, we advanced the AP waveform estimates and the PAP waveforms so that they were temporally aligned with the measured AP waveforms.) Since it is customary to report CO errors in percent, we evaluated the resulting beat-to-beat proportional CO estimates with respect to the reference aortic flow probe measurements in terms of the root-mean-squared-normalized-error (RMSNE). This quantity was specifically computed by 1) scaling the proportional CO estimates to have the same mean value as the reference CO in each animal; 2) normalizing each calibrated CO error with the reference CO value; and 3) computing the RMS of the normalized, calibrated CO errors. For comparison, we likewise evaluated the beat-to-beat proportional CO estimates obtained by fitting the Windkessel model directly to the FAP and RAP waveforms as well as to the AP waveforms estimated by our initial technique and the generalized transfer function.

Table 3.1 The new technique (see Figures (3.1) and (3.2)) as well as alternative peripheral artery pressure (PAP) waveform analysis techniques were evaluated with respect to four swine datasets consisting of simultaneous measurements of femoral artery pressure (FAP) and radial artery pressure (RAP) waveforms, a reference aortic pressure (AP) waveform, and reference aortic flow probe cardiac output (CO) during diverse interventions. MAP is mean arterial pressure; SP, systolic pressure from AP; PP, pulse pressure from AP; SEI, systolic ejection interval from AP; and HR, heart rate.

Hemodynamic Parameter	Animal				
	1	2	3	4	Total
MAP Range [mmHg]	54 – 136	58 – 117	45 – 114	48 – 119	45 – 136
SP Range [mmHg]	62 – 182	70 – 148	55 – 144	58 – 157	55 – 187
PP Range [mmHg]	17 – 54	17 – 52	20 – 62	19 – 57	17 – 62
SEI Range [ms]	160 – 400	160 – 340	120 – 240	140 – 300	120 – 400
HR Range [beats/min]	100 – 223	92 – 190	91 – 243	102 – 207	91 – 243
CO Range [L/min]	2.3 – 4.1	1.7 – 6.0	2.4 – 5.7	1.3 – 6.2	1.3 – 6.2

3.4 Results

Table (3.2) includes the evaluation results for the AP waveforms estimated by the technique introduced herein, which employs our new MBSI method, for each of the four swine datasets as well as the corresponding results for the measured PAP waveforms. The overall total waveform RMSE of the AP waveform estimates was 3.5 mmHg (after a modest time alignment), whereas the average overall total waveform RMSE between the PAP waveforms and the measured AP waveforms was 8.6 mmHg (after a more significant time alignment). Thus, the technique effectively reduced the wave distortion in the measured PAP waveforms by 59%. As a result, the technique also reduced the average overall SP and PP RMSEs by 71% and 61%, respectively. However, the technique did not improve upon the surprisingly small, overall SEI RMSE obtained from the FAP waveforms. Figure (3.3a) provides a visual example illustrating the significant differences between the PAP waveforms and the measured AP waveform, while Figure (3.3b) shows that the AP waveform estimated from these PAP waveforms closely agrees with the directly measured reference waveform.

Table (3.2) also provides a comparison of the evaluation results for the AP waveforms estimated by our new technique, our initial MBSI technique, which employs the standard eigenvector method, and a previous ARX-based generalized transfer function for each of the four swine datasets. The overall total waveform RMSE of the AP waveform estimates from our initial technique was 4.6 mmHg, while the average overall total waveform RMSE from the generalized transfer function was 5.4 mmHg. Thus, both MBSI techniques provided more accurate AP waveform estimates than the conventional generalized transfer function even though it was developed on a subset of

the swine datasets. However, the new technique enhanced the estimation accuracy of our initial technique by 24%. As a result, the new technique provided similar improvements in the estimation of SP and PP (but yielded similar results in the estimation of the SEI). In addition, a more significant advantage of the new technique over the initial technique is indicated below.

Table (3.3) includes the evaluation results for the beat-to-beat proportional CO estimated by the new technique via fitting the Windkessel model of Figure (3.2a) to the estimated AP waveform for each of the four swine datasets as well as the corresponding results obtained by directly fitting the model to each of the PAP waveforms. The overall beat-to-beat CO RMSNE from the AP waveform estimates was 12.9%, whereas the average overall beat-to-beat CO RMSNE from the PAP waveforms was 26%. Thus, the technique enhanced the beat-to-beat CO estimation accuracy by 50%. Interestingly, the overall beat-to-beat CO RMSNE from the FAP waveforms was 49% smaller than the corresponding RMSNE from the RAP waveforms but still 33% larger than the analogous RMSNE obtained with the technique. Figure (3.4) provides a visual illustration of the close agreement between the estimated and once calibrated beat-to-beat CO from the technique and the gold standard reference aortic flow probe measurements for each of the four swine datasets.

Table (3.3) also provides a comparison of the evaluation results for the beat-to-beat proportional CO estimated by the new technique and via fitting the Windkessel model to the AP waveform estimates from our initial technique and the generalized transfer function. The overall beat-to-beat CO RMSNE from the AP waveforms estimated by our initial technique was 36.3%, while the average overall beat-to-beat CO RMSNE from the

waveforms estimated by the generalized transfer function was 20.2%. Thus, the new technique increased the beat-to-beat CO estimation accuracy of the former technique by 63% and the latter technique by 36%. Note that the beat-to-beat CO RMSNE obtained with our initial technique was even larger than the corresponding RMSNEs from the PAP waveforms. As discussed in Section 3.5, this result was mainly due to outliers in the AP waveform estimation.

Table 3.2 Quantitative summary of the aortic pressure waveform estimation results in terms of root-mean-squared-error. The new technique resulted in more accurate AP waveform estimates in the four swine datasets (see Figure (3.3)) than those obtained from alternative PAP waveform analysis techniques including the conventional generalized transfer function (GTF). The root-mean-squared-errors are in units of mmHg for the total waveform (TW), SP, and PP parameters and ms for the SEI parameter.

Arterial Pressure Waveform	Arterial Pressure Parameter	Animal				
		1	2	3	4	Total
Estimated AP (New Technique)	TW	2.5	3.9	3.4	3.4	3.5
	SP	1.9	5.1	5.0	5.6	4.8
	PP	2.8	5.4	6.4	6.1	5.6
	SEI	22	14	21	22	19
FAP	TW	11.6	7.8	6.3	7.0	8.1
	SP	19.2	13.5	12.0	10.7	13.7
	PP	10.5	14.3	10.2	14.3	12.6
	SEI	22	19	19	20	19
RAP	TW	4.0	10.5	9.4	9.3	9.1
	SP	5.1	24.5	16.7	22.7	19.7
	PP	4.9	19.2	10.3	21.6	15.9
	SEI	20	38	18	48	33
Estimated AP (Initial Technique)	TW	4.4	4.4	3.8	5.7	4.6
	SP	4.1	5.0	5.0	9.4	6.1
	PP	4.3	5.9	7.1	9.9	7.1
	SEI	23	14	22	22	20
Estimated AP (GTF: FAP → AP)	TW	4.8	5.2	6.9	5.6	5.8
	SP	7.4	7.7	12.4	9.6	9.7
	PP	8.6	9.4	13.4	11.2	11.0
	SEI	24	28	46	42	35
Estimated AP (GTF: RAP → AP)	TW	4.2	4.6	6.0	5.1	5.0
	SP	5.3	6.6	8.7	6.5	7.1
	PP	4.8	6.3	8.5	6.8	7.0
	SEI	22	26	35	37	29

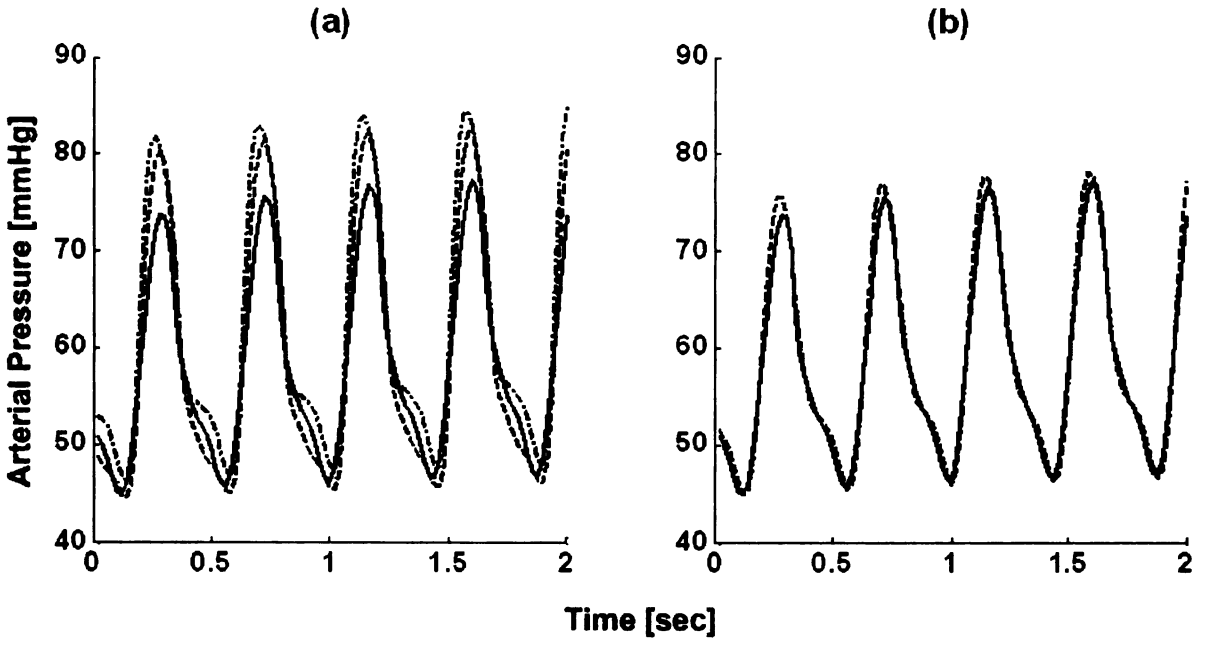

Figure 3.3 (a) Example segments of the measured AP (solid), femoral artery pressure (dash), and radial artery pressure (dot-dash) waveforms from one of the four swine datasets (see Table (3.1)). (b) Example segments of the AP waveform measured (solid) and estimated (dash) by applying the technique to the two segments of the PAP waveforms (see Figure (3.1)). See Table (3.2) for a complete quantitative summary of the AP waveform estimation results.

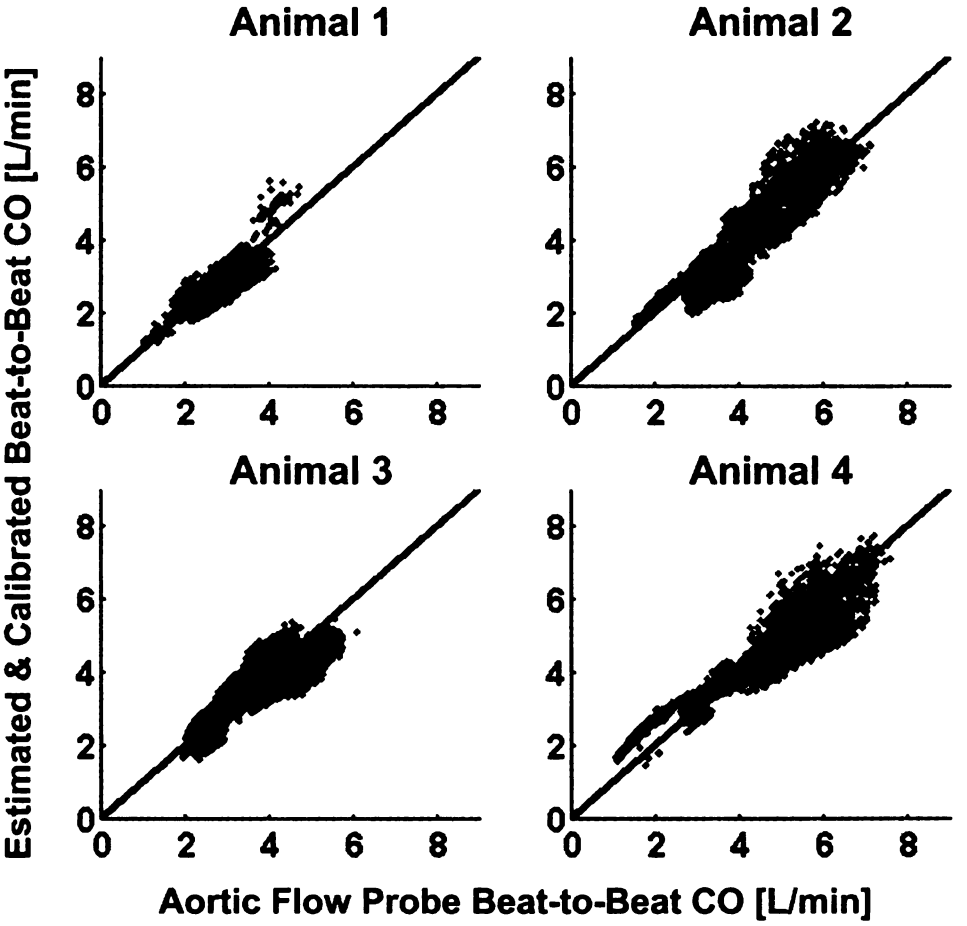

Figure 3.4 Beat-to-beat CO estimated (and once calibrated) by applying the technique to the estimated AP waveforms (see Figure (3.2)) plotted against the gold standard reference aortic flow probe CO measurements for each of the four swine datasets (see Table (3.1)). The solid line in each plot is the identity line. See Table (3.3) for a complete quantitative summary of the beat-to-beat proportional CO estimation results.

Table 3.3 Quantitative summary of the beat-to-beat proportional cardiac output estimation results in terms of root-mean-squared-normalized-error. The new technique (see Figure (3.2)) also resulted in more accurate beat-to-beat proportional CO estimates in the four swine datasets (see Figure (3.4)) than those obtained from alternative PAP waveform analysis techniques. The root-mean-squared-normalized-errors are in units of percent.

Arterial Pressure Waveform for Windkessel modeling	Animal				
	1	2	3	4	Total
Estimated AP (New Technique)	11.8	12.3	15.5	10.5	12.9
FAP	16.6	14.8	17.7	19.6	17.2
RAP	39.0	25.6	22.6	48.6	33.9
Estimated AP (Initial Technique)	44.7	37.8	28.0	37.1	36.3
Estimated AP (GTF: FAP $\rightarrow$ AP)	11.6	14.1	26.6	16.0	17.6
Estimated AP (GTF: RAP $\rightarrow$ AP)	20.0	25.0	19.9	26.0	22.8

3.5 Discussions

The present study represents a follow-up to our initial efforts in developing a patient and time specific technique for mathematically estimating the clinically more relevant AP waveform from less invasively measured PAP waveforms distorted by wave reflections [Swamy 2007]. In our initial study, we developed a technique to estimate the AP waveform from two or more PAP waveforms by employing MBSI rather than using the conventional generalized transfer function or any training data for that matter. In particular, the technique models the measured waveforms as individual outputs of coprime FIR channels driven by the common AP waveform input (see Figure (3.1)) and then analyzes the differences in the measured outputs, while invoking Poiseuille's law, so as to estimate the FIRs through the standard eigenvector method and ultimately reconstruct the common input via multi-channel least squares deconvolution. We applied the technique to FAP and RAP waveforms measured from four swine during diverse hemodynamic interventions, and our results showed superior agreement to simultaneously measured AP waveforms than a generalized transfer function developed on a subset of the swine data. The main contributions of the present study are in: 1) introducing a new MBSI method to more accurately estimate the FIRs and therefore the AP waveform; 2) proposing to estimate beat-to-beat proportional CO by fitting a lumped parameter Windkessel model to the estimated AP waveform in which the wave distortion should be greatly attenuated (see Figure (3.2)); and 3) testing the resulting new technique for estimating both the AP waveform and beat-to-beat relative changes in CO, while comparing it to several alternative techniques, based on our four previous swine datasets,

which also included gold standard reference aortic flow probe CO measurements (see Table (3.1)).

The basic idea of our new MBSI method is to represent the FIRs with more efficient basis functions than the standard impulse basis functions assumed by the eigenvector method. In this way, the number of parameters to be estimated will be reduced thereby potentially resulting in a marked decrease in the precision component of the FIR estimation error. We specifically chose damped sinusoidal basis functions to compactly represent the FIRs (see Equation (3.4)). This choice was made empirically by observing that the estimated impulse responses relating the *measured* AP waveforms to each of the PAP waveforms in one of the swine datasets generally appeared as damped sinusoids. Thus, the bias component of the FIR estimation error may only increase modestly with this choice of basis functions. For simplicity, we assumed that 1) the damping could be represented with a single parameter whose values was set according to the estimated channel order; 2) the frequencies of the sinusoids could take on only discrete values according to the Fourier Series; and 3) each of the FIRs could be represented with the same number of basis functions. Even with these simplifications, the complexity in the least squares estimation of the parameters of the basis functions increases considerably with the number of basis functions. Thus, to render a real-time technique (with a one minute delay), the parameter estimation was designed to only be optimal for a single basis function representation and sub-optimal for a multiple basis function representation. We acknowledge that an orthogonal basis set could permit both optimal and practical parameter estimation. However, it turned out that only one basis function was needed to represent the FIRs in about three-quarters of the one-minute intervals in the swine

datasets. As a result, only six parameters were generally estimated by the new method, whereas ten parameters were, on average, estimated by the standard eigenvector method. In addition to reducing the number of parameters to be estimated, the new method is also advantageous in terms of accommodating larger channel orders (by simply redefining the definition of an insignificant eigenvalue), which are more congruent with the estimated impulse responses mentioned above. Such channel orders would result in large estimation errors with the eigenvector method due to the limited frequency content of the AP waveform.

Our new technique was able to reliably estimate the AP waveform from the FAP and RAP waveforms in the four swine datasets with an overall total waveform RMSE of 3.5 mmHg (see Table (3.2) and Figure (3.3)). This error effectively represents a 59% reduction in wave distortion in the measured PAP waveforms. As a result, the technique was able to similarly reduce the RMSEs of SP and PP, which are perhaps the two most clinically significant parameters of the AP waveform. Significantly, the aforementioned overall total AP waveform RMSE represents a 24% improvement with respect to our initial technique and a 35% improvement with respect to a generalized transfer function developed on a subset of the swine datasets. The former improvement is likely due to a reduction in the FIR estimation error variance, while the latter improvement is presumably a result of accounting for the changes in arterial tree properties induced by the interventions as well as any inter-subject variability.

As a result of greatly attenuating the wave distortion, our new technique was also able to reliably estimate beat-to-beat relative changes in CO in the four swine datasets with an overall RMSNE of 12.9% (see Table (3.3) and Figure (3.4)). This result is consistent

with a compelling, previous study in which beat-to-beat proportional stroke volume was shown to be impressively estimated over a wide hemodynamic range by simply fitting the Windkessel model to the AP waveform (measured specifically from the descending thoracic aorta) [Bourgeois, 1976]. Significantly, the aforementioned overall beat-to-beat CO RMSNE of our new technique represents an improvement of $\geq 25\%$ with respect to fitting the Windkessel model directly to each of the PAP waveforms and to the AP waveforms estimated by our initial technique and the generalized transfer function. Counter to intuition, the beat-to-beat proportional CO estimates obtained from the AP waveforms estimated by our initial technique were the least accurate. As mentioned above, this result is mainly due to outliers in the AP waveform estimation. These outliers may have been caused by an insufficient number of frequency components in the AP waveform and have essentially been eliminated by the new technique, which required fewer parameters for estimation.

As an interesting aside, the beat-to-beat CO RMSNE obtained by direct fitting of the Windkessel model to the FAP waveforms is nearly half that obtained by direct model fitting to the RAP waveforms (see Table (3.3)). This result may be due to the surprisingly accurate SEI estimates obtained from the FAP waveforms (see Table (3.2)) and their relatively consistent morphology throughout the interventions. It is unclear whether these features hold in human FAP waveforms. On the other hand, the beat-to-beat CO RMSNE obtained from the RAP waveforms was reduced by nearly a third after the generalized transfer function was applied to these waveforms (see Table (3.3)). To our knowledge, this result of the generalized transfer function has not been shown before. However, application of the generalized transfer function to the FAP waveforms did not

further reduce the already relatively low beat-to-beat CO RMSNE (see Table (3.3)) perhaps because the AP waveform estimates here were not as accurate (see Table (3.2)).

Our new technique (as well as our initial technique) was inspired by the recent efforts of McCombie et al. who we believe were the first to apply MBSI in the field of hemodynamic monitoring [McCombie 2005]. These investigators specifically proposed a technique to estimate the morphology of the common aortic flow waveform input from multiple PAP waveform outputs and showed its feasibility in a single swine. Figure (3.5) illustrates the single input, multi-output model upon which their technique was based. As can be seen from this model, the channels coupling the aortic flow waveform to each PAP waveform include common dynamics, namely the channel relating the aortic flow waveform to the AP waveform, and are therefore not coprime. As a result, these investigators had to develop additional signal processing to estimate the common channel, which resulted in a considerably more complicated technique than standard MBSI. Moreover, since their technique does not provide the scale factor of the estimated input, it cannot be utilized to monitor relative changes in CO. In contrast, our new technique first estimates the AP waveform input in which the coprime channel assumption is more tenable and the arbitrary input scale factor is conveniently determined through Poiseuille's law and then estimates beat-to-beat relative changes in CO by fitting the Windkessel model to the estimated waveform in which the wave distortion is greatly attenuated. We note that it is also possible to estimate the aortic flow waveform by applying the governing Windkessel model differential equation to the AP waveform estimated by our technique. However, the aortic flow waveform estimated in this manner

did not closely agree with the reference aortic flow probe waveform in our swine datasets perhaps due to noise arising from implementing the required derivative operation.

Our new technique is related to a previous technique that we have developed for automated and less invasive monitoring of average relative changes in CO by long time interval analysis of a single PAP waveform [Zhenwei 2006]. The basic idea of this technique is to *circumvent* the highly complex wave reflections by effectively applying the Windkessel model to the waveform variations occurring over time scales greater than a cardiac cycle in which the distributed arterial tree appears to be lumped [Noordergraf 1978]. In contrast, the technique introduced herein aims to essentially *remove* the wave reflections through MBSI and then apply the Windkessel model. The advantage of this technique is in providing AP waveform estimates as well as beat-to-beat rather than average proportional CO estimates. The obvious disadvantage is in requiring more than one waveform for analysis. (Note that the CO RMSNE that we reported earlier for our previous technique in [Zhenwei 2006] is not directly comparable to the results of this study, as the swine evaluation data utilized herein represent only a subset of the data employed in our earlier study.)

The new technique introduced herein permits both automated and less invasive central hemodynamic monitoring through estimation of the AP waveform and beat-to-beat relative changes in CO by mathematical analysis of multiple PAP waveforms. In addition, the technique may possibly prove useful for local hemodynamic monitoring at each PAP waveform measurement site through the corresponding estimated FIR. The technique could potentially be applied to non-invasive PAP waveforms measured from patients with various cardiovascular diseases (e.g., hypertension, heart failure, shock) in a

number of different settings (e.g., emergency rooms, intensive care units, homes) as well as to invasive PAP waveforms obtained from critically ill patients. While only one PAP catheter is commonly used in the latter patients, a subset of these patients is also instrumented with the more risky pulmonary artery catheter for operator-required measurements of average CO via the standard thermodilution method [Marino 1998]. For this patient population in particular, the technique as applied to two invasive PAP waveforms (e.g., measured from the routinely cannulated femoral and radial arteries [Marino 1998]) may be preferred. Future investigations of the technique with respect to invasive and non-invasive PAP waveforms measured from humans are needed to eventually realize these potential applications.

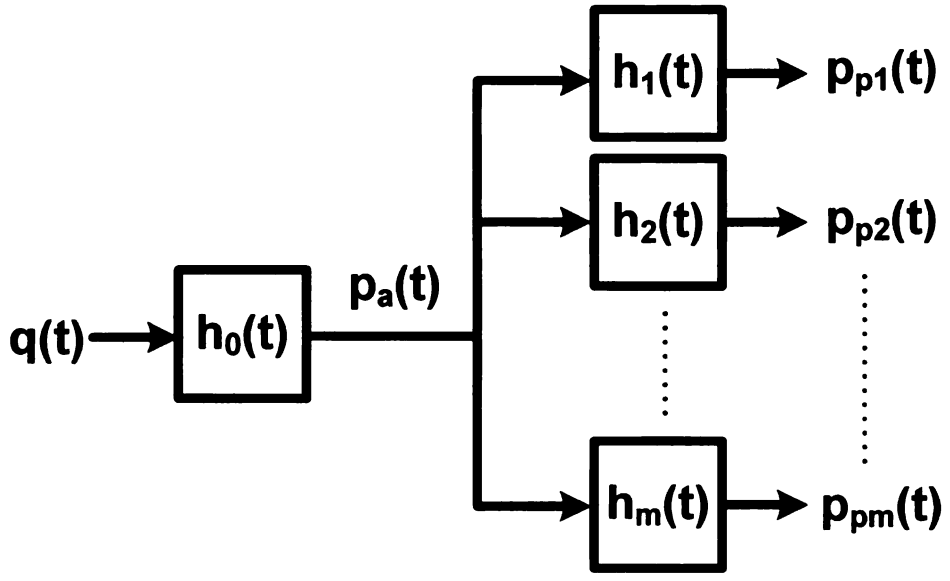

Figure 3.5 Single input, multi-output model of the arterial tree providing the basis for a previous MBSI technique to estimate the shape of the aortic flow waveform from multiple PAP waveforms. In contrast to the model of Figure (3.1), the common input to be estimated is the aortic flow waveform (q(t)). However, the channels coupling the aortic flow waveform input to the PAP waveform outputs are not coprime, as they share the channel relating the aortic flow waveform to the AP waveform. Since common channel dynamics cannot be estimated with MBSI methods [Xu 1995], the previous technique required additional complicated signal processing. In addition, this technique did not provide the scale factor of the aortic flow waveform and therefore cannot be utilized to monitor relative changes in CO.

CHAPTER 4

CONTINUOUS LEFT VENTRICULAR EJECTION FRACTION MONITORING BY AORTIC PRESSURE WAVEFORM ANALYSIS

4.1 Introduction

Left ventricular ejection fraction (EF) – the ratio of the stroke volume (SV) to the end-diastolic volume (EDV) of the left ventricle – is widely recognized as one of the most clinically significant indices of cardiac function. This recognition is largely due to its ability to predict mortality in patients with heart failure and coronary artery disease (see, e.g., [Bosch 2005, Curtis 2003] and references therein) as well as to readily distinguish between systolic and diastolic dysfunction [Katz 1992]. Serial changes in EF at rest and transient rate of changes in EF during exercise may offer additional prognostic value [Cintron 1993, Sridhara 1993].

The standard clinical method for measuring EF is through imaging the left ventricular volume via echocardiography, radionuclide techniques, contrast angiography, ultra-fast computed tomography, or magnetic resonance imaging [Rumberger 1997]. Each of these imaging methods offers certain advantages over the others in terms of, for example, level of accuracy, invasiveness, and radiation exposure. However, they generally share the major disadvantages of requiring a trained operator to make each individual measurement and expensive capital equipment. While sonomicrometry, the conductance catheter, and the non-imaging nuclear monitor are currently available for automated and continuous monitoring of left ventricular volume [Burkhoff 1990, Dellegrottaglie 2002, Rushmer 1956] these alternative methods suffer from significant practical disadvantages (e.g., high

level of invasiveness) that have prevented them from supplanting or even complementing imaging methods in clinical practice.

Thus, there is a need for a practical method capable of automated and continuous EF monitoring. Indeed, this need may be regarded as urgent due to the rapidly growing population with chronic heart disease [Ansari 2001] together with the projected shortage of clinical staff.

Based on our previous work in the field of hemodynamic monitoring [Lu 2006, Mukkamala 2006, Swamy 2007, Swamy 2008] our hypothesis is that EF may be accurately estimated by deciphering the information embedded in the temporal variations of blood pressure waveforms. In this way, EF may be continuously monitored in various inpatient settings with routinely employed invasive catheter systems [Marino 1998] as well as automatically measured in outpatient clinics and at home with commercial non-invasive transducers (see, e.g., the Finometer and Portapres, Finapres Medical Systems, The Netherlands and the T-Line Blood Pressure Monitoring System, Tensys Medical, San Diego, CA). As an initial step towards this ultimate end point, in this study, we specifically developed a technique to continuously estimate beat-to-beat EF as well as relative changes in beat-to-beat EDV and other important hemodynamic variables by model-based analysis of the aortic pressure waveform. We then performed experiments in six dogs in order to evaluate the technique with respect to intermittent reference EF and EDV measurements via standard trans-thoracic two-dimensional echocardiography during various pharmacological and volume interventions. Our results demonstrate, perhaps for the first time, the feasibility of estimating EF from only blood pressure. Preliminary versions of this work have been reported [Mukkamala 2006, Swamy 2007].

4.2 Model Based Analysis Technique

Our model-based analysis technique is generally implemented in three steps. First, the aortic pressure waveform is represented with a circulatory model. Second, the model is fitted to each beat of the waveform so as to estimate its parameters to within a constant scale factor. Third, the proportional parameter estimates are utilized to compute beat-to-beat absolute EF by cancellation of the scale factor as well as monitor other beat-to-beat proportional hemodynamic variables. We describe the details of these steps below while stating the underlying assumptions and justify the major assumptions in the Discussion section.

First, the measured and sampled aortic pressure waveform is assumed to be well represented with the lumped parameter model of the left ventricle (lv), aortic valve, and arteries (a) shown in Fig. 1a in electrical analog form. Here, voltage is analogous to pressure (P), charge, to volume (V), and current, to flow rate. In particular, the left ventricle is represented with the variable capacitance or compliance (C) model whose elastance (E = 1/C) oscillates over time (t) so as to drive the flow of blood [Sagawa 1977, Suga 1974]. The aortic valve is modeled by an ideal diode (i.e., $P_{lv}(t) = P_a(t)$) during the systolic ejection interval wherein the valve is opened) thereby making aortic stenosis a contraindication of the technique. The arteries are represented with a two-parameter Windkessel model accounting for the compliance of the large arteries and the resistance (R) of the small arteries [Noordergraaf 1978]. In addition to compliance, the left ventricle (and large arteries) is parameterized with a zero-pressure (0) filling volume (i.e., unstressed volume). Finally, C_a is assumed to be constant over a monitoring period

(e.g., days to weeks), whereas the remaining parameters are assumed to be constant only over each cardiac cycle.

Thus, the pressure-volume relationship of the left ventricle model and the differential equation governing the entire model during the systolic ejection interval are given as follows:

$$V_{lv}(t) = \frac{P_a(t)}{E_{lv}(t)} + V_{lv}^0, \qquad t_{bs} < t \le t_{es}, \tag{4.1}$$

$$-\frac{d}{dt}\frac{P_a(t)}{E_{lv}(t)} = C_a \frac{d}{dt}P_a(t) + \frac{P_a(t)}{R_a}, \qquad t_{bs} < t \le t_{es}, \tag{4.2}$$

where the term $P_a(t)/E_{lv}(t)$ is the stressed left ventricular volume during the systolic ejection interval, and the subscripts bs and es respectively stand for the beginning and end of the systolic ejection interval. Integrating Equation (4.2) from t_{bs} to some time t within the systolic ejection interval, while dividing by the constant scale factor C_a, yields the following equation:

$$\frac{P_a(t_{bs})}{C_a E_{lv}(t_{bs})} - \frac{P_a(t)}{C_a E_{lv}(t)} = P_a(t) - P_a(t_{bs}) + \frac{1}{\tau}\int_{t_{bs}}^{t} P_a(\lambda)d\lambda, \qquad t_{bs} < t \le t_{es}, \tag{4.3}$$

where $\tau = R_a C_a$ is the Windkessel time constant. Note that the left-hand side of this equation is proportional to the volume of blood that has been ejected by the left ventricle by time t in the systolic ejection interval, while the right-hand side is proportional to the volume of blood that has entered the arteries by this time. Thus, when $t = t_{es}$, both sides of the equation indicate proportional SV or SV/C_a. Further note that the term $P_a(t)/C_a E_{lv}(t)$ here is proportional to the stressed volume that is remaining in the left

ventricle at time t in the systolic ejection interval. Thus, the terms $P_a(t_{bs})/C_aE_{lv}(t_{bs})$ and $P_a(t_{es})/C_aE_{lv}(t_{es})$ respectively represent proportional stressed left ventricular volume at the beginning time of the systolic ejection interval wherein ejection has yet to commence (i.e., proportional stressed EDV or stressed EDV/C_a) and at the end time of the systolic ejection interval wherein ejection has ceased (i.e., proportional stressed left ventricular end-systolic volume (ESV) or stressed ESV/C_a).

Second, to fit the model to the samples of the aortic pressure waveform so as to estimate its parameters, Equation (4.3) is discretized by replacing t with nT, where T is the sampling period and n denotes discrete-time, and approximating the integral via the trapezoidal formula as follows:

$$\frac{P_a(n_{bs}T)}{C_aE_{lv}(n_{bs}T)} - \frac{P_a(nT)}{C_aE_{lv}(nT)} = P_a(nT) - P_a(n_{bs}T) + \frac{T}{2\tau}\sum_{k=n_{bs}+1}^{n}(P_a(kT)+P_a((k-1)T)), \qquad n_{bs} < n \le n_{es}. \tag{4.4}$$

Here, T and $P_a(nT)$ for $n_{bs} \le n \le n_{es}$ (i.e., aortic pressure samples within the systolic ejection interval) are known, while τ (i.e., proportional total peripheral resistance) and $C_aE_{lv}(nT)$ for $n_{bs} \le n \le n_{es}$ (i.e., proportional left ventricular elastance samples within the systolic ejection interval) are unknown. It is evident that Equation (4.4) does not provide a basis for uniquely determining these unknown proportional model parameters and thus the proportional stressed left ventricular volume terms, as it represents an underdetermined set of equations with $n_{es} - n_{bs}$ equations and $n_{es} - n_{bs} + 2$ unknowns (where $n_{es} - n_{bs} \approx 80$ for T = 4 msec).

To arrive at a solvable (i.e., overdetermined) set of equations, a parametric function is assumed to succinctly characterize the temporal evolution of $E_{lv}(t)$over each cardiac cycle. In particular, the following, previously proposed parametric raised cosine function is employed:

$$E_{lv}(t)=\begin{cases} E_{min}+\dfrac{E_{max}-E_{min}}{2}\left\{1-\cos\left(\dfrac{\pi(t-t_{bi})}{T_s}\right)\right\}, & t_{bi}\le t<t_{bi}+T_s \\ E_{min}+\dfrac{E_{max}-E_{min}}{2}\left\{1+\cos\left(\dfrac{2\pi t(t-(t_{bi}+T_s))}{T_s}\right)\right\}, & t_{bi}+T_s\le t<t_{bi}+1.5T_s \\ E_{min}, \quad t_{bi}+1.5T_s\le t & \end{cases} \tag{4.5}$$

where E_{min} and E_{max} respectively represent the minimum and maximum ventricular elastances over a cardiac cycle; T_s indicates the time duration to reach E_{max} from E_{max}; and the subscript bi stands for the beginning of the isovolumic contraction phase (see solid line in lower panel of Figure (4.1b)) [Heldt, 2002]. Substitution of Equation (4.5) into Equation (4.4) reduces the number of unknowns to five, namely τ, C_aE_{max}, C_aE_{min}, T_s, and $C_aE_{lv}(n_{bs}T)$ (i.e., proportional left ventricular elastance at the beginning time of the systolic ejection interval). Further, C_aE_{min} is assumed to be equal to $0.05\cdot C_aE_{max}$ so as to reduce the number of unknowns to four (see gray font in Figure (4.1b)). The four unknowns are then estimated for each beat in two steps.

In the initial step, τ is estimated from the diastolic interval of the aortic pressure waveform (i.e., from the time of the minimum of the first difference of the waveform between the time of the peak systolic pressure and the time of the local minimum immediately preceding the subsequent peak systolic pressure (defined as $n_{es}T$ of the

beat) to this latter time (defined as $n_{bs}T$ of the next beat)). In particular, since the lumped parameter model predicts that aortic pressure should decay like a pure exponential during the diastolic interval, τ is estimated by least squares fitting of an exponential to this interval (see Figure (4.1b)). Optimal fitting is achieved in closed-form after log transformation of aortic pressure. Since the time constants governing R_a changes are significantly longer than the cardiac cycle duration [Berger 1989], the τ estimates are then averaged over ten successive cardiac cycles to attenuate any noise.

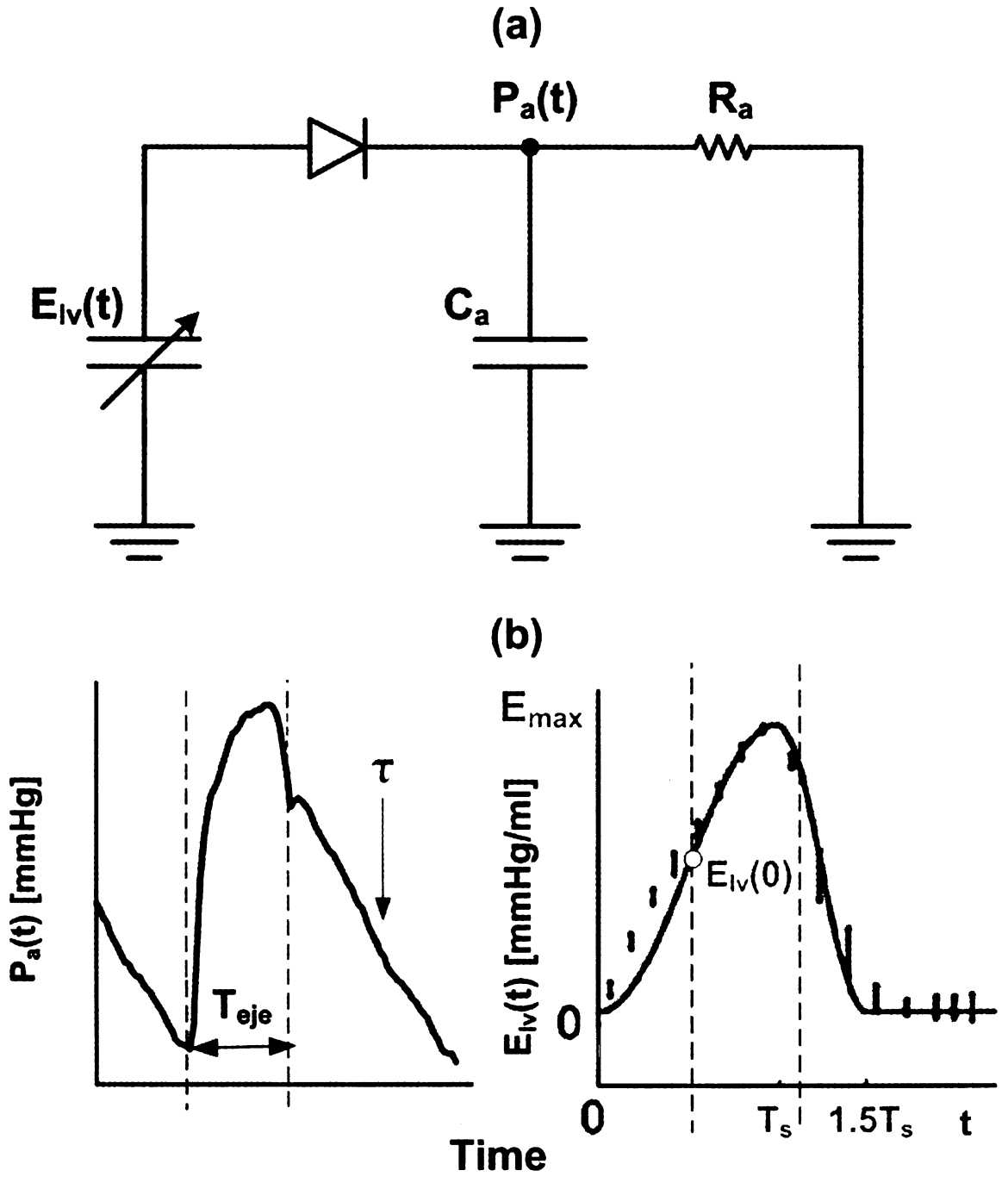

Figure 4.1 Model-based analysis technique for monitoring EF. (a) Lumped parameter model of the left ventricle and arteries upon which the technique is based. (b) $E_{lv}(t)$ in the model is assumed to vary over time according to a parametric raised cosine function (solid line in the lower panel).

In the subsequent step, the estimated τ is substituted into Equation (4.4), and the remaining unknowns in this equation, $C_a E_{max}$, T_s, and $C_a E_{lv}(n_{bs}T)$, are estimated by least squares fitting of the equation to the systolic ejection interval of the aortic pressure waveform (i.e., the remainder of the beat). Optimal fitting is achieved by numerical search over the following physiologic range of the three unknowns: 1) 0 (physical minimum value) < $C_a E_{max} \leq 15$ (3 times the nominal value reported in the literature [20], [24], [25], [26]; 2) $\frac{1}{3}QT \leq T_s \leq \frac{4}{3}QT$, where the QT interval is obtained from a simultaneous ECG measurement (with the underlying assumption that the electrical QT interval is a rough approximation of the mechanical time interval between the start of the upstroke to the end of the downstroke of $E_{lv}(t)$; and 3) $C_a E_{lv}(t_{bi} + T_s - T_{eje}) \leq C_a E_{lv}(n_{bs}T) \leq C_a E_{lv}(t_{bi} + T_s)$, where T_{eje} is the duration of the systolic ejection interval (to ensure that the end time of the systolic ejection interval does not occur prior to the time of E_{max}). With the estimated $C_a E_{max}$, T_s, and $C_a E_{lv}(n_{bs}T)$, $C_a E_{lv}(nT)$ is computed for $n_{bs} \leq n \leq n_{es}$ through Equation (4.5).

Third, beat-to-beat absolute EF is computed from the resulting $C_a E_{lv}(nT)$ for $n_{bs} \leq n \leq n_{es}$ and the measured P(t) by cancellation of the C_a scale factor as follows:

$$EF = \frac{\frac{SV}{C_a}}{\frac{EDV}{C_a}} = \frac{\frac{P_a(n_{bs}T)}{C_a E_{lv}(n_{bs}T)} - \frac{P_a(n_{es}T)}{C_a E_{lv}(n_{es}T)}}{\frac{P_a(n_{bs}T)}{C_a E_{lv}(n_{bs}T)} + \frac{V_{lv}^0}{C_a}}, \tag{4.6}$$

where V_{lv}^0 / C_a (i.e., proportional unstressed left ventricular volume), in contrast to the other terms in the right-hand side of this equation, is neither estimated nor measured but

rather assumed to take on a nominal value (see below). Note that the term $P_a(n_{es}T)/C_aE_{lv}(n_{es}T)$ (i.e., proportional stressed ESV) should correspond to the minimum value of $P_a(nT)/C_aE_{lv}(nT)$ over $n_{bs} \le n \le n_{es}$ (i.e., proportional stressed left ventricular volume samples within the systolic ejection interval). However, such correspondence may not always hold due to imperfect identification of the end time of the systolic ejection interval (or, equivalently, the beginning time of the diastolic interval). In these instances, $P_a(n_{es}T)/C_aE_{lv}(n_{es}T)$ in Equation (4.6) is replaced with the minimum value of $P_a(nT)/C_aE_{lv}(nT)$ over $n_{bs} \le n \le n_{es}$.

Note that by-products of the above three steps are beat-to-beat proportional estimates of EDV, SV, cardiac output (CO = HR·SV, where HR is heart rate), R_a, and E_{max} (which is known to be a relatively specific index of ventricular contractility [Sagawa 1977, Suga 1974]. Thus, relative changes in these important hemodynamic variables may be monitored as well.

4.3 Materials and Methods

Experimental Procedures

To evaluate the model-based analysis technique, experiments were performed in six normal adult beagles (10-15 kg). All experimental procedures were reviewed and approved by the MSU All-University Committee on Animal Use and Care.

In one dog, a sterile surgical procedure was employed for implanting chronic recording transducers as follows. General anesthesia was induced with an intravenous injection of propofol (2.2 – 6.6 mg/kg) and maintained with inhaled isoflorane (1.5 – 2.5%), and mechanical ventilation was instituted. A left lateral thorocotomy was

performed. An ultrasonic flow probe was placed around the ascending aorta for gold standard reference SV and CO (Transonic Systems, Ithaca, NY), while a tygon catheter was placed in the left atrial appendage for unrelated purposes. The chest was evacuated and closed in layers, with the cable and catheter tunneled subcutaneously and exteriorized between the scapulae. The dog was then allowed ten days for recovery.

The chronically instrumented dog and the remaining five dogs were then studied as follows. General anesthesia was induced and maintained as described above but mechanical ventilation was not employed. A micromanometer-tipped catheter was inserted into a femoral artery and positioned under fluoroscopic guidance in the descending thoracic aorta (see below) for the aortic pressure waveform (Millar Instruments, Houston, TX). A similar catheter was also placed in the opposite femoral artery of half the dogs for future studies. A catheter was inserted into a cephalic vein for drug and isotonic fluid administration, and surface electrodes were placed for two frontal ECG leads. All of the analog transducer outputs were interfaced to a personal computer through an A/D conversion system (DataQ Instruments, Akron, OH). The cardiovascular measurements were then recorded in each dog at a sampling rate of 400-1000 Hz over the course of 50-170 minutes during a subset of the following interventions to alter EF and other hemodynamic variables: infusions of dobutamine, esmolol, verapamil, phenylephrine, nitroprusside, and volume as well as progressive hemorrhage. Various infusion rates were employed followed by brief recovery periods. During the recording session, trans-thoracic two-dimensional echocardiography (GE Vivid 7, Horton, Norway) was intermittently used for four-chamber left apical imaging in order to calculate reference EF and EDV. (This single plane method was shown to be nearly equivalent to

a biplane method in terms of measuring absolute EF and relative changes in EDV and ESV [Sutton, 1998].) A 5-10 beat cine echocardiographic recording at > 90 frames/sec was obtained at a time for the chronically instrumented dog, whereas 5-10 beat cine echocardiographic recordings at the same frame rate were obtained in triplicate for the five acutely studied dogs.

Data Analysis

The model-based analysis technique was applied off-line to the aortic pressure waveforms resampled to 250 Hz with the QT interval automatically detected from the surface ECGs using a previously introduced wavelet-based method [Maetinez 2004] and V_{lv}^0 / C_a set to the nominal canine value of 15 mmHg as prescribed in [Suga 1974, Bourgeois 1976]. The resulting beat-to-beat EF and proportional EDV and E_{max} estimates were then averaged over multiple beats for evaluation against the reference measurements and known drug effects (see below).

Reference EDV and ESV, and thus EF, were established by manually tracing the endocardial border of the single plane images, excluding papillary muscles, at end-diastole and end-systole and then applying Simpson's rule [Schiller 1991]. This method was performed for two beats of each cine echocardiographic recording, and the resulting values were then averaged over the two beats. For the five acutely studied dogs, the values were further averaged over each set of triplicate cine echocardiographic recordings. Thus, in these dogs, the reference EF and EDV represent six beat averages. For the chronically instrumented dog, the reference echocardiographic values were validated in part by noting a tight correspondence between the echocardiographic SV and the gold standard aortic flow probe SV ($\rho = 0.92$).

To compare the average proportional EDV estimates with the corresponding absolute reference values, the estimates were first scaled to have the same mean as the reference values in each dog. The average EF and average calibrated EDV estimates were then evaluated against their corresponding reference values through 1) standard Bland-Altman analysis for a comprehensive illustration of the estimation errors as a function of the reference values (rather than the average of the estimated and reference values) and an indication of the bias μ and precision σ of the estimation errors [Bland 1986] and 2) the root-mean-square of the estimation errors ($\mathrm{RMSE} = \sqrt{\mu^2 + \sigma^2}$) for a simple scalar metric indicating the overall error size. For the chronically instrumented dog, the resulting beat-to-beat proportional CO estimates were likewise calibrated and then compared to the corresponding absolute reference aortic flow probe values through the RMSNE (i.e., RMS of the estimation errors normalized (N) by the reference values), as CO errors are customarily reported in percent [Crtichley 1999]. Finally, the average proportional E_{max} estimates were qualitatively evaluated in terms of whether they changed in the physiologically expected manner in response to the positive inotrope dobutamine and the negative inotrope esmolol. (Note that verapamil acted more like a vasodilator in our study.)

4.4 Results

Figure (4.2) illustrates exemplary segments of the aortic pressure waveform measured from one of the dogs during baseline, dobutamine, and volume infusion conditions. Note that the aortic pressure waveform consistently exhibited a smooth upstroke during the systolic ejection interval and an exponential decay during the diastolic interval despite

large variations in EF and mean aortic pressure (MAP). This result generally held for the entirety of the waveform as well as for the waveforms of the remaining five dogs. Thus, the lumped parameter model of Figure (4.1a), which accounts for smooth dynamics, was representative of the measured aortic pressure waveforms.

The Table and Figure (4.3) summarize the results of applying the model-based analysis technique to the measured aortic pressure waveforms. In particular, the Table includes the hemodynamic range and average EF and calibrated EDV RMSEs for each dog, while Figure (4.3) illustrates Bland-Altman plots of all of the average EF and calibrated EDV errors for the six dogs. As can be seen, the employed interventions imposed a wide spectrum of hemodynamic conditions but did not result in a state of severe systolic dysfunction. The average EF RMSE was 5.6% over all the dogs and was generally consistent in each dog, deviating most in dog 1 with a value of 8.5%. Further, the average EF RMSE showed only a small bias component of ~1%. While the average EF errors did show a negative correlation with the corresponding reference echocardiographic EF values (ρ = -0.61), removal of the few large errors in the very high reference EF range (> ~80%; see below) substantially reduced this correlation. The average calibrated EDV RMSE was 4.1 ml over all the dogs and was likewise generally consistent in each dog, except for dog 1 with a value of 8.6 ml. The average calibrated EDV RMSE has no bias component due merely to the calibration step. Further, the average calibrated EDV errors were uncorrelated with the corresponding reference echocardiographic EDV values (ρ = 0.06).

Figure (4.4) illustrates the results from all six dogs in terms of a plot of the average EF estimates versus the corresponding reference echocardiographic values. (Note that an

analogous plot of the calibrated EDV results may misleadingly reveal strong correlation simply due the calibration step.) Figures (4.5) and (4.6) illustrate the results from dogs 2 and 5 in terms of trends in the EF, calibrated EDV, and C_aE_{max} estimates (dark lines) as a function of time, along with the corresponding intermittent reference echocardiographic values (gray circles) and the employed interventions (underlines). These figures not only further reveal the correspondence between the model-based analysis technique and echocardiography but also demonstrate the advantage of the new technique in providing continuous hemodynamic monitoring. In addition, consistent with expectation, C_aE_{max} increased during dobutamine and decreased during esmolol.

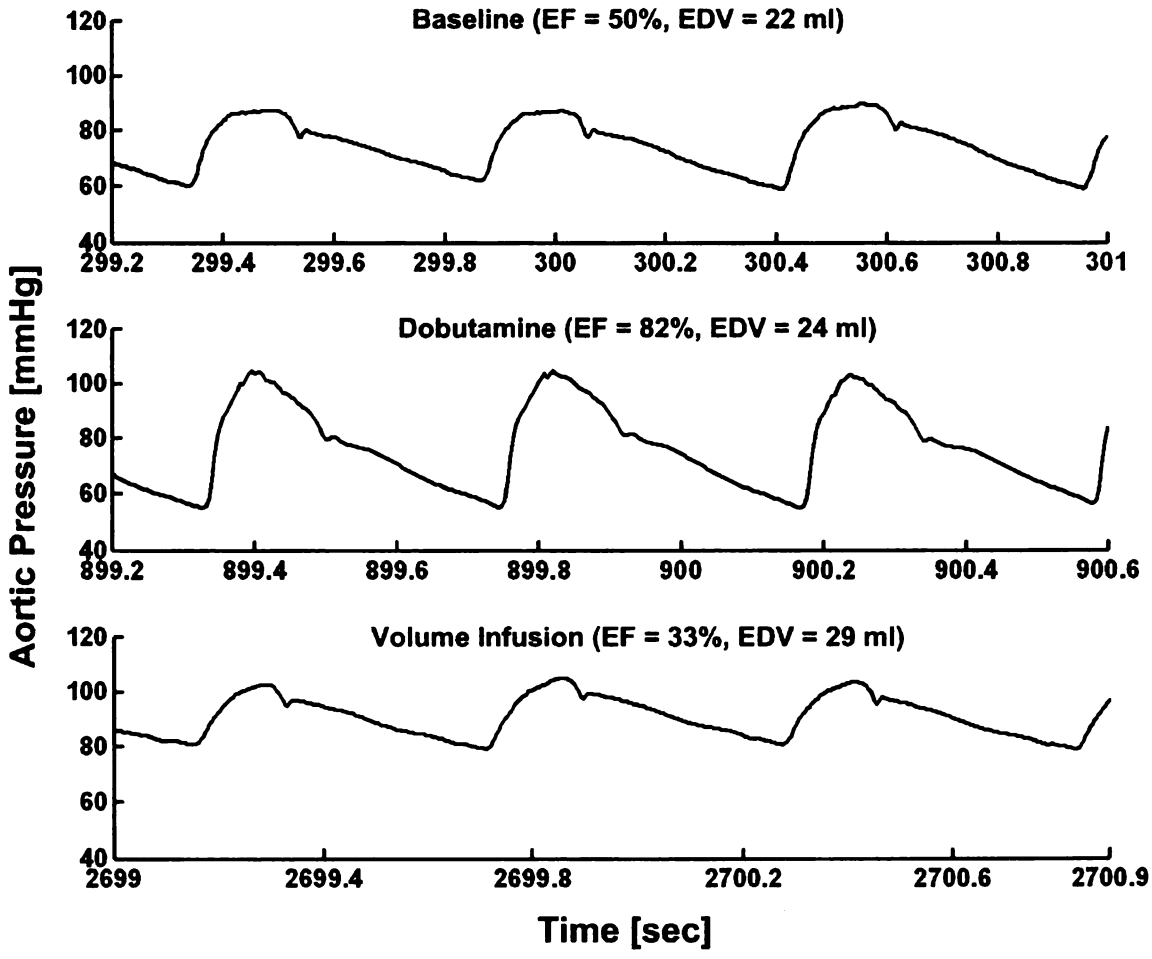

Figure 4.2 Exemplary segments of the aortic pressure waveform measured from the descending thoracic aorta in dog 2 during baseline, dobutamine, and volume infusion conditions.

Table 4.1 Summary of the hemodynamic range and results of the model-based analysis technique for each dog. EF is left ventricular ejection fraction; EDV, left ventricular end-diastolic volume; HR, heart rate; MAP, mean aortic pressure; and RMSE, root-mean-squared-error. The EF and EDV ranges were established with the reference echocardiographic measurements.

Dog	Number of Comparisons	EF Range [%]	EDV Range [ml]	MAP Range [mmHg]	EF RMSE [%]	EDV RMSE [ml]
1	7	53 - 90	28 - 46	67 - 156	8.5	8.6
2	9	33 - 84	17 - 29	60 - 94	6.1	1.9
3	10	56 - 74	21 - 25	58 - 118	4.1	4.5
4	10	52 - 69	18 - 23	42 - 82	3.4	4.3
5	17	37 - 74	10 - 15	36 - 116	5.5	1.4
6	9	43 - 74	13 - 18	53 - 128	5.8	3.3
Total	62	33 - 90	10 - 46	36 - 156	5.6	4.1

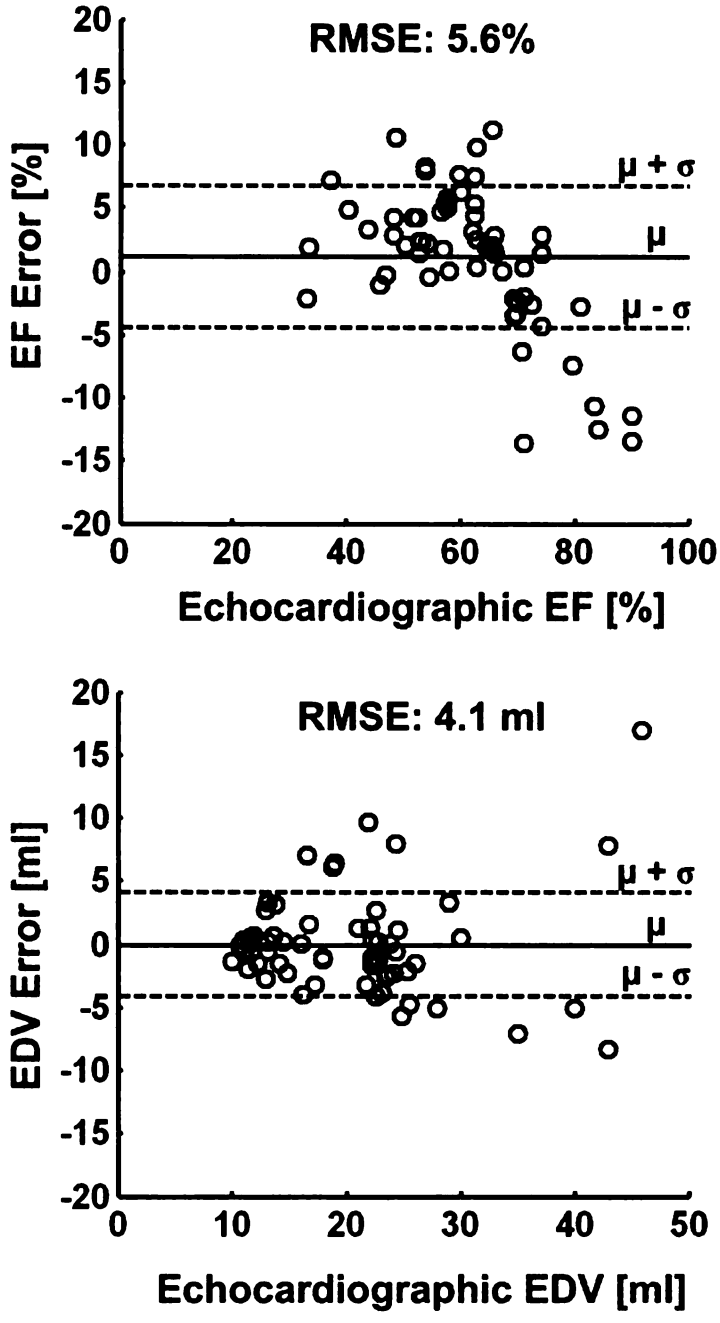

Figure 4.3 Results for all six dogs in terms of Bland-Altman plots of the average EF and average calibrated EDV errors as a function of the corresponding reference echocardiographic values. The parameter μ indicates the mean of the errors; σ, the standard deviation of the errors; and RMSE the root-mean-square of the errors (i.e., $\sqrt{\mu^2+\sigma^2}$).

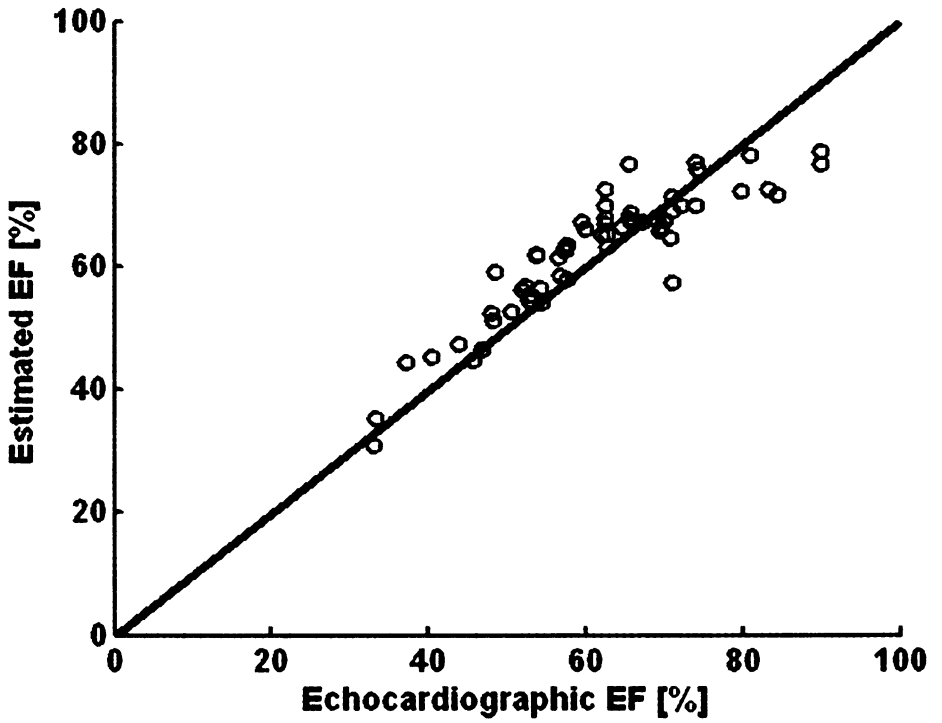

Figure 4.4 Results for all six dogs in terms of a plot of the average EF estimates versus the corresponding reference echocardiographic EF values.

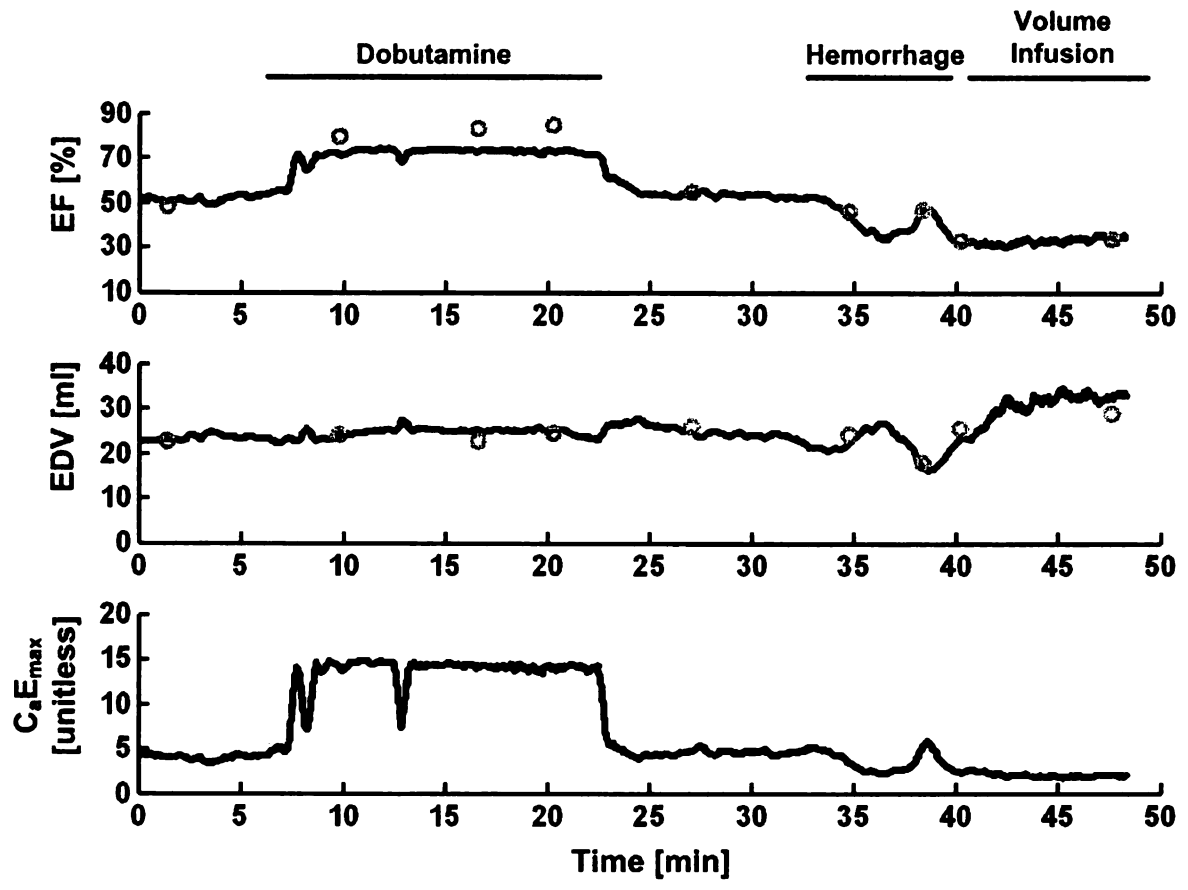

Figure 4.5 Results for dog 2 in terms of the trends in the EF, calibrated EDV, and C_aE_{max} estimates (dark lines) as a function of time, along with the corresponding intermittent reference echocardiographic values (gray circles) and the employed interventions (underlines).

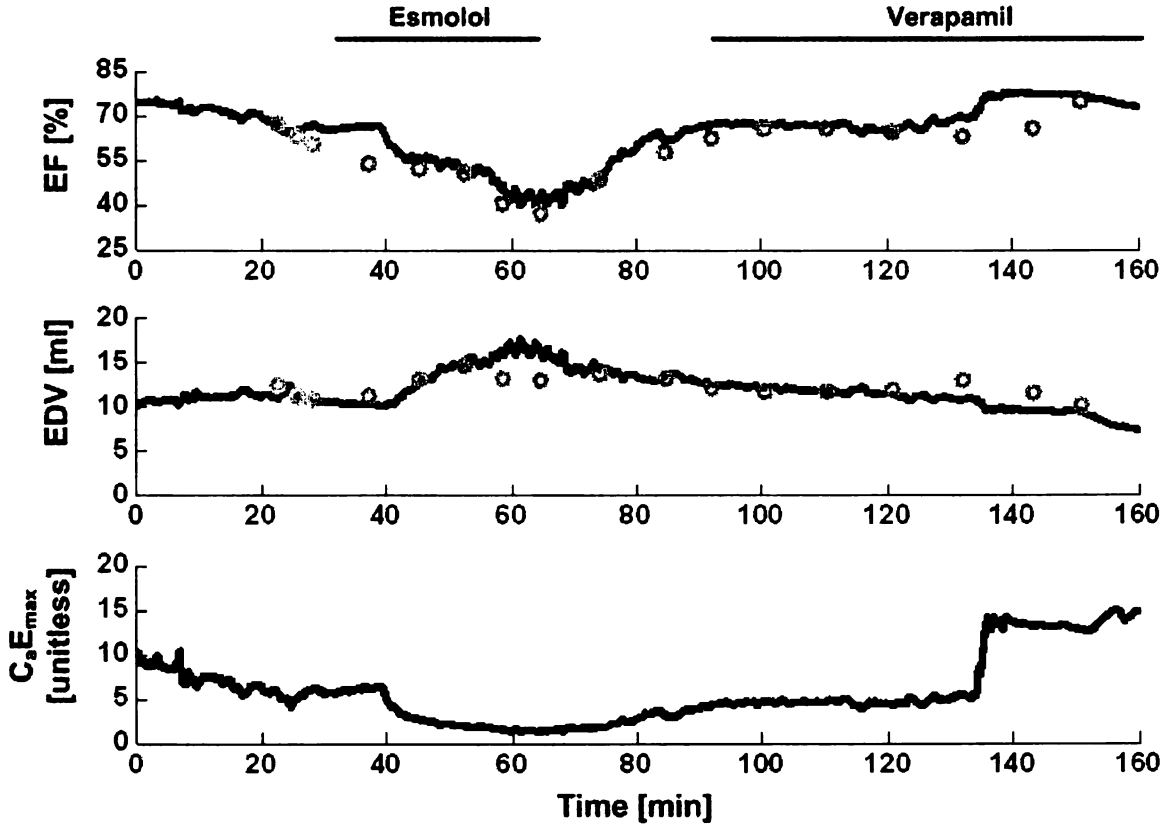

Figure 4.6 Results for dog 5 in terms of the trends in the EF, calibrated EDV, and C_aE_{max} estimates (dark lines) as a function of time, along with the corresponding intermittent reference echocardiographic values (gray circles) and the employed interventions (underlines).

Finally, the beat-to-beat calibrated CO RMSNE was 10.0% for dog 1. This RMSNE had no bias component again because of the calibration step.

4.5 Discussions

In summary, we have developed a novel technique to estimate EF by model-based analysis of the aortic pressure waveform (see Figure (4.1)). First, the aortic pressure waveform is represented with a lumped parameter model comprising a three-parameter variable elastance model of the left ventricle connected via a one-way, non-viscous valve to a Windkessel model of the arteries accounting for R_a and the nearly constant C_a. Then, this circulatory model is fitted to each beat of the waveform so as to estimate its lumped parameters to within a scale factor equal to C_a. Finally, these proportional parameter estimates along with a nominal value for V_{lv}^0 / C_a are utilized to compute beat-to-beat absolute EF by cancellation of the C_a scale factor. In this way, in contrast to conventional imaging methods, EF may be continuously monitored without making any assumptions about the left ventricular geometry. In addition, with the proportional parameter estimates, relative changes in EDV, SV, CO, R_a, and E_{max} may also be monitored on a beat-to-beat basis. Note that the traditional method for determining E_{max}, in particular, is much more cumbersome, requiring simultaneous measurements of left ventricular pressure and volume during alterations to the preload and/or afterload [Sagawa 1977, Suga 1974]. To evaluate the technique, we measured aortic pressure waveforms, intermittent average reference EF and EDV via standard echocardiography, and other cardiovascular variables from six dogs during various pharmacological and volume interventions (see Figure (4.2)). Our results showed overall RMSEs in average

EF and average calibrated EDV of 5.6% and 4.1 ml, respectively, as well as reliable estimation of relative changes in average E_{max} and beat-to-beat CO (see Table (4.1) and Figures (4.3)-(4.6)). This study is notable in that it may be the first to demonstrate the feasibility of estimating EF from only blood pressure.

Assumptions of the Model-Based Analysis Technique

Our model-based analysis technique is based on four major assumptions. We defend each of these assumptions below using known physiology and previous experimental findings.

Assumption 1: lumped parameter model representation of the aortic pressure waveform. It is well known that the arteries are not simply a lumped system but rather a complicated distributed system with impedance mismatches throughout due to vessel tapering, bifurcations, and caliber changes. As a result, peripheral artery pressure waveforms are heavily corrupted by wave reflections and generally require a distributed model for their representation. However, aortic pressure waveforms are less complicated by wave reflections due to destructive interference and attenuation of the reflected waves reaching the aorta [Noordergraaf 1978] as well as significant time delays between forward and backward waves in the aorta [Albaladejo 2001]. Thus, aortic pressure waveforms may be more amenable to a lumped parameter model representation. Indeed, consistent with the prediction of the lumped parameter model utilized herein (see Figure (4.1a)), Bourgeois et al. showed that aortic pressure waveforms measured specifically from the descending thoracic aorta exhibit pure exponential diastolic decays over a wide hemodynamic range [Bourgeois 1974]. We therefore placed the aortic catheter in the

descending thoracic aorta in this study, and the resulting aortic pressure waveforms generally confirmed their finding (see Figure (4.2)).

Assumption 2: constant arterial compliance. To estimate EF and relative changes in other hemodynamic variables including EDV and CO, the assumption is precisely that C_a is constant over a monitoring period (e.g., days to weeks) in a given subject. Note that this assumption is relaxed in terms of estimating just EF, as C_a must be invariant only within each cardiac cycle (see Equation (4.6)). Indeed, it is well known that C_a decreases gradually over the course of years in a subject (e.g., [Hallock 1937]). However, previous studies have indicated that C_a tends to decrease with increasing arterial pressure [Hallock 1937, Li 1994]. If this inverse relationship were strongly present in the dogs studied herein, EF would be significantly and consistently underestimated, while EDV would be grossly overestimated at high arterial pressures and underestimated at low arterial pressures. However, the EF error bias was small (see Figure (4.3)), and the EDV error was only mildly correlated with MAP ($\rho = 0.28$). Thus, C_a may have been sufficiently constant in our study even though MAP was varied over a wide range (see Table (4.1)), which is consistent with previous studies including those by Bourgeois et al. [Bourgeois 1974, Bourgeois 1976] (see below) and us [Lu 2006, R.Mukkamala 2006, Swamy 2008].

Assumption 3: three parameter raised cosine function representation of left ventricular elastance during the systolic ejection interval. In a surprising but compelling study, Senzaki et al. showed that experimentally measured $E_{lv}(t)$, normalized both in amplitude and time, were remarkably consistent in 87 patients despite extremely wide variations in their ventricular states (see discrete values in the lower panel of Figure

(4.1b)) [Senzaki 1996]. Heldt et al. then showed that these normalized data could be well fitted, especially during the systolic ejection interval (i.e., the higher elastance range), by a raised cosine function with three unknown parameters, E_{min}, E_{max}, and T_s (see Figure (4.1b) and Equation (4.5)) [Heldt 2002]. Further, E_{min} may be simply approximated as $0.05 \cdot E_{max}$ as suggested by the data of Senzaki et al (see Figure (4.3) in [Senzaki 1996]). Thus, $E_{lv}(t)$ during the systolic ejection interval may indeed be well represented using a raised cosine function with three unknown parameters, E_{max}, T_s, and $E_{lv}(n_{bs}T)$. Note that independent estimation of (proportional) E_{min} here would likely be unreliable anyhow, as it would essentially amount to an extrapolation. That is, E_{min} is not directly "seen" by aortic pressure, as the aortic valve is closed during diastole. Further note that attempts to represent $E_{lv}(t)$ with a Gaussian, trapezoidal, exponential or sinusoidal function (see [Guarini 1998]) and/or allow the ratio of the time period of the downstroke of $E_{lv}(t)$ to T_s to vary (rather than be fixed to 0.5 as assumed in Equation (4.5)) did not improve our EF estimation results. Finally, it should be emphasized that, while the assumption here constrains the shape of the left ventricular elastance function, its amplitude and width are allowed to vary in order to account for any changes that may occur in cardiac functioning.

Assumption 4: nominal value for proportional unstressed left ventricular volume. It is generally appreciated that V_{lv}^0 is usually much smaller than EDV. Thus, in many subjects including the healthy dogs studied herein, V_{lv}^0 / C_a may indeed be set to a nominal value or even neglected (i.e., no calibration) without substantially sacrificing the

EF estimation accuracy. In fact, varying V_{lv}^0 / C_a from 10 to 20 mmHg in this study only altered the EF RMSE by 2%. Alternatively, V_{lv}^0 / C_a may be determined by obtaining an independent measurement of EF via imaging and then finding the value of V_{lv}^0 / C_a that equalizes the EF estimated by aortic pressure waveform analysis to the independent EF measurement (i.e., single calibration). This alternative approach would be preferred in subjects with cardiac dilatation. Further, for these subjects, large changes in the EF estimated by aortic pressure waveform analysis with the determined V_{lv}^0 / C_a may, in turn, be utilized as a cue to re-image the heart (i.e., multiple calibrations). Finally, note that it is possible that the ratio of SV to stressed EDV (i.e., $V_{lv}^0 / C_a = 0$) could prove to be a valuable indicator of left ventricular function.

Potential Sources of Error

Any violation to the four above assumptions certainly represents a source of the errors reported herein. Another source of the errors is likely imperfect reference echocardiographic measurements due to, for example, individual variations in the trans-thoracic imaging window [Rumberger 1997], inaccuracies in endocardial contour definition [Hof 1998], and violation to the underlying ventricular geometry assumptions [Nosir 1996]. Indeed, we suspect that the relatively large EF errors at reference EF values > ~80% (see Fig. 3) were a result of the ventricular geometry assumptions of echocardiography breaking down at the very small ESVs. In addition, we surmise that the EF and EDV RMSEs were largest for dog 1 (see Table (4.1)), because the reference values were established by averaging over fewer beats than the other dogs (see above). On the other hand, we do not believe that measurement inaccuracies in the aortic pressure

waveforms were a major source of the errors, as high fidelity, micromanometer-tipped catheters were employed.

Computational Speed

Our implementation of the model-based analysis technique included a brute force search over a physiologic range to estimate the three parameters of the raised cosine left ventricular elastance function during the systolic ejection interval (see above). However, the technique may be implemented much more efficiently by exploiting the fact that the parameters usually do not change much from one beat to the next. For example, we estimated the parameters for one beat using the brute force search and then estimated the parameters for subsequent beats using a local simplex method with the parameter estimates of the previous beat specified as its initial seed. We actually implemented the brute force search for every tenth beat rather than for just the initial beat in order to attenuate any propagation of error due to, for example, ventricular ectopy. This implementation produced almost the same average EF estimates as the original brute force search and was ten times faster than real time when executed on MATLAB with a standard PC.

Previous Related Techniques

We find no techniques in the literature aiming to likewise monitor EF from only blood pressure waveforms. However, we are aware of two closely related, previous techniques.

Bourgeois et al. developed a technique to monitor relative changes in beat-to-beat SV by analysis of the aortic pressure waveform using a two-parameter Windkessel model of the arteries (see Figure (4.1a)) [Bourgeois 1976]. Their technique specifically involved

estimating SV to within a constant $1/C_a$ scale factor for each beat using the right-hand side of Eq. (3) with $t = t_{es}$ and τ determined by fitting an exponential to each diastolic interval of the waveform. These investigators applied their technique to canine aortic pressure waveforms measured from the descending thoracic aorta wherein pure exponential diastolic decays are visually apparent (see above). As a result, they were able to show excellent agreement between their technique and the gold standard aortic flow probe over a wide hemodynamic range. Our study builds upon the seminal work of Bourgeois et al. by modeling the left ventricle in addition to the arteries so as to also permit the monitoring of beat-to-beat absolute EF and proportional EDV and E_{max}.

Guarini, Urzua, and co-workers developed a technique to monitor beat-to-beat ventricular and arterial parameters based on analysis of the radial artery pressure waveform [Guarini 1998, Urzua 1998]. Their technique specifically involved representing the waveform with a parametric variable elastance model of the left ventricle in series with a third-order lumped parameter model of the arteries and then estimating the model parameters for each beat using a two-step procedure conceptually similar to one utilized herein. However, since these investigators desired the absolute values of the model parameters rather than EF, their technique also necessitated an operator-dependent thermodilution CO measurement. Thus, the technique is not automated and continuous. Moreover, unlike the aortic pressure waveform, the radial artery pressure waveform is heavily corrupted by wave reflections and is therefore generally unsuitable for representation with lumped parameter models, particularly those of low order (see above). Indeed, these investigators did not experimentally verify their technique against reference methods.

Potential Applications and Future Directions

Our model-based analysis technique may potentially be utilized in lieu of, or as a complement to, imaging methods so as to permit continuous monitoring of EF as well as other important proportional hemodynamic variables in subjects without aortic stenosis and instrumented with an aortic catheter. Examples of such subjects include animals in the context of research and patients undergoing cardiac catheterization or with intra-aortic balloon pumps. To eventually realize these applications, we plan to conduct further testing of the technique in both animals and humans, especially with severe systolic dysfunction.

In addition, we intend to adapt the technique to peripheral artery pressure waveforms, which, in contrast to aortic pressure waveforms, are routinely available in clinical practice via invasive catheters and can be measured non-invasively (see above). However, as we have discussed, analysis of peripheral artery pressure waveforms is technically more difficult due to significant distortion by wave reflections. To overcome this difficulty, we propose to first mathematically reconstruct the aortic pressure waveform from measured peripheral artery pressure waveforms using our multi-channel blind system identification technique [Swamy 2007, Swamy 2008] or possibly even the conventional generalized transfer function (e.g., [Chen 1997, Soderstrom 2002]) and then apply the model-based analysis technique to the reconstructed waveform.

Our hope is that these future directions ultimately lead to widespread automated and continuous EF monitoring by arterial pressure waveform analysis in various inpatients and outpatients as well as heart failure patients at home so as to help meet the increasing patient monitoring demands.

CHAPTER 5

QUANTIFICATION OF FORWARD AND BACKWARD ARTERIAL WAVES BY MODEL BASED ANALYSIS OF AORTIC AND FEMORAL ARTERY PRESSURE WAVEFORM

5.1 Introduction

It is well appreciated that arterial pressure and flow waveforms represent the sum and difference of forward and backward traveling waves in the arterial tree. The relative magnitude and timing of the backward or reflected wave likely play an important role in health and disease. For example, a wave reflected at the periphery that reaches the ascending aorta during systole would increase the cardiac afterload and thereby reduce the stroke volume. On the other hand, a reflected wave that arrives at the ascending aorta during diastole would enhance myocardial perfusion. It is therefore important to be able to quantify the wave reflections in order to obtain an improved understanding of circulatory pathophysiology and potentially develop more effective indices for monitoring cardiovascular health.

To this end, several techniques have been proposed to separate measured arterial waveforms into their forward and backward wave components. Westerhof et al. [Westerhof, 1972] modeled the arterial tree as a uniform frictionless tube in which the forward and backward pressure waves are equal to the product of the corresponding flow waves and the characteristic impedance of the tube. These investigators obtained simultaneous measurements of aortic pressure and flow waveforms in order to first determine the tube characteristic impedance from the high frequency regime of the

arterial input impedance (i.e., the ratio of the Fourier Transforms of the aortic pressure and flow waveforms) and then calculate the forward and backward waves from the measured waveforms and characteristic impedance by adding pressure waves and subtracting flow waves. Lee et al. [Lee, 1993] developed a more accurate technique to determine the tube characteristic impedance by measuring the arterial pressure and flow response to a single cardiac contraction using vagal stimulation. They were then able to likewise calculate the forward and backward waves. Burattini et al. [Burratini, 1989] employed a similar tube model but also represented its terminal load with a three-parameter Windkessel model. These researchers then estimated the model parameters by nonlinear least squares fitting between the aortic pressure waveform predicted from the model in response to a measured aortic flow waveform input and a simultaneously measured aortic pressure waveform. They were then able to calculate the forward and backward waves from the estimated model parameters.

As described above, the initial techniques all involved the measurement of an arterial flow waveform, which either requires surgery to place a flow probe around a blood vessel or an expert operator to stabilize an ultrasound transducer. Thus, the applicability of these techniques is limited. Recently, Westerhof et al. [Westerhof, 2006] proposed a technique to compute the forward and backward waves from aortic pressure alone by approximating the aortic flow waveform with a triangular pulse. However, this approximation could introduce significant error in the calculated waves for at least some pathophysiologic conditions.

In this study, we developed a technique to quantify forward and backward arterial waves by model-based analysis of only aortic and femoral artery pressure waveforms,

without making any assumptions about flow morphology. Furthermore, in contrast to most previous related efforts, we validated the forward and backward waves through a set of canine experiments by specifically showing that the waves accurately predicted a third arterial pressure waveform measurement and changed in the physiologically expected manner to interventions of known effect. Finally, we calculated the forward and backward waves during nine different hemodynamic conditions.

5.2 Technique

Our model-based analysis technique for quantifying forward and backward arterial waves is conceptually similar to that of Burattini et al. but with three major differences. Firstly, the model input and output are measured ascending aortic and femoral artery pressure waveforms instead of ascending aortic flow and pressure waveforms. Secondly, the tube load is effectively represented with a pole-zero model whose order is data-determined rather than being set to first-order a priori. Thirdly, the model parameters are determined using linear least squares estimation, which affords a convenient and reliable closed-form solution, in contrast to nonlinear least squares estimation, which requires a difficult and often imperfect numerical search.

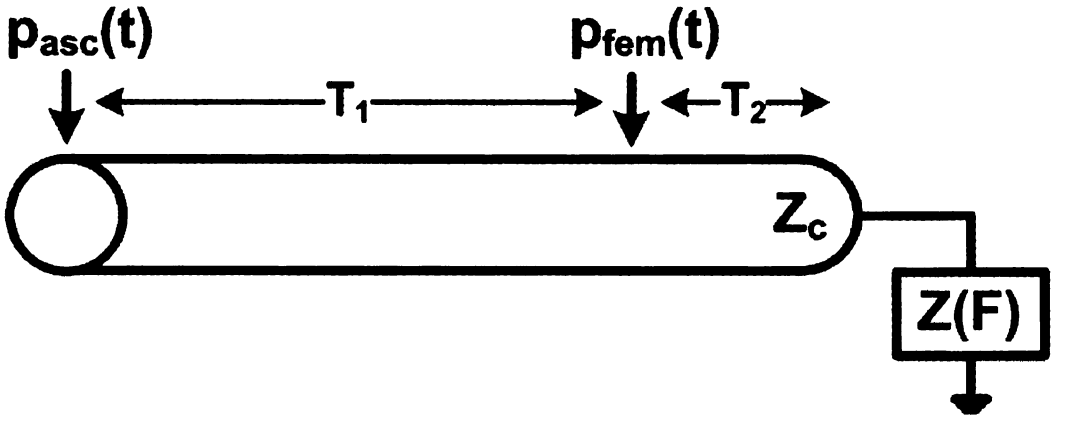

Figure 5.1 Arterial tube model upon which our technique is based.

More specifically, the technique is based on the arterial model of Figure (5.1) in which a distributed uniform tube is terminated by a lumped load. The tube represents the arterial conduit starting from the ascending aorta and passing through a femoral artery. Similar to previous studies, this tube is frictionless and therefore has constant characteristic impedance (Z_c). As a result, mean pressure is the same along the tube. The terminal load represents the arterial bed distal to the femoral artery. This load has a frequency-dependent impedance (Z(F), where F is frequency).

According to this model, the forward and backward waves at the terminal load ($p_f(t)$ and $p_b(t)$) are related as follows:

$$p_b(t) = \Gamma(t) \otimes p_f(t), \tag{5.1}$$

where $\otimes$ is the convolution operation, and $\Gamma(t)$ is the inverse Fourier Transform of $\Gamma(F) = \left(Z(F) - Z_c\right) / \left(Z(F) + Z_c\right)$, which is the frequency-dependent reflection coefficient at the terminal load. The ascending aortic and femoral artery pressure waveforms ($p_{asc}(t)$ and $p_{fem}(t)$) may then be expressed as the sum of appropriately shifted forward and backward waves as follows:

$$p_{asc}(t) = p_f(t + T_1 + T_2) + \Gamma(t) \otimes p_f(t - T_1 - T_2) \tag{5.2}$$

$$p_{fem}(t) = p_f(t + T_2) + \Gamma(t) \otimes p_f(t - T_2), \tag{5.3}$$

where T_1 is the measured time for the arterial wave to travel between the ascending aorta and the femoral artery, while T_2 is the unknown time for the arterial wave to travel between the femoral artery and the terminal load. Substitution of Equation (5.3) into Equation (5.2) gives the following equation:

$$\underbrace{p_{fem}(t+T_1)-p_{asc}(t)}_{y(t)} = \Gamma(t-2T_2)\otimes\underbrace{(p_{asc}(t)-p_{fem}(t-T_1))}_{x(t)}+e(t), \tag{5.4}$$

where the term e(t) has been included to account for measurement and/or modeling error.

The unknown $\Gamma(t)$ and T_2 are calculated in Equation (5.4) from the measured "input" x(t) and "output" y(t) by least squares minimization of e(t). This optimization problem is specifically solved using standard autoregressive exogenous input (ARX) identification and the MDL criterion 0. In this way, $\Gamma(t\text{-}2T_2)$ is efficiently represented with a pole-zero model whose unknown parameters are estimated with the linear least squares solution and whose unknown order and delay are determined from the measured waveforms. Then, the computed $\Gamma(t)$ and T_2 are substituted into Equations (5.2) and (5.3), and $p_f(t)$ is calculated from the measured $p_{asc}(t), p_{fem}(t)$ and T_1 by way of deconvolution. Rather than applying conventional deconvolution to Equations (5.2) and (5.3) to arrive at two versions of $p_f(t)$, a single, optimal $p_f(t)$ is specifically obtained from these equations using multi-channel linear least squares deconvolution as described in [Abed-Meriam, 1997].

Note that, with the calculated $p_f(t)$ and $p_b(t)$ along with T_2, the arterial pressure waveform at any point along the tube ($p_a(t,T)$) of the model of Figure (5.1) may be computed using the following equation:

$$p_a(t,T) = p_f(t+T+T_2)+p_b(t-T-T_2), \tag{5.5}$$

where T is the measured time for the arterial wave to travel between the point of interest and the femoral artery. Similarly, the arterial flow waveform at any point along the tube

($q_a(t,T)$) may be computed to within a proportionality constant equal to $1/Z_c$ through the following equation:

$$q_a(t,T) = \frac{1}{Z_c}(p_f(t+T+T_2) - p_b(t-T-T_2)). \quad (5.6)$$

However, because of branching between the ascending aorta and the femoral artery, the proportional $q_a(t,T)$ calculated at a given point in the tube does not have any correspondence to anatomy, except at the point of the femoral artery (i.e., T = 0). Here, the waveform specifically represents relative changes in femoral artery flow. Finally, note that, since $\Gamma(t)$ and T_2 are computed from zero-mean x(t) and y(t) in Equation (5.4), the mean value of proportional $q_a(t,T)$ may not be reliably determined. (However, the mean value of $p_a(t,T)$ should always be accurately determined, as it is effectively set to the mean value of the measured arterial pressure.)

5.3 Methods

A. Experimental Procedures

Experiments were performed in three normal adult beagles (10-12 kg). Each dog was studied under a protocol approved by the MSU All-University Committee on Animal Use and Care as follows. General anesthesia was induced with an intravenous injection of propofol (2.2-6.6 mg/kg) and maintained with inhaled isoflorane (1.5-2.5%). A micromanometer-tipped catheter (Millar Instruments, Houston, TX) was inserted into a either femoral or carotid artery and positioned via fluoroscopic guidance for measurement of the ascending aortic pressure waveform. A similar catheter was placed for measurement of the femoral artery pressure waveform. A catheter was introduced

into a cephalic vein for drug and isotonic fluid administration, and electrodes were placed for measurement of surface ECGs. In the third dog, a micromanometer-tipped catheter was also inserted into a femoral artery and placed for measurement of the abdominal aortic pressure waveform ($p_{abd}(t)$) as confirmed with fluoroscopy. In addition, a bipolar electrode catheter was advanced through the jugular vein of this dog into the right atrium via fluoroscopic guidance for atrial pacing using an external pulse generator (Medtronic, Minneapolis, MN). The analog transducer outputs were interfaced to a personal computer through an A/D conversion system (DataQ Instruments, Akron, OH). The cardiovascular measurements were then recorded at a sampling frequency of 1000 Hz during a baseline condition and following infusions of dobutamine and esmolol in the first dog; infusions of volume and hemorrhage in the second dog; and infusions of phenylephrine, nitroglycerin, and verapamil as well as atrial pacing in the third dog.

B. Data Analysis

The technique was applied to all 15-second segments of the ascending aortic and femoral artery pressure waveforms resampled to 250 Hz, with T_1 measured for each segment as the time delay between the onsets of upstroke of the two waveforms. Then, similar to the study of Burattini et al.[Burratini, 1989], the abdominal aortic pressure waveform was predicted ($p_a(t,T)$) for the 15-second segments from the calculated quantities, with T measured for each segment as the time delay between the onsets of upstroke of the measured abdominal aortic and femoral artery pressure waveforms. The predicted waveform was quantitatively evaluated with respect to the measured reference waveform through the root-mean-squared-error (RMSE). For comparison, the ascending aortic and femoral artery pressure waveforms were likewise evaluated with respect to the

measured abdominal aortic pressure waveform. In addition, the computed magnitude spectrum of the reflection coefficient ($|\Gamma(F)|$) and proportional femoral artery peak-to-peak flow were assessed during the phenylephrine and nitroglycerin conditions and baseline, dobutamine, esmolol, vasopressin and HIS-pacing conditions respectively. Finally, the computed forward and backward waves at the ascending aorta ($p_a(t+T_1+T_2)$ and $p_a(t-T_1-T_2)$) were examined during the baseline, phenylephrine and nitroglycerin conditions.

5.4 Results

The overall RMSE of the abdominal aortic pressure waveform predicted by the forward and backward waves, which were calculated from the ascending aortic and femoral artery pressure waveforms, was 2.4 mmHg. For comparison, the overall RMSE of the ascending aortic and femoral artery pressure waveforms with respect to the measured abdominal aortic pressure waveform was 5.9 and 4.5 mmHg, respectively. Figure (5.2) illustrates an example of the measured ascending aortic and femoral artery pressure waveform segments and the predicted abdominal aortic pressure waveform segment, along with the measured reference abdominal aortic pressure waveform segment.

Figure (5.3) illustrates the magnitude spectrum of the reflection coefficient calculated during the baseline, phenylephrine, and nitroglycerin conditions. Consistent with known physiology, this spectrum was amplified under the intense vasoconstrictor (phenylephrine) and blunted under the strong vasodilator (nitroglycerin). Figure (5.4) shows the reference (solid line) and predicted (dashed line) peak-peak femoral artery flow (solid line) for one of the dogs.

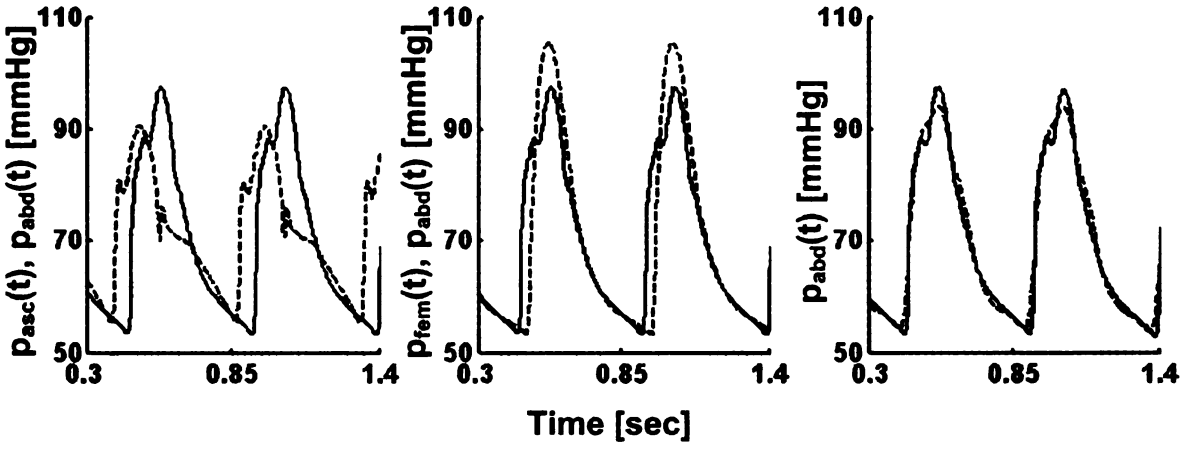

Figure 5.2 Example segments of the (a) measured ascending aortic pressure waveform, (b) measured femoral artery pressure waveform, and (c) predicted abdominal aortic pressure waveform (dash), along with the measured abdominal aortic pressure waveform (solid).

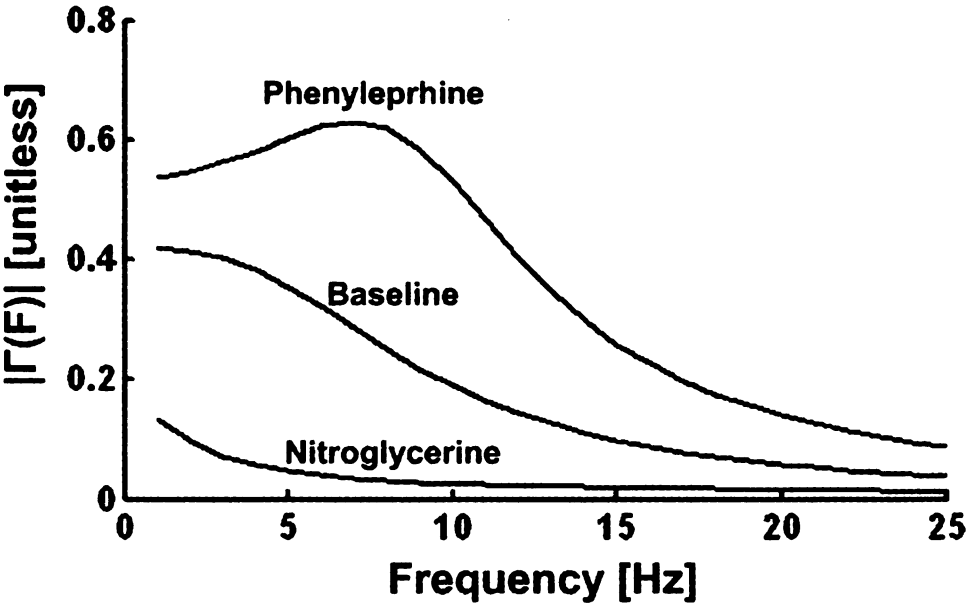

Figure 5.3 Computed magnitude spectrum of the reflection coefficient.

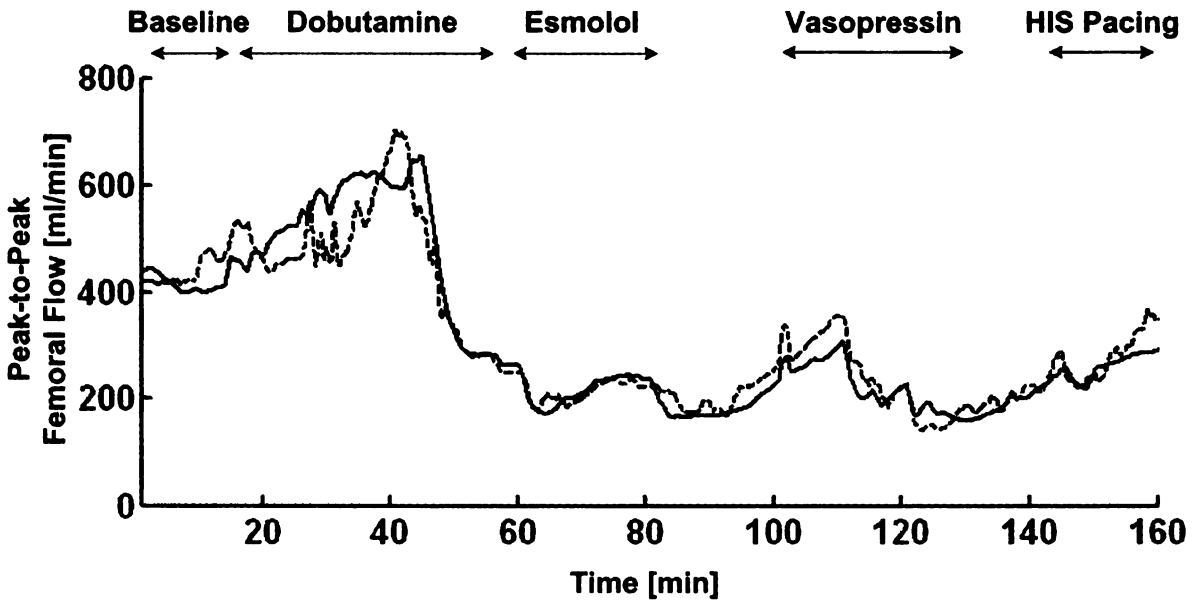

Figure 5.4 Predicted proportional femoral artery flow.

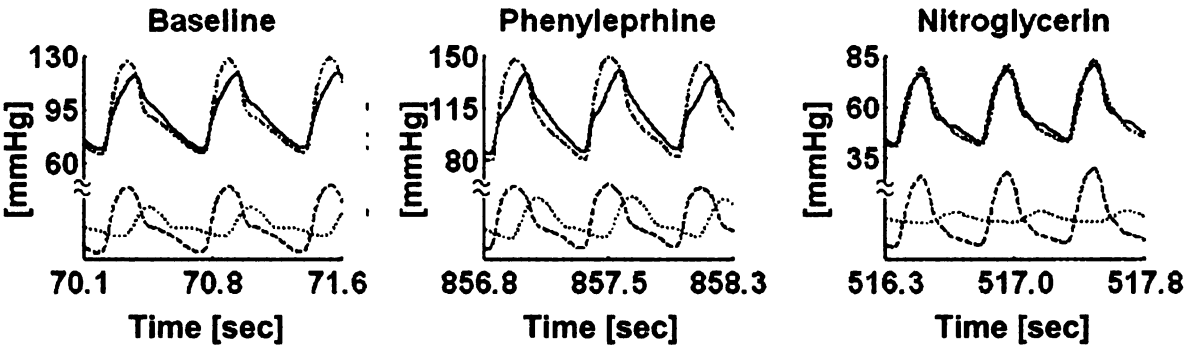

Figure 5.5 Measured ascending aortic and femoral artery pressure waveforms and calculated zero-mean forward and backward waves at the ascending aorta.

Figure (5.5) illustrates the measured ascending aortic and femoral artery pressure waveforms and the calculated zero-mean forward and backward waves at the ascending aorta during each of the nine experimental conditions. The magnitude of the backward wave relative to the forward wave appeared smallest during nitroglycerin and dobutamine and largest during phenylephrine and hemorrhage, while the time delay between the two waves was smallest during atrial pacing and about the same during the remaining eight conditions. Overall, the backward waves generally appeared like a time shifted and scaled version of the forward waves. This result is congruent with those of Lee et al. who, as described above, computed the waves using aortic pressure and flow measurements during vagal stimulation [Lee, 1993].

5.5 Discussions

In a companion study [Swamy, 2008], we modeled an arterial conduit with a tube model terminated by a first-order load and then utilized a numerical search to estimate the model parameters from only a femoral artery pressure waveform by exploiting the fact that aortic flow is zero during diastole. While the forward and backward arterial waves could be calculated from the estimated parameters, the main aim of that study was to estimate the aortic pressure waveform from a peripheral artery pressure waveform via an adaptive transfer function. In contrast, in this study, we aimed to accurately calculate the forward and backward waves by analysis of aortic and femoral artery pressure waveforms. By including both waveforms in the analysis, a higher order terminal load could be conveniently and accurately calculated in closed-form. We verified the forward and backward waves computed here by showing that these waves accurately predicted a third arterial pressure waveform measurement and changed in the physiologically

expected manner to interventions of known effect. We then examined the forward and backward waves during various hemodynamic conditions. In the future, we plan to continue the evaluation of the technique by quantitatively comparing the predicted proportional femoral artery flow with a corresponding independent reference measurement. With such future successful testing, the technique may ultimately be used to enhance the understanding of arterial wave phenomena in health and disease.

CHAPTER 6

ADAPTIVE TRANSFER FUNCTION FOR DERIVING THE AORTIC PRESSURE WAVEFORM FROM A PERIPHERAL ARTERY PRESSURE WAVEFORM

6.1 Introduction

Since its introduction by O'Rourke and co-workers in 1993 [Karamanoglu, 1993], the generalized transfer function has received attention for providing a convenient and safe means for monitoring central aortic pressure (AP) by mathematical transformation of a peripheral artery pressure (PAP) waveform. The basic premise of the transformation is that a single, universal transfer function exists that can faithfully relate the PAP waveform to the AP waveform of all individuals for all time. However, the transfer function linking PAP to AP would ideally be able to adapt to the inter-subject and temporal variability of the arterial tree due to, for example, age-related arterial compliance differences, baro- and thermo-regulatory modulation of peripheral resistance in response to physiologic perturbations, progression of peripheral vascular disease, and therapeutic administration of vasoactive agents. To this end, Sugimachi et al. [Sugimachi 2001] and Westerhof et al. [Westerhof 2007] have previously proposed a technique to partially adapt the transfer function by defining it through an arterial tube model with a personalized value for a model parameter reflecting the wave propagation delay time and population averages for the remaining parameters. We recently introduced perhaps the first entirely adaptive technique for mathematically deriving the AP waveform by

exploiting the commonality in multiple PAP waveforms through the powerful multi-channel blind system identification approach [Swamy 2007, Swamy 2008]. However, the requirement of more than one PAP waveform is a practical disadvantage of this technique.

In this study, we conceived a fully adaptive technique for deriving the AP waveform from only one PAP waveform. The new technique similarly defines the transfer function relating PAP to AP through a parallel tube model of pressure and flow in the arterial tree but then estimates all of its parameters by capitalizing on pre-knowledge of aortic flow with the model. The parameters are periodically re-estimated for each subject so as to derive an adaptive transfer function (ATF). We performed canine experiments in order to evaluate the ATF technique as well as compare it to previous transfer function techniques over a broad array of controlled and significant hemodynamic perturbations. A preliminary version of this study has been reported in abbreviated form [Swamy 2008].

6.2 Methods

Adaptive Transfer Function (ATF) Technique

Figure (6.1) illustrates the ATF technique. As shown in the top panel of this figure, the arterial tree is modeled as a parallel arrangement of m uniform tubes in series with terminal loads. The i^{th} tube represents the path between the aorta and the i^{th} peripheral artery. Each tube is frictionless and therefore has constant characteristic impedance ($Z_{ci} = \sqrt{(l_i / c_i)}$, where l_i and c_i are the tube's total inertance and compliance) and allows waves to propagate with constant velocity and delay time from one end of the tube to the other ($T_{di} = \sqrt{(l_i c_i)}$). Thus, consistent with Poiseulle's law, mean pressure is

identical throughout the tubes. The i^{th} terminal load signifies the arterial bed distal to the i^{th} peripheral artery. Like the studies of Sugimachi et al [Sugimachi 2001] and Westerhof et al. [Westerhof 2007], each terminal load has a frequency-dependent impedance ($Z_i(\omega)$, where ω is frequency) characterized by two parameters that are dependent on the peripheral resistance and compliance (A_i and B_i, where $0 < A_i < B_i$) as well as the characteristic impedance of the corresponding tube (i.e., Z_{ci}). Thus, the wave reflection coefficient at each terminal load is also frequency-dependent ($\Gamma_i(\omega) = \left(Z_i(\omega) - Z_{ci}\right) / \left(Z_i(\omega) + Z_{ci}\right)$).

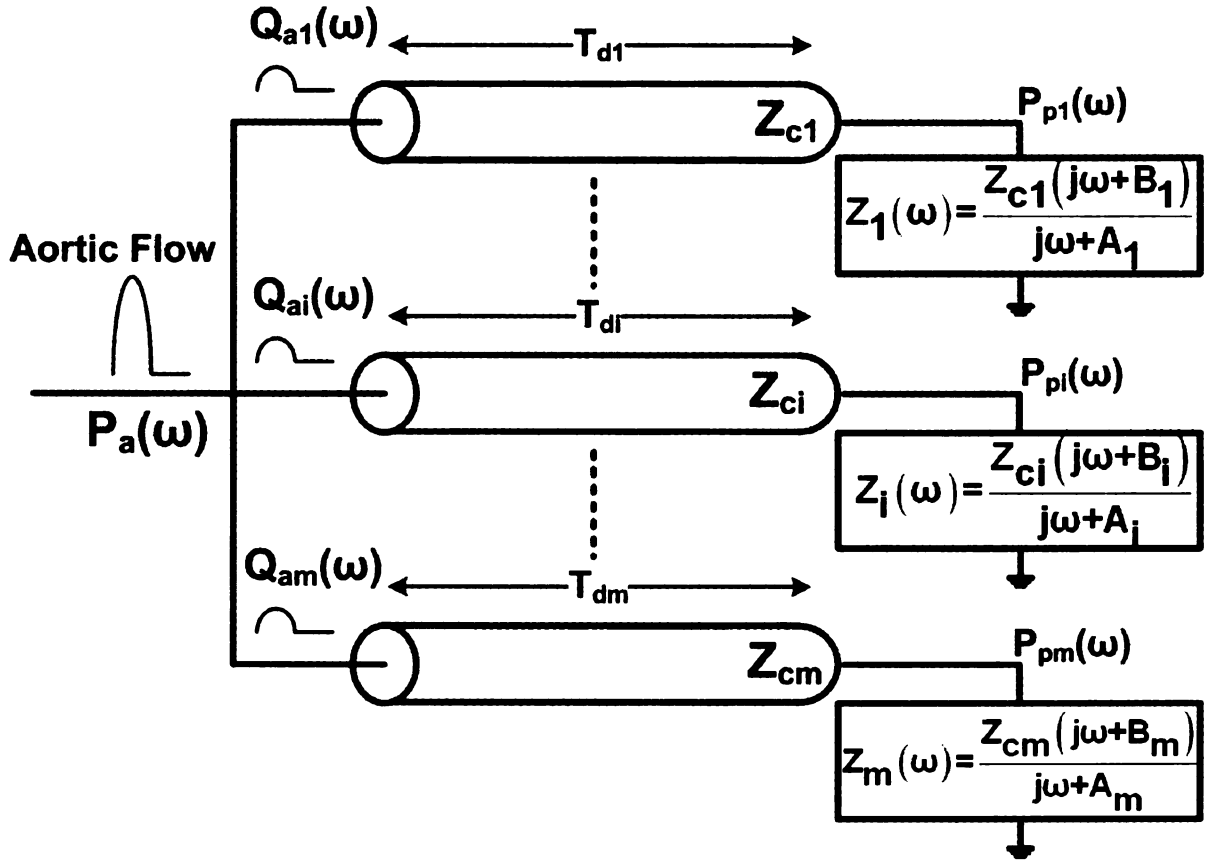

pressure → pressure transfer function

$$p_{pi}(t) \rightarrow \frac{\left(\frac{B_i+A_i}{2}+j\omega\right)e^{j\omega T_{di}}+\frac{B_i-A_i}{2}e^{-j\omega T_{di}}}{B_i+j\omega} \rightarrow p_a(t)$$

pressure → flow transfer function

$$p_{pi}(t) \rightarrow \frac{\left(\frac{B_i+A_i}{2}+j\omega\right)e^{j\omega T_{di}}+\frac{B_i-A_i}{2}e^{-j\omega T_{di}}}{B_i+j\omega} \rightarrow q_{ai}(t)$$

0 diastole

Figure 6.1 Adaptive transfer function (ATF) technique for deriving the aortic pressure (AP) waveform from a peripheral artery pressure (PAP) waveform.

Generally speaking, pressure and flow waves propagate along each tube without distortion and are proportional to each other through the tube characteristic impedance. Waves traveling in the forward direction (left to right) are reflected in the opposite or backward direction at the terminal load with relative magnitude and phase based on the frequency according to the wave reflection coefficient. The actual pressure (or flow) waveform at any point along a tube may therefore be expressed as the sum (or difference) of the forward and backward traveling pressure (or flow) waves appropriately shifted in time based on the distance between the point and the tube end. In this way, the model is able to mimic the well-known progressive distortion that experimental arterial pressure and flow waveforms undergo with increasing distance from the aorta. Further, from these expressions, a transfer function relating the arterial pressure or flow waveform at any point along a tube to the arterial pressure or flow waveform at any other point on the tube may be established in terms of the model parameters.

More specifically, according to the arterial tree model, a PAP waveform ($p_{pi}(t)$) is related to the AP waveform ($p_a(t)$) through the transfer function shown in the middle panel of Figure (6.1) ("pressure→pressure transfer function") with unknown model parameters (see detailed derivation in [Stergiopulos 1998]). Thus, this transfer function may be applied to a measured PAP waveform so as to derive the AP waveform, if its parameters, namely T_{di}, A_i and B_i, could be determined.

To this end, T_{di} the wave propagation delay time between the aorta and peripheral artery measurement site, is first measured non-invasively (see Discussion section). Only one T_{di} measurement is made for a subject during a monitoring period (e.g., on order of days), as arterial inertance and compliance may not greatly vary over this time period.

Thereafter, the three parameters are determined from each 15 sec segment of the measured PAP waveform and initial T_{di} value by exploiting the fact that aortic flow is negligible during each diastolic interval due to aortic valve closure (in absence of aortic regurgitation). Thus, as indicated in the top panel of Figure (6.1), the arterial flow at each tube entrance in the arterial tree model ("arterial entry flow") may likewise be small during these time intervals. In particular, according to this model, the PAP waveform is related to the arterial entry flow waveform to the corresponding peripheral artery ($q_{ai}(t)$) through the transfer function shown in the bottom panel of Figure (6.1) ("pressure→flow transfer function") with the same unknown model parameters as the pressure→pressure transfer function. The common parameters are then estimated by finding the pressure→flow transfer function, which when applied to the PAP waveform segment, minimizes the energy (sum-of-squares) of the arterial entry flow waveform (scaled by $q_{ai}(t)$) output over its diastolic intervals. In other words, as indicated in the bottom panel of Figure (6.1), the parameters are selected so as to map the PAP waveform to an arterial entry flow of zero during diastole. The detailed steps of the technique are given as follows.

First, since the mean or DC value of $p_a(t)$ is already known (i.e., approximated as the corresponding value of $p_{pi}(t)$due to Poiseuille's law), the DC value of $p_{pi}(t)$ is removed in order to focus the mapping on the unknown zero-mean or AC components. Then, AC $q_{ai}(t)$ is calculated to within a $1/Z_{ci}$ scale factor by applying the pressure→flow transfer function to AC $p_{pi}(t)$ for a set of A_i and B_i values over a physiologic range with the T_{di} value as measured. Next, the end of each diastolic

interval in each candidate AC proportional $q_{ai}(t)$ is determined by identifying the minimum preceding the peak amplitude of a cardiac cycle, and the start of each corresponding diastolic interval is approximated based on Malik's formula [Malik 1996] relating the cardiac cycle length to the systolic interval length. Then, the values of A_i and B_i are selected that provide the minimum variance of AC proportional $q_{ai}(t)$ over its diastolic intervals and yield physiologically reasonable pressure and flow waveforms (i.e., AC proportional $q_{ai}(t)$ exhibits an undershoot during diastole as typically seen in experimental waveforms [McDonald 1974] and $p_a(t)$, computed as described below, does not reveal double peaks). In the event that none of the A_i and B_i values in the set result in physiologically reasonable waveforms, T_{di} is successively incremented when mean pressure decreases relative to the T_{di} measurement period or decremented when mean pressure increases relative to this period (as T_{di} tends to have an inverse relationship with mean pressure for significant changes [Gribbin 1976]) until the criterion is satisfied. Finally, the pressure→pressure transfer function, with the selected values for A_i, B_i, and T_{di}, is applied to $p_{pi}(t)$ (including its DC value) so as to derive $p_a(t)$. (Note that the DC value of proportional $q_{ai}(t)$ may be determined by shifting the diastolic intervals of the AC waveform to zero amplitude.)

Data Collection

Data were collected from six healthy adult beagles (10-12 kg) under an experimental protocol approved by the MSU All-University Committee on Animal Use and Care. For each dog, general anesthesia was induced by an intravenous injection of propofol (2.2-6.6 mg/kg) and maintained with an inhaled mixture of oxygen and isoflorane (1.5-2.5%). A

micromanometer-tipped catheter (Millar Instruments, Houston, TX) was placed in a femoral artery for the PAP waveform for analysis. A similar catheter was inserted in the opposite femoral artery or a carotid artery and positioned in the ascending aorta for the reference AP waveform. A catheter was also placed in a cephalic vein for drug and isotonic fluid administration, and electrodes were positioned for standard ECG measurements. In the fifth dog, a bipolar electrode catheter (EP Technologies, Boston Scientific, Sunnyvale, CA) was inserted into a jugular vein and advanced to the right atrium for high rate pacing with an external pulse generator (Medtronic, Minneapolis, MN). In the sixth dog, a quadrapolar ablation catheter (EP Technologies) was inserted into a femoral vein and positioned to ablate the AV node and then apply bipolar electrical stimulation to the His bundle as previously described [Sanders 2004] for low rate pacing with the external pulse generator. (Additional instrumentation was also installed in the fifth and sixth dogs to address different specific aims.) Placement of all central catheters was accomplished using single-plane lateral projection fluoroscopic guidance. The analog transducer outputs were interfaced to a personal computer (DataQ Instruments, Akron, OH). The arterial pressure waveforms and ECG measurements were recorded at a sampling rate of 1000 Hz during a baseline period and following infusions of phenylephrine and nitroglycerin in the first dog; dobutamine and esmolol in the second dog; norepinephrine and xylazine in the third dog; saline and progressive hemorrhage in the fourth dog; verapamil and high rate pacing in the fifth dog; and vasopressin (prior to AV node ablation) and low rate pacing in the sixth dog. Several infusion and pacing rates were employed followed by recovery periods.

Data Analysis

The ATF technique was applied off-line to approximately 300 min of recorded PAP waveforms re-sampled to 250 Hz, with T_{di} measured for each dog as the time interval between the onsets of upstroke of the AP and PAP waveforms during the initial beats of the baseline period. The resulting derived AP waveforms were lowpass filtered with a cutoff frequency of 15 Hz as previously justified [Fetics 1999] and then quantitatively evaluated against the (unfiltered) reference AP waveforms in terms of the sample-to-sample (total waveform, TW), beat-to-beat systolic pressure (SP), and beat-to-beat pulse pressure (PP) root-mean-squared-error (RMSE) values. The unprocessed PAP waveforms were likewise assessed with respect to the reference AP waveforms after time-aligning the two waveforms to eliminate error due merely to the wave propagation delay. For further comparison, AP waveforms were also derived by an autoregressive exogenous input-based generalized transfer function (GTF_{ARX}) technique [Fetics 1999] (which was shown to be the most accurate amongst three generalized transfer function techniques) and the tube model-based partially adaptive transfer function ($PATF_{TUBE}$) technique [Sugimachi 2001, Westerhof 2007] (i.e., the transfer function shown in the top panel of Figure (6.1) with T_{di} measured for each dog as described above and the same values for the A_i and B_i parameters for all dogs). More specifically, the two previous transfer functions were established by averaging over set of transfer functions computed from each 15 sec segment of the PAP and AP waveforms of one dog and then applied to the PAP waveforms of the remaining dogs (see Discussion section). The resulting derived AP waveforms were then similarly lowpass filtered and evaluated. This procedure was repeated for each dog in order to avoid any bias, and the results were averaged.

6.3 Results

Table (6.1) illustrates the AP and heart rate (HR) levels during each of the experimental conditions. Table (6.2) shows the TW, SP, and PP RMSE values of the PAP waveforms after time-alignment and the AP waveforms derived by the new ATF technique as well as the previous GTF_{ARX} and $PATF_{TUBE}$ techniques for each condition and overall. Figure (6.2) provides visual examples of the measured AP and PAP waveform segments and the corresponding derived AP waveform segments during the dobutamine and nitroglycerin conditions.

The AP and HR levels (mean±SD) varied widely over the different experimental conditions. Mean arterial pressure (MAP) ranged from 62±3 to 134±15 mmHg, SP, from 78±8 to 162±22 mmHg, PP, from 18±1 to 55±11 mmHg, and HR, from 73±20 to 197±16 bpm.

In general, the PAP waveforms were significantly different from the reference AP waveforms, especially in terms of SP and PP. The overall TW, SP, and PP RMSE values of the time-aligned waveforms were 8.6, 16.9, and 19.9 mmHg, respectively. The level of discrepancy between the unprocessed PAP and reference AP waveforms likewise varied over the different experimental conditions. The RMSE values were by far the smallest during the nitroglycerin condition (average of 2.7 mmHg) and largest during the norepinephrine condition (average of 26.4 mmHg).

Table (6.1) illustrates the AP and heart rate (HR) levels during each of the experimental conditions. Table (6.2) shows the TW, SP, and PP RMSE values of the PAP waveforms after time-alignment and the AP waveforms derived by the new ATF technique as well as the previous GTF_{ARX} and $PATF_{TUBE}$ techniques for each condition

and overall. Figure (6.2) provides visual examples of the measured AP and PAP waveform segments and the corresponding derived AP waveform segments during the dobutamine and nitroglycerin conditions.

Table 6.1 Aortic pressures (AP) and heart rate (HR) levels. Values are expressed as mean±SD. MAP is mean arterial pressure; SP, systolic pressure; and PP, pulse pressure.

Condition	MAP [mmHg]	SP [mmHg]	PP [mmHg]	HR [bpm]
Baseline	88±20	104±24	34±9	127±7
Phenylephrine	132±14	158±19	49±9	98±9
Nitroglycerin	62±3	79±3	27±1	96±1
Dobutamine	89±2	116±3	51±2	172±8
Esmolol	71±3	85±3	24±0	113±1
Norepinephrine	134±15	162±22	55±11	117±13
Xylazine	65±8	78±8	25±1	100±10
Saline	98±1	119±1	45±1	137±1
Hemorrhage	66±5	80±5	25±1	105±4
Verapamil	74±10	90±11	33±3	115±10
High Rate Pacing	75±3	85±2	18±1	197±16
Vasopressin	94±15	108±16	28±3	103±4
Low Rate Pacing	73±7	95±5	42±6	73±20

Table 6.2 Peripheral artery pressure (PAP) and derived AP waveform errors. ATF is adaptive transfer function; GTF_{ARX}, autoregressive exogenous input-based generalized transfer function; $PATF_{TUBE}$, tube model-based partially adaptive transfer function; TW, total waveform (i.e., sample-to-sample); and RMSE, root-mean-squared-error.

	Time Aligned PAP			ATF			GTF_{ARX}			$PATF_{TUBE}$		
Condition	**TW**	**SP**	**PP**	**TW**	**SP**	**PP**	**TW**	**SP**	**PP**	**TW**	**SP**	**PP**
	RMSE [mmHg]			**RMSE [mmHg]**			**RMSE [mmHg]**			**RMSE [mmHg]**		
Baseline	10.3	20.0	21.8	6.3	10.2	8.8	5.1	5.9	4.9	5.4	8.5	7.1
Phenylephrine	10.6	19.8	22.6	3.3	4.8	4.4	5.4	6.5	6.1	7.9	4.7	4.2
Nitroglycerin	3.1	1.9	2.0	3.8	6.9	6.6	5.3	9.4	8.2	4.4	8.0	7.8
Dobutamine	7.7	12.5	16.7	5.2	3.0	3.0	8.2	12.8	15.9	6.6	5.3	7.7
Esmolol	5.0	11.0	11.3	2.0	0.7	1.4	2.8	2.2	3.2	2.4	3.6	2.3
Norepinephrine	14.0	30.6	34.7	5.4	8.0	7.9	7.3	6.2	6.0	9.1	11.0	10.7
Xylazine	6.1	12.9	13.5	2.5	4.0	3.3	3.2	2.7	2.0	2.9	4.7	4.1
Saline	11.5	20.9	24.7	3.7	3.5	3.6	4.8	4.7	5.7	4.6	6.5	7.0
Hemorrhage	6.5	15.5	15.9	2.4	2.6	1.2	2.7	3.6	3.0	3.0	6.2	5.2
Verapamil	7.9	15.0	16.4	3.7	6.5	6.5	2.6	2.5	3.2	3.3	4.7	4.6
High Rate Pacing	7.6	13.3	21.2	4.0	2.7	4.3	2.6	2.6	4.7	3.8	6.0	6.5
Vasopressin	6.9	13.7	16.6	3.7	3.4	5.5	3.6	3.0	2.4	2.7	4.0	4.6
Low Rate Pacing	6.9	15.4	16.7	4.0	2.7	4.9	3.0	2.3	2.1	2.5	3.8	3.8
Overall	**8.6**	**16.9**	**19.9**	**4.1**	**5.3**	**5.3**	**4.8**	**6.2**	**6.9**	**5.1**	**6.5**	**6.5**

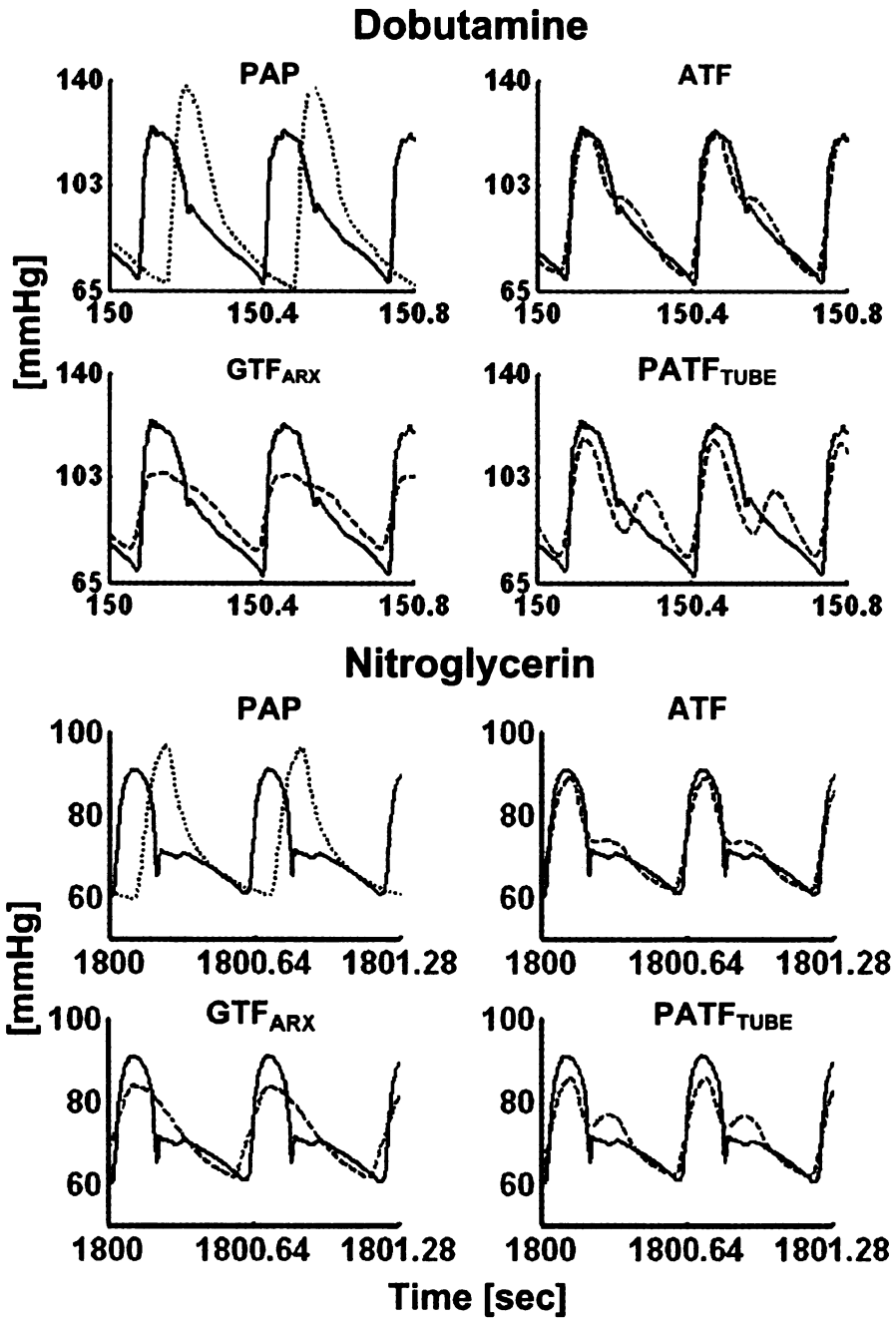

Figure 6.2 Example segments of the reference AP (solid), measured PAP (dot), and derived AP (dash) waveforms by the new ATF technique and previous autoregressive exogenous input-based generalized transfer function (GTF_{ARX}) and tube model-based partially adaptive transfer function ($PATF_{TUBE}$) techniques during the dobutamine and nitroglycerin conditions.

The AP and HR levels (mean±SD) varied widely over the different experimental conditions. Mean arterial pressure (MAP) ranged from 62±3 to 134±15 mmHg, SP, from 78±8 to 162±22 mmHg, PP, from 18±1 to 55±11 mmHg, and HR, from 73±20 to 197±16 bpm.

In general, the PAP waveforms were significantly different from the reference AP waveforms, especially in terms of SP and PP. The overall TW, SP, and PP RMSE values of the time-aligned waveforms were 8.6, 16.9, and 19.9 mmHg, respectively. The level of discrepancy between the unprocessed PAP and reference AP waveforms likewise varied over the different experimental conditions. The RMSE values were by far the smallest during the nitroglycerin condition (average of 2.7 mmHg) and largest during the norepinephrine condition (average of 26.4 mmHg).

All three techniques were able to derive the AP waveform with considerably greater accuracy than merely time aligning the PAP waveform over all the experimental conditions. Each of the techniques also afforded improved accuracy over the unprocessed PAP waveforms for each condition, except for nitroglycerin in which the measured PAP and AP waveforms were already in close agreement and dobutamine for the GTF_{ARX} technique only. The ATF technique was the most accurate over all the conditions. The overall TW, SP, and PP RMSE values of the AP waveforms derived by the new technique were 4.1, 5.3, and 5.3 mmHg, respectively. The corresponding RMSE values for the GTF_{ARX} and $PATF_{TUBE}$ techniques were similar to each other and, on average, 5.0, 6.4, and 6.7 mmHg. The ATF technique achieved its most significant improvements in accuracy over the two previous techniques during the conditions of dobutamine (average reduction in TW, SP, and PP RMSE values by 5.7 mmHg), saline

(2.0 mmHg), hemorrhage (1.9 mmHg), phenylephrine (1.6 mmHg), nitroglycerin (1.4 mmHg), esmolol (1.4 mmHg), and norepinephrine (1.3 mmHg). However, the GTF_{ARX} and $PATF_{TUBE}$ techniques did derive the AP waveform with similarly greater accuracy than the new technique during the conditions of baseline (average reduction in TW, SP, and PP RMSE values by 2.3 mmHg) and verapamil (2.1 mmHg).

6.4 Discussion

Pressure waveforms simultaneously measured from the central aorta and a peripheral artery show striking differences in both morphology and level (see, e.g., Figure (6.2)). Most importantly from a clinical point of view, peripherally measured SP and PP are generally larger than their centrally measured counterparts. This counter-intuitive amplification of the pressure waveform with increasing distance from the central aorta arises from wave reflections in the arterial tree. It is therefore the pressure in the central aorta that truly indicates cardiac afterload and myocardial perfusion. Perhaps, as a consequence, previous studies have shown that centrally measured arterial pressure can offer superior clinical information to more distally measured pressure [Safar 2009, Wadell 2001]. Even so, the PAP waveform is much more commonly measured in practice due to the relative ease and safety of its measurement.

In this study, we developed a technique to mathematically transform a PAP waveform so as to obtain the AP waveform conveniently and safely. The technique was inspired by the following investigators: 1) Stergiopulos et al. [Stergiopulos 1998] who proposed a physical basis for the transfer function relating PAP to AP through an arterial tube model; 2) Sugimachi et al. [Sugimachi, 2001] and Westerhof et al. [Westerhof 2007] who employed the tube model to establish a partially adaptive transfer function for deriving

the AP waveform, and 3) Cohen who thought to compute the total aortic flow waveform from a PAP waveform by finding a black-box, rather than physical model-based, transfer function that maps the PAP waveform to zero during diastole (personal communication in 2000 and now described in [Cohen 2008] as a result of this study). Our technique similarly defines the transfer function relating PAP to AP through a tube model and then estimates the unknown model parameters from the PAP waveform as well as a one-time non-invasive measurement of the wave propagation delay time between the aorta and peripheral artery measurement site by likewise exploiting the fact that aortic flow is negligible during diastole (see Figure (6.1)). In this way, in contrast to the conventional generalized transfer function and perhaps all other previous techniques for mathematically deriving the AP waveform, the new technique is able to fully adapt to the inter-subject and temporal variability of the arterial tree with only a single PAP waveform available for analysis.

To demonstrate the feasibility of the new ATF technique, we measured a PAP waveform from a femoral artery and the reference AP waveform from the ascending aorta of six healthy beagles of similar size during twelve different hemodynamic interventions (see Table (6.1)). Thus, unlike most previous related efforts, we were able to assess the efficacy of the technique over a diverse set of significant perturbations of known effect. On the other hand, our measurements did not allow us to investigate the technique in the context of a diverse population of subjects.

Our results (see Table (6.2) and Figure (6.2)) showed that the average of the overall TW, SP, and PP RMSE values of the AP waveforms derived by the ATF technique was 4.9 mmHg. This error effectively amounted to a 68% reduction in wave distortion in the

PAP waveforms. The corresponding RMSE values for the GTF_{ARX} and $PATF_{TUBE}$ techniques were each about 22% higher than the new technique, despite the fact that both of these previous techniques had the unfair advantage of being developed with or "seeing" the entire reference AP waveform from one of the six homogenous dogs (i.e., a baseline condition and two of the interventions). Note that, even under the most favorable scenario for the GTF_{ARX} and $PATF_{TUBE}$ techniques in which the reference AP waveforms from all six dogs were utilized for both development and testing, the RMSE values for these techniques still remained larger than the ATF technique by about 7% on average (results not shown). While the previous techniques would indeed be developed in practice with data from many more subjects (e.g., hundreds), they would be applied to an even greater number of subjects (e.g., all patients). In other words, the previous techniques would be developed with data from a much smaller fraction of the subject population in practice than the one-sixth proportion employed herein. We therefore believe that the new technique will show even greater than 22% improvement in accuracy over the previous techniques in actual practice.

Not surprisingly, the ATF technique was able to derive the AP waveform with appreciably better accuracy than the GTF_{ARX} and $PATF_{TUBE}$ techniques specifically during the conditions wherein the arterial tree was directly perturbed. The one exception was the vasopressin condition, which resulted in a relatively small hemodynamic change (see Table (6.1)). However, the new technique actually offered by far its greatest improvement in accuracy over the two previous techniques during the dobutamine condition. Evidently, intense vasodilation occurred during this positive cardiac inotropic condition, as centrally measured PP and HR markedly increased relative to the baseline

condition without a change in MAP (see Table (6.1)). For the remaining conditions in which the heart was primarily influenced, the three techniques showed similar overall accuracy, with the ATF technique affording notably greater accuracy during the esmolol condition but particularly less accuracy during the verapamil condition. The new technique was also equally less accurate than the previous techniques during the baseline condition. It is unclear why the ATF technique was not as effective during these two conditions.

The parallel tube model upon which the ATF technique is based (see top panel of Figure (6.1)) neglects arterial tapering and stiffening, as the dominant wave reflection sites appear to be at the arterial terminations due to their high resistance [McDonald 1974, Westerhof 1972]. The model also ignores the inertance of the distal arterial bed, since it is well appreciated that inertial work is small compared to viscous work in the high-pressure systemic arterial tree. Nevertheless, such modeling inaccuracies as well as imperfect parameter estimation represent the sources of error of the technique. To determine the relative contributions of the modeling and parameter estimation errors to the derived AP waveform error, we first found the "actual" parameter values using the measured PAP and AP waveforms. We specifically established the actual parameter values for each individual segment of analysis by finding the pressure→pressure transfer function (see middle panel of Figure (6.1)), which when applied to the PAP waveform segment, best fits the measured AP waveform segment in the least squares sense. We then applied the transfer function with the actual parameter values to the PAP waveform segment so as to derive the AP waveform segment. The TW RMSE value of the derived AP waveforms therefore represents the lower bound for the ATF technique due only to its

modeling error. Table (6.3) shows the resulting TW RMSE values, along with the SP and PP RMSE values (which do not represent lower bounds), for each condition and overall. The overall TW RMSE value was 3.0 mmHg, which indicates that most (73%) of the corresponding value for the ATF technique is due to modeling error. Finally, as a related comment, note that the GTF_{ARX} and $PATF_{TUBE}$ techniques derived the AP waveform with similar average overall RMSE values (see Table (6.2)) perhaps as a result of the modeling error offsetting the partial individualization of the latter tube model-based technique.

For this demonstration study, we obtained the single measurement of the wave propagation delay time between the aorta and the peripheral artery measurement site (T_{di}) for each dog using a few beats of the measured AP and PAP waveforms during the baseline period. In practice, T_{di} may be measured non-invasively by, for example, placing a handheld tonometer on the carotid artery and determining the time between the onsets of upstroke of the waveform that it measures and the recorded PAP waveform [Sugimachi 2001]. For continuous monitoring applications, such an operator-required measurement would likely need to be made periodically (e.g., every few days). Alternatively, $T_{di\,i}$ may be continuously approximated through, for example, a simultaneously recorded ECG or phonocardiogram.

It is claimed that the generalized transfer function is justified when applied to a PAP waveform from the upper limb but not the lower limb [O'Rourke 2008]. Despite this claim, we measured the PAP waveform from a femoral artery in this study due to experimental convenience, the observation that this waveform appears significantly different from the AP waveform (see Figure (6.2) and Table (6.2)), and the fact that this

peripheral artery is commonly cannulated in clinical practice. Our study may therefore be amongst, if not, the first to demonstrate the feasibility of mathematically transforming a PAP waveform from a lower limb to the AP waveform. In principle, due to its ability to adapt to arterial tree changes, our technique should be applicable to pressure waveforms obtained from any peripheral artery including the readily accessible radial artery (but excluding distal arteries in the coronary circulation for which arterial entry flow is significant during diastole). However, while we believe that our technique will also reveal improved accuracy over the generalized transfer function when applied to a PAP waveform from the upper limb, we do acknowledge the possibility that the overall difference in accuracy may not be as significant.

Table 6.3 Derived AP waveform errors using actual tube model parameter values. TW RMSE values represent lower bound for the ATF technique.

Condition	TW	SP	PP
	RMSE [mmHg]		
Baseline	4.1	5.8	3.8
Phenylephrine	2.9	3.0	2.2
Nitroglycerin	2.9	3.6	3.0
Dobutamine	4.8	2.6	3.5
Esmolol	1.6	2.1	0.9
Norepinephrine	3.7	2.6	2.2
Xylazine	1.9	2.9	1.4
Volume	3.5	1.5	1.3
Hemorrhage	2.1	3.6	1.7
Verapamil	2.7	2.2	1.3
High Rate Pacing	3.1	3.9	5.3
Vasopressin	1.5	1.4	1.5
Low Rate Pacing	1.8	1.2	2.1
Total	**3.0**	**3.2**	**2.9**

In summary, we have developed perhaps the first fully adaptive technique for mathematically deriving the AP waveform from one PAP waveform and have demonstrated its feasibility in animals over a wide range of physiologic conditions. In the future, it would be worthwhile to explore refinements to the parallel tube model upon which the technique is based (e.g., the inclusion of additional parameters to more accurately represent the terminal loads) as well as continuous approximation of the wave propagation delay time from simultaneously recorded non-invasive measurements. In addition, validation of the technique as applied to invasive and non-invasive PAP waveforms from the upper and lower limbs of humans is a must. If such follow-up studies prove successful, then the technique could be employed for more precise arterial pressure monitoring and titration of therapy in inpatient settings wherein PAP catheters are inserted and other clinical environments such as outpatient clinics and home in conjunction with non-invasive PAP devices. Finally, subsequent combination of the technique with an AP waveform analysis technique that we have also recently developed [Swamy 2009] may ultimately permit continuous monitoring of cardiac output and left ventricular ejection fraction in addition to AP from just a single PAP waveform.

CHAPTER 7

CONCLUSIONS

In this dissertation we have presented several techniques to estimate clinically relevant hemodynamic parameters from routinely measured blood pressure waveforms.

In chapter 2 we introduced a technique to estimate the clinically more relevant central aortic pressure waveform from multiple, less invasively measured peripheral artery pressure waveforms distorted by wave reflections. The technique is based on multi-channel blind system identification in which two or more measured outputs (peripheral artery pressure waveforms) of a single input, multi-output system (arterial tree) are mathematically analyzed so as to reconstruct the common unobserved input (central aortic pressure waveform) to within an arbitrary scale factor. Consequently, in contrast to previous, related efforts, the technique does not utilize a generalized transfer function or any training data and is therefore entirely patient and time specific. We have evaluated the technique with respect to four swine in which peripheral artery pressure waveforms from the femoral and radial arteries and a reference central aortic pressure waveform were simultaneously measured during diverse hemodynamic interventions. We report that the technique was able to reliably estimate the entire central aortic pressure waveform with an overall root-mean-squared-error of 4.7 mmHg. This error effectively represented a reduction in the total wave distortion in the measured peripheral artery pressure waveforms by 45%. As a result, the technique was also able to provide

similar improvements in the estimation of systolic pressure, pulse pressure, and the ejection interval.

In chapter 3 we proposed a refinement to the MBSI technique wherein the transfer function characterizing the path between the aorta and the peripheral arteries is represented using damped sinusoidal functions. This representation effectively lowered the number of estimation parameters and therefore helped in reducing the reconstruction error. This improvement facilitated fitting of the reconstructed waveform to lumped element Windkessel models for continuous estimation of beat-to-beat cardiac output. With further successful testing, the new technique may ultimately be employed for automated and less invasive monitoring of central hemodynamics in places where multiple catheter systems are employed.

In the next chapter we outlined a technique to estimate left ventricular ejection fraction (EF) by model-based analysis of the aortic pressure waveform. In this way, in contrast to conventional imaging, EF may be continuously monitored without making any assumptions about the left ventricular geometry. Moreover, with the proportional parameter estimates, relative changes in left ventricular end-diastolic volume (EDV), cardiac output (CO), total peripheral resistance, and maximum left ventricular elastance (E_{max}) may also be monitored on a beat-to-beat basis. To evaluate the technique, we measured aortic pressure waveforms, intermittent reference EF and EDV via standard echocardiography, and other cardiovascular variables from six anesthetized dogs during various pharmacological and volume interventions. Our results showed overall EF and calibrated EDV root-mean-squared-errors of 5.6% and 4.1 ml, respectively, as well as reliable estimation of relative changes in E_{max} and beat-to-beat CO. These results

demonstrate, perhaps for the first time, the feasibility of estimating EF from only blood pressure. With further successful testing, the technique may potentially be employed for continuous EF monitoring in subjects instrumented with an aortic catheter such as animals in research and patients undergoing cardiac catheterization. Future work involves extending the technique to estimate EF and other left ventricular parameters from measurements of peripheral artery pressure waveforms.

In subsequent chapters we utilized a transmission line representation of the arterial path between the aorta and the peripheral arteries to derive the wave reflection characteristic of the reflection path. This model was then extended to estimate aortic pressure waveform from a single peripheral artery pressure waveform based on the knowledge that aortic input flow is zero during diastole. To demonstrate the feasibility of this adaptive transfer function technique, we performed experiments in six healthy dogs in which peripheral artery and aortic pressure waveforms were simultaneously recorded during twelve different hemodynamic interventions. Our results showed that the aortic pressure waveforms derived by the technique were in superior agreement to the reference aortic pressure waveforms (average overall error of 4.9 mmHg) than the unprocessed peripheral artery pressure waveforms (average overall error of 15.1 mmHg) and the aortic pressure waveforms derived by two previously proposed transfer functions developed on a subset of the same canine data (average overall error of 6.0 mmHg).

Future work involves validating these techniques on data from human subjects and exploring more sophisticated models for arterial tree representations. With such further successful testing the techniques may ultimately be employed in the clinical

settings for continuous monitoring of cardiovascular status and also in home and ambulatory environments with the use of non-invasive measurement devices.

REFERENCES

Abed-Meraim K, Qiu Q and Hua Y. Blind system identification. *Proc of IEEE* 85: 1310-1332, 1997.

Albaladejo P, Copie X, Boutouyrie P, Brigitte L, Déclère AD, Smulyan H, Bénétos A. Heart rate, arterial stiffness, and wave reflections in paced patients. *Hypertension* 38: 949-952, 2001.

Ansari M, Barry M. Heart failure: how big is the problem? Who are the patients? What does the future hold? *Am Heart J* 146: 1-4, 2003.

Asada HH, Shaltis P, Reisner A, Rhee S and Hutchinson RC. Mobile monitoring with wearable photoplethysmographic biosensors. *IEEE Eng Med Biol Magazine* 22: 28-40, 2003.

Barcroft H, Edholm OG, McMichael J, and Sharpey-Schafer EP. Posthaemorrhagic fainting: study by cardiac output and forearm flow. *Lancet*, 1:489–491, 1944.

Berger DS, Li JK, Laskey WK, and Noordergraaf A. Repeated reflection of waves in the systemic arterial system. *Am. J. Physiol. Heart. Circ. Physiol* 264: 269-281, 1993.

Berger RD, Saul JP, and Cohen RJ. Transfer function analysis of autonomic regulation I. Canine atrial rate response. *Am J Physiol Heart Circ Physiol* 256: 142-152, 1989.

Bland JM, Altman DG. Statistical methods for assessing agreement between two methods of clinical measurement. *Lancet* 1(8476): 307-310, 1986.

Bosch X, Theroux P. Left ventricular ejection fraction to predict early mortality in patients with non-ST-segment elevation acute coronary syndromes. *Am Heart J* 150: 215-220, 2005.

Bourgeois M J, Gilbert B K, Donald.D.E, and Wood.E.H. Characteristics of aortic diastolic pressure decay with application to the continuous monitoring of changes in peripheral vascular resistance. *Circ Res* 35: 56-66, 1974.

Bourgeois MJ, Gilbert BK, Bernuth G and Wood EH. Continuous determination of beat-to-beat stroke volume from aortic pressure pulses in the dog. *Circ Res* 39: 15-24, 1976.

Burattini R, and Campbell KB. Modified asymmetric t-tube model to infer arterial wave reflection at the aortic root. *IEEE Trans Biomed Eng* 36: 805-814, 1989.

Burkhoff D. The conductance method of left ventricular volume estimation methodologic limitations put into perspective. *Circulation* 81(2): 703-706, 1990.

Chen CH, Nevo E, Fetics B, Pak PH, Yin FC, Maughan WL, and Kass DA. Estimation of central aortic pressure waveform by mathematical transformation of radial tonometry pressure. Validation of generalized transfer function. *Circulation* 95: 1827-1836, 1997.

Cintron G, Johnson G, Francis G, Cobb F, Cohn JN. Prognostic significance of serial changes in left ventricular ejection fraction in patients with congestive heart failure. *Circulation* 87(6): 17-23, 1993.

Cohen RJ. Flow estimation. *M.I.T. Case No. 13176*, 2008.

Critchley LAH, and Critchley JAJH. A meta-analysis of studies using bias and precision statistics to compare cardiac output measurement techniques. *J Clin Monit Comput* 15: 85-91, 1999.

Critchley LAH, Critchley JAJH. A meta-analysis of studies using bias and precision statistics to compare cardiac output measurement techniques. *J Clin Monit Comput* 15: 85-91, 1999.

Curtis JP, Sokol SI, Wang Y, Rathore SS, Ko DT, Jadbabaie F, Portnay EL, Marshalko SJ, Radford MJ, Krumholz HM. The association of left ventricular ejection fraction, mortality, and cause of death in stable outpatients with heart failure. *J Am Coll Cardiol* 42(4): 736-742, 2003.

Dellegrottaglie S, Filardi PP, Pace L, Ponticelli MP, Corrado L, Cafiero M, Polimeno M, Camerino R, Chiariello M. Non imaging nuclear monitoring of left ventricular function: twenty-five years of technical development and clinical experience. *Ital Heart J* 3(5): 300-307, 2002.

Donald AM. *Blood Flow in Arteries*. London: Edward Arnold, 1960.

Fetics B, Nevo C, Chen H, and Kass DA. Parametric model derivation of transfer function for noninvasive estimation of aortic pressure by radial tonometry. *IEEE Trans Biomed Eng* 46:698-706, 1999.

Gribbin B, Steptoe A, Slight P. Pulse wave velocity as a measure of blood pressure change. *Psychophysiology* 13:86-90, 1976.

Guarini M, Urzua J, Cipriano A, Gonzalez W. Estimation of cardiac function from computer analysis of the arterial pressure waveform. *IEEE Trans Biomed Eng* 45(12): 1420-1428, 1998.

Guyton AC, and Hall JE. *Textbook of Medical Physiology.* Philadelphia, PA: W.B. Saunders Company, 1996.

Hallock P, Benson JC. Studies on the elastic properties of human isolated aorta. *Am J*

Physiol 16: 595-602, 1937.

Hansen PC. *Rank Deficient and Discrete Ill-Posed Problems: Numerical Aspects of Linear Inversion.* Philadelphia, PA: SIAM, 1987.

Heldt T, Shim EB, Kamm RD, Mark RG. Computational modeling of cardiovascular response to orthostatic stress. *J Appl Physiol* 92(3): 1239-1254, 2002.

Igarashi Y, Goto Y, Osamu Y, Ishii T, Suga H. Transient vs. steady end-systolic pressure-volume relation in dog left ventricle. *Am J Physiol Heart Circ Physiol* 252: 998-1004, 1987.

Imholz BPM, Wieling W, Montfrans GA and Wesseling KH. Fifteen years experience with finger arterial pressure monitoring: assessment of technology. *Cardiovasc Res* 38: 605-616, 1998.

Jain AK. Fast inversion of banded toeplitz matrices by circular decompositions. *IEEE Trans Acoustics, Speech and Signal Processing* 26: 121-126, 1978.

Karamanoglu M and Feneley MP. On-line synthesis of the human ascending aortic pressure pulse from the finger pulse. *Hypertension* 30: 1416-1424, 1997.

Karamanoglu M, and Feneley MP. Derivation of the ascending aortic-carotid pressure transfer function with an arterial model. *Am J Physiol* 271: 2399-2404, 1996.

Karamanoglu M, O'Rourke MF, Avolio AP and Kelly RP. An analysis of the relationship between central aortic and peripheral upper limb pressure waves in man. *Eur Heart J* 14: 16-167, 1993.

Katz AM. *Physiology of the Heart.* New York: Raven Press, 1992.

Kenner T. ABP and its measurement. *Basic Res Cardiol* 83: 107-121, 1988.

Lee CC, and Mark RG. Analysis of arterial waves by the single-pulse-response method. *IEEE Trans Biomed Eng* 40, 833-836, 1993.

Li JK, Zhu Y. Arterial compliance and its pressure dependence in hypertension and vasodilation. *Angiology* 45: 113-117, 1994.

Ljung L. *System Identification: Theory for the User.* Englewood Cliffs, NJ: Prentice Hall, 1999.

Lu Z, Mukkamala R. Continuous cardiac output monitoring in humans by invasive and non-invasive peripheral blood pressure waveform analysis. *J Appl Physiol* 101(2): 598-608, 2006.

Malik M. If Dr. Bazett had a computer. *PACE* 19:1635-1639, 1996.

Marino PL. *The ICU Book.* Baltimore, MD: Lippincott Williams & Wilkins, 1998.

Martinez JP, Almeida R, Olmos S, Rocha AP, Laguna P. A wavelet-based ECG delineator: evaluation on standard databases. *IEEE Trans Biomed Eng* 51(4): 570-581, 2004.

McCombie DB, Reisner AT and Asada HH. Laguerre-model blind system identification: cardiovascular dynamics estimated from multiple peripheral circulatory signals. *IEEE Trans Biomed Eng* 52: 1889-1901, 2005.

McDonald DA. *Blood flow in the arteries.* London: Edward Arnold, 1974.

Mukkamala R, Reisner AT, Hojman HM, Mark RG, and Cohen RJ. Continuous cardiac output monitoring by peripheral blood pressure waveform analysis. *IEEE Trans Biomed Eng* 53: 459-467, 2006.

Noordergraaf A. *Circulatory System Dynamics.* New York: Academic Press, 1978.

Nosir YF, Fioretti PM, Vletter WB, Boersma E, Salustri A, Postma JT, Reijs AE, Ten Cate FJ, Roelandt JR. Accurate measurement of left ventricular ejection fraction by three-dimensional echocardiography. A comparison with radionuclide angiography. *Circulation* 94(3): 460-466, 1996.

O' Rourke MF, Avolio AP. Arterial transfer functions: background, applications and reservations. *J Hypertens* 26:8-10, 2008.

O'Rourke MF and Yaginuma T. Wave reflections and the arterial pulse. *Arch Intern Med* 144: 366-371, 1984.

Rumberger JA, Behrenbeck T, Bell MR, Breen JF, Johnston DL, Holmes DR, Enriquez-Sarano M. Determination of ventricular ejection fraction: a comparison of available imaging methods. *Mayo Clin Proc* 72: 860-870, 1997.

Rushmer RF, Franklin DL, Ellis RM. Left ventricular dimensions recorded by sonocardiometry. *Circ Res* 4: 684-688, 1956.

Saeed M, Lieu C, Raber G, and Mark RG. MIMIC II: a massive temporal icu patient database to support research in intelligent patient monitoring. *CINC*, 29:641-644, 2002.

Safar ME, Blacher J, Pannier B, Guerin AP, Marchais SJ, Guyonvarc'h P and London GM. Central Pulse pressure and mortality in end-stage renal disease. *Hypertension* 38: 735-738, 2002.

Sagawa K, Suga H, Shoukas AA, Bakalar KM. End-systolic pressure/volume ratio: a

new index of ventricular contractility. *Am J Cardiol* 40: 748-753, 1977.

Sanders R, Bailie M, Olivier NB. Stability of ventricular depolarization in conscious dogs with chronic atrioventricular dissociation and his-bundle pacing. *Pacing Clin Electrophysiol* 27:1475-1483, 2004.

Schiller NB. Two-dimensional echocardiographic determination of left ventricular volume, systolic function, and mass. Summary and discussion of the 1989 recommendations of the American Society of Echocardiography. *Circulation* 84(3): 280-287, 1991.

Segers P, Carlier S, Pasquet A, Rabben SI, Hellevik LR, Remme E, Backer TD, Sutter JD, Thomas JD and Verdonck P. Individualizing the aorto-radial pressure transfer function: feasibility of a model-based approach. *Am J Physiol* 279: H542-H549, 2000.

Senzaki H, Chen CH, Kass DA. Single-beat estimation of end-systolic pressure-volume relation in humans. A new method with the potential for non-invasive applications. *Circulation* 94: 2497:2506, 1996.

Soderstrom S, Nyberg G, O'Rourke MF, Sellgren J and Ponten J. Can a clinically useful aortic pressure wave be derived from a radial pressure wave? *Br J Aneasth* 88: 481-488, 2002.

Sridhara B, Bhattacharya, Liu XJ, Broadhurst P, Lahiri A. Rate of change of left ventricular ejection fraction during exercise is superior to the peak ejection fraction for predicting functionally significant coronary artery disease. *Brit Heart J* 70: 507-512, 1993.

Stergiopulos N, Westerhof BE, Westerhof N. Physical basis of pressure transfer from periphery to aorta: a model-based study. *Am J Physiol* 43:1386-1392, 1998.

Suga H, Sagawa K. Instantaneous pressure-volume relationships and their ratio in the excised, supported canine left ventricle. *Circ Res* 35: 117-126, 1974.

Sugimachi M, Shishido T, Miyatake K and Sunagawa K. A new model-based method of reconstructing central aortic pressure from peripheral arterial pressure. *Jpn J Physiol* 51: 217-222, 2001.

Swamy G, Kuiper J, Gudur M, Olivier NB, Mukkamala R. Continuous left ventricular ejection fraction monitoring by aortic pressure waveform analysis. *Annals of Biomed Eng,* To Appear.

Swamy G, Ling Q, Li T and Mukkamala R. Blind identification of the central aortic pressure waveform from multiple peripheral arterial pressure waveforms. *28th IEEE EMBS Conf*: New York City, NY, 2006.

Swamy G, Ling Q, Li T, Mukkamala R. Blind identification of the aortic pressure waveform from multiple peripheral artery pressure waveforms. *Am J Physiol* 292:2257-2264, 2007.

Swamy G, Mukkamala R, Olivier NB. Estimation of the aortic pressure waveform from a peripheral artery pressure waveform via an adaptive transfer function. *30th Annual IEEE EMBS Conf* 1:1385-1388, 2008.

Swamy G, Mukkamala R. Estimation of the aortic pressure waveform and beat-to-beat cardiac output from multiple peripheral artery pressure waveforms. *IEEE Trans Biomed Eng* 55:1521-1529, 2008.

Swamy G, Olivier NB, and Mukkamala R. Estimation of the aortic pressure waveform from a peripheral artery pressure waveform via an adaptive transfer function. *Am J Physiol,* Submitted.

U.S. Department of Health and Human Services, Health Resources and Services Administration, Bureau of Health Professions. Projected Supply, Demand, and Shortage of Registered Nurses: 2000-2002, July, 2002.

Urzua J, Salinas C, Cipriano A, Guarini M, Lema G, Canessa R. Estimation of ventricular volume and elastance from the arterial pressure waveform. *J Clin Monit Comput* 14(3): 177-181, 1998.

van't Hof AW, Schipper CW, Gerritsen JG, Reiffers S, Hoorntje JC. Comparison of radionuclide angiography with three echocardiographic parameters of left ventricular function in patients after myocardial infarction. *Int J Card Imaging* 14(6): 413-418, 1998.

Wadell TK, Dart AM, Medley TL, Cameron JD, Kingwell BA. Carotid pressure is a better predictor of coronary artery disease severity than brachial pressure. *Hypertension* 38:927-931, 2001.

Westerhof BE, Guelen I, Stok WJ, Wesseling KH, Spaan JA, Westerhof N, Bos WJ, Stergiopulos N. Arterial pressure transfer characteristics: effects of travel time. *Am J Physiol* 292:800-807, 2007.

Westerhof BE, Guelen I, Westerhof N, Karemaker JM, and Avolio A. Quantification of wave reflection in the human aorta from pressure alone. A proof of principle. *Hypertension* 48: 595-601, 2006.

Westerhof N, Sipkema P, Van Den Bos GC, and Elzinga G. Forward and backward waves in the arterial system. *Cardiovasc. Res* 6: 648-656, 1972.

Xu G, Liu H, Tong L and Kailath T. A least-squares approach to blind channel identification. *IEEE Trans Signal Processing* 43: 2982-2993, 1995.

Zhang Y, Asada HH and Reisner AT. Noninvasive cardiac output monitoring based on multi-channel blind system identification and modal decomposition. *Proc 2nd Joint EMBS/BMES Conf* 1: 218-219, 2002.

Zhenwei L, and Mukkamala R. Continuous cardiac output monitoring in humans by invasive and noninvasive peripheral blood pressure waveform analysis. *J Appl Physiol* 101: 598-608, 2006.